1-1-2014

# INTERFACIAL DYNAMICS OF DROP COALESCENCE AND IMPINGING LIQUID JETS: EFFECT OF VISCOUS, MARANGONI AND SHEAR-THINNING STRESSES

Jiakai Lu
*Purdue University*

# PURDUE UNIVERSITY
## GRADUATE SCHOOL
## Thesis/Dissertation Acceptance

This is to certify that the thesis/dissertation prepared

By Jiakai Lu

Entitled

INTERFACIAL DYNAMICS OF DROP COALESCENCE AND IMPINGING LIQUID JETS: EFFECT OF VISCOUS, MARANGONI AND SHEAR-THINNING STRESSES

For the degree of Doctor of Philosophy

Is approved by the final examining committee:

Dr. Carlos M. Corvalan Dr. Paul E. Sojka

Dr. Paul E. Sojka

Dr. Osvaldo Campanella

Dr. Stephen Heister

To the best of my knowledge and as understood by the student in the Thesis/Dissertation Agreement, Publication Delay, and Certification/Disclaimer (Graduate School Form 32), this thesis/dissertation adheres to the provisions of Purdue University's "Policy on Integrity in Research" and the use of copyrighted material.

Dr. Carlos M. Corvalan Dr. Paul E. Sojka

Approved by Major Professor(s): _____

_____

Approved by: Dr. Ganesh Subbarayan 12/04/2014

Head of the Graduate Program Date

# INTERFACIAL DYNAMICS OF DROP COALESCENCE AND IMPINGING LIQUID JETS: EFFECT OF VISCOUS, MARANGONI AND SHEAR-THINNING STRESSES

A Dissertation

Submitted to the Faculty

of

Purdue University

by

Jiakai Lu

In Partial Fulfillment of the

Requirements for the Degree

of

Doctor of Philosophy

December 2014

Purdue University

West Lafayette, Indiana

To my grandpas

# ACKNOWLEDGMENTS

First and formost, I would like to express my gratitude to my advisor, Professor Carlos M. Corvalan, for his guidence and encouragement through the years that I spent at Purdue University. It was his guidance that led me into this amazing research field, and it was his knowledge and wisdom that helped me become a scientist and engineer. Without his incredible patience and continuous encouragement, I would not have gone this far.

I would also like to thank Professor Osvaldo H. Campanella, Professor Paul E. Sojka and Professor Stephen Heister for serving on my advisory committee and shearting their valuable comments and insights in my research. It has been an wonderful and lucky journey for me during my study and work at Purdue University under the guidence of these people.

I would like to express my deepest gratitude and love to my parents and family for their everlasting love and support. Also special thanks goes to all my friends and colleagues at Purdue University for their help and support.

Finally, I would like to thank the U.S. Army Research Office under the Multi-University Research Initiave (MURI) project, the USDA Cooperative State Research, Education and Extension Service Air Quality Program and Purdue Research Foundation (PRF) for their fincial support.

TABLE OF CONTENTS

# LIST OF TABLES

# LIST OF FIGURES

Figure Page

Figure Page

Figure Page

Figure Page

Figure Page

# ABSTRACT

Jiakai Lu Ph.D., Purdue University, December 2014. Interfacial dynamics of drop coalescence and impinging liquid jets: effect of viscous, Marangoni and shear-thinning stresses. Major Professors: Carlos M. Corvalan Associate Professor, Department of Food Science and Paul E. Sojka Professor, School of Mechanical Engineering.

The free-surface dynamics of drop coalescence and that of impinging liquid jets have both fundamental interest and practical importance in processes ranging from crop spraying and the processing of food emulsions to the atomization of fuel and propellants in combustion and propulsion engines. These processes frequently involve the use of complex fluids — shear-thinning or viscoelastic non-Newtonian liquids, which often contain surfactants either as additives or as contaminants. This thesis reports high-fidelity simulations of unsteady free-surface flows of complex fluids. The objective is to advance the understanding of the free-surface dynamics of drop coalescence and liquid jet impingement when viscous, surfactant and shear-thinning effects are important. Simulations in this thesis enabled, for the first time, a comprehensive numerical analysis of the coalescence of surfactant-laden drops after the merging drops make contact. The analysis reveals how interfacial (Marangoni) stresses induced by uneven accumulation of surfactant control the rate at which the drops coalesce by modulating the pull of surface tension on the tiny meniscus bridge joining the drops. Simulations also enabled the analysis of the unsteady free-surface dynamics of impinging viscous and shear-thinning liquid jets. Results demonstrate that viscous and shear-thinning stresses profoundly affects the impingement dynamics — in particular the velocity and thickness of the resulting radially expanding liquid sheet — by modifying the pressure developed in the impact region.

# 1. INTRODUCTION

## 1.1 Overview

The general subject of this thesis is the physics of multiphase flows of the sort encountered in spray and atomization systems. In this context, the focus is on the free-surface dynamics of drop coalescence and impinging liquid jets.

Drop coalescence — the process during which a drop merges another — is a phenomenon ubiquitous in everyday life. It plays a critical role in nature, as in the coalescence process that produces raindrops, and in many important technological processes involving dense concentration of drops. Examples of these processes range from spray drying, crop spraying and food emulsification in the food and agriculture industry to fuel atomization in propulsion engines for space and defense technologies. Recently, drop coalescence has also became central to novel analytical technologies that involve the manipulation and mixing of tiny droplets in nano and microfluidic devices.

Impinging laminar liquid jets, upon collision, form a thin, radially expanding liquid sheet. These free-surface dynamics underline important applications ranging from industrial coating to heat transfer technologies for high heat flux cooling and heating. Moreover, the eventual fragmentation into drops of the expanding liquid sheet is of direct interest to the science based design of spray and atomization systems including spray painting, fuel atomization in internal combustion engines, and propellant atomization in rocket engines.

Besides involving simple, low-viscosity liquids such as water, processes and technologies frequently involve viscous liquids with complex rheological and interfacial properties. Common examples include paints, agrochemicals, food emulsions, polymeric solutions and, more recently, gelled propellants for rocket and missile engines.

These complex fluids are typically viscous liquids, which may exhibit non-Newtonian elastic or shear-thinning rheological properties, and contain additives or contaminants with surface active properties (surfactants).

This thesis develops methods for the accurate numerical analysis of nonlinear free-surface flows, including fluids with complex rheological and interfacial properties.

## 1.2 Synopsis

The overall objective of this research is to better understand the free-surface dynamics of drop coalescence and impinging liquid jets in cases in which viscous, surfactant and shear-thinning effects are important.

This thesis is separated into three parts. The first part presents a numerical analysis of the coalescence of surfactant-laden drops, the second part examines the impingement of viscous liquid jets, and the third part extends the analysis to the impingement of shear-thinning liquid jets.

### 1.2.1 Coalescence of Surfactant-laden Drops

Drop coalescence is a familiar event in both nature and technology, from spray and atomization systems to the production of food emulsions. It is well known that surfactants — which are ubiquitous contaminants and routinely used as industrial additives — play an important role in preventing drop coalescence. Little is known, however, about the mechanisms of coalescence after the surfactant-laden drops make contact.

In chapter 2 these mechanisms are analyzed using high-fidelity direct numerical simulation (Fig. 1.1). Results from the simulations show that due to the uneven contraction of the interface the surfactant accumulates on the liquid meniscus bridge joining the drops. Simulations further reveal that the surfactant accumulation is hampered by Marangoni stresses induced, in turn, by the uneven surfactant distribution. This study reveals for the first time how these entwined mechanisms control the rate

at which the drops coalesce by modulating the pull of surface tension on the meniscus bridge.

Chapter 2 contains both text and figures from a published manuscript entitled "Coalescence of viscous drops with surfactants." (2012, Chemical Engineering Science, 78, 9–13), the article is a product of joint efforts between Dr. Carlos M. Corvalan and myself.

### 1.2.2 Impingement of Viscous Liquid Jets

The impingement of low-viscosity liquid jets has been studied extensively for over a century due to their fundamental scientific interest and their practical importance in spray and atomization technologies. However, the role of the fluid viscosity on the impingement of viscous liquid jets is not very well known despite the fact that viscous liquids are common in spray and atomization processes ranging from spray drying in the food industry to the atomization of gelled propellants in rocket engines.

Section 3.1 reports direct numerical simulations that enable a detailed analysis of the influence of viscosity on the impingement dynamics. The simulations solve the complete Navier-Stokes system governing the free-surface dynamics, and so fully account for the interplay of inertia, viscous and capillary forces. Results demonstrate that the liquid viscosity profoundly affects the impingement dynamics (Fig. 1.2). The simulations show that the collision of viscous liquid jets generates a fluid sheet that thins at a rate $r^{-1}$ with the distance $r$ from the impact point at intermediate viscosities, in contrast to the inertial case in which the sheet thins at a faster rate $r^{-2}$. As the viscosity increases further, the fluid sheets become thicker and more uniform, and contrary to the inertial case, the velocity of the sheets are lower than the velocity of the jets. Results further reveal that due to viscous stresses the impact pressure generated by the collision of viscous liquid jets scales as $Re^{-1}$, where $Re$ is the jet Reynolds number.

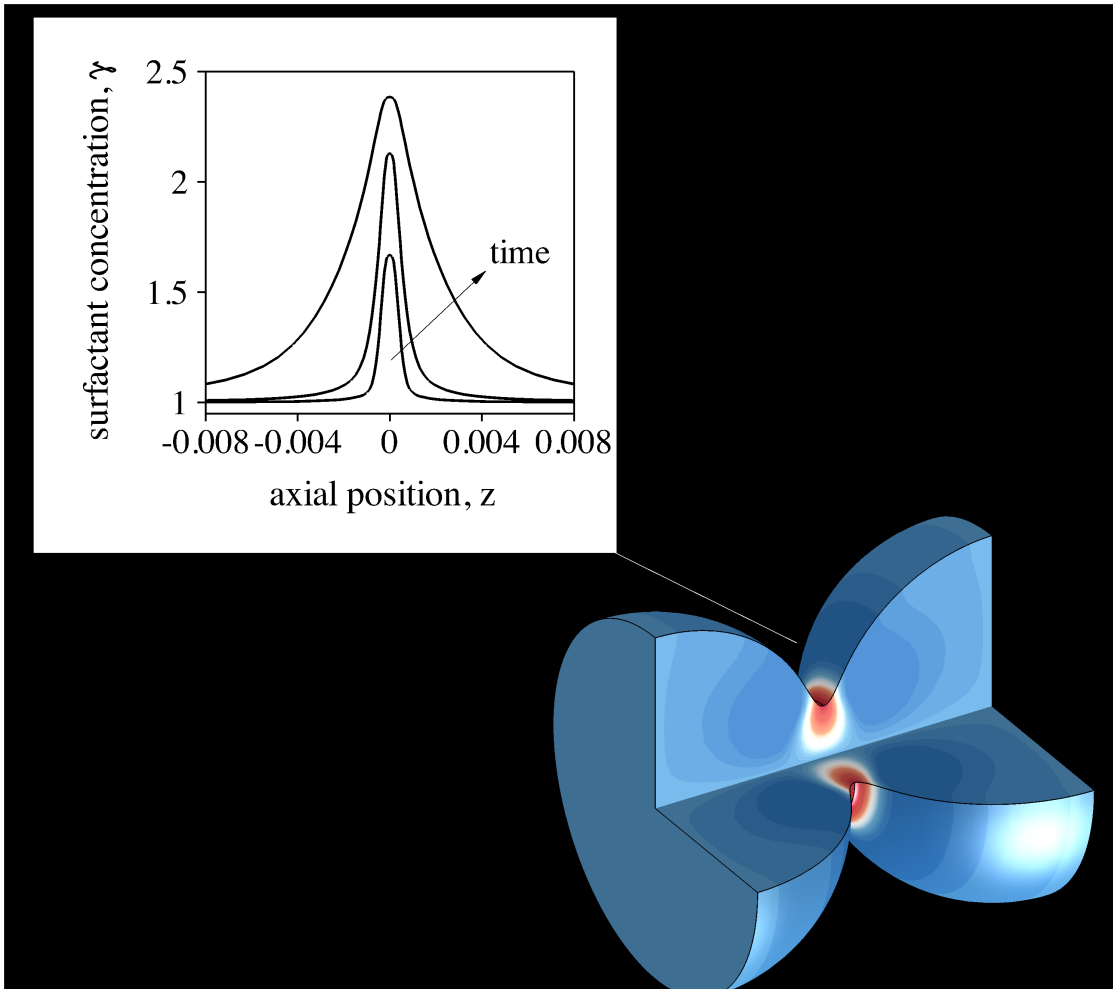


Figure 1.1. **Coalescence of viscous drops with surfactant.** Simulations show that due to the uneven contraction of the interface, surfactants accumulate on the liquid meniscus bridge between the merging drops. The resulting tangential Marangoni stresses control the rate at which the drops coalescence.

Chapter 3 contains both text and figures from a published manuscript entitled "Influence of viscosity on the impingement of laminar liquid jets." (2014, Chemical Engineering Science, 119, 182–186), the article is a product of joint efforts between Dr. Carlos M. Corvalan and myself.

### 1.2.3 Impingement of Shear-thinning Liquid Jets

Due to its fundamental scientific interest and numerous applications in spray and atomization systems, the physics of impinging liquid jets has been extensively studied since the pioneering works by Savart (1833) and Taylor (1960). However, most studies have only considered the impingement of jets of simple liquids such as water, where rheology plays no role. Therefore, little is known about the impingement of complex fluid jets, despite their importance in industrial and defense technologies.

Section 3.2 extends the analysis of section 3.1 to jets of complex fluids. Specifically, high-fidelity numerical simulations are used to study the impingement of shear-thinning liquid jets as a model system for jets of non-Newtonian liquids frequently used in industrial and defense technologies, such as paints, food emulsions, polymeric solutions, and gelled propellants. Computations reveal that during the impingement of jets of complex fluids, shear stresses create a region of comparatively low viscosity in the vicinity of the impact point. As a consequence, shear-thinning sheets are thinner and flow faster than the corresponding Newtonian ones. Shear thinning also enhances the growth of the toroidal rim bounding the resulting expanding liquid sheet (Fig. 1.3). Together, these results highlight the large impact of the fluid rheology on the dynamics of jet impingement. This study is anticipated to be a starting point for more sophisticated rheological models for the impingement of jets of viscoelastic fluids.

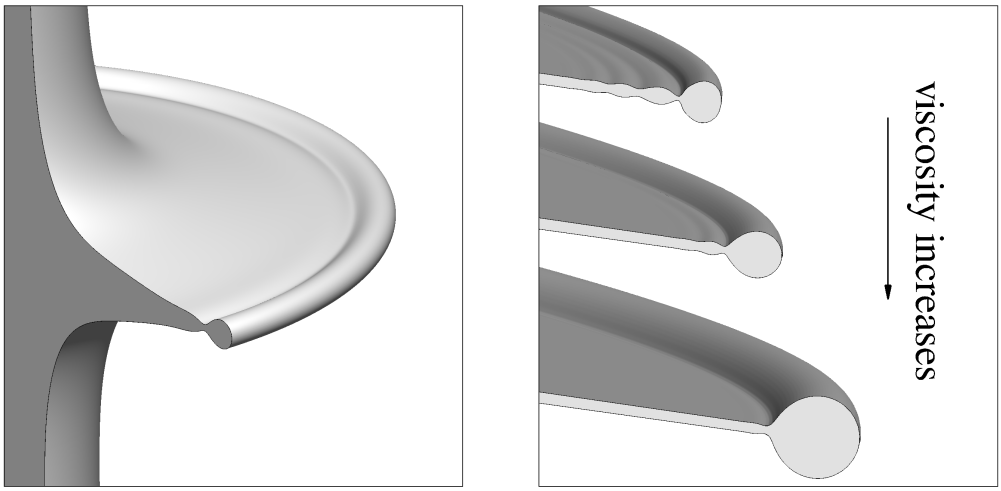


Figure 1.2. **Impingement of viscous liquid jets.** Direct numerical simulation enabled a detailed analysis of the influence of viscosity on the dynamics of opposed impinging liquid jets. The liquid viscosity profoundly affects the impinging dynamics, including the velocity and thickness of the resulting expanding sheet and its bounding rim.

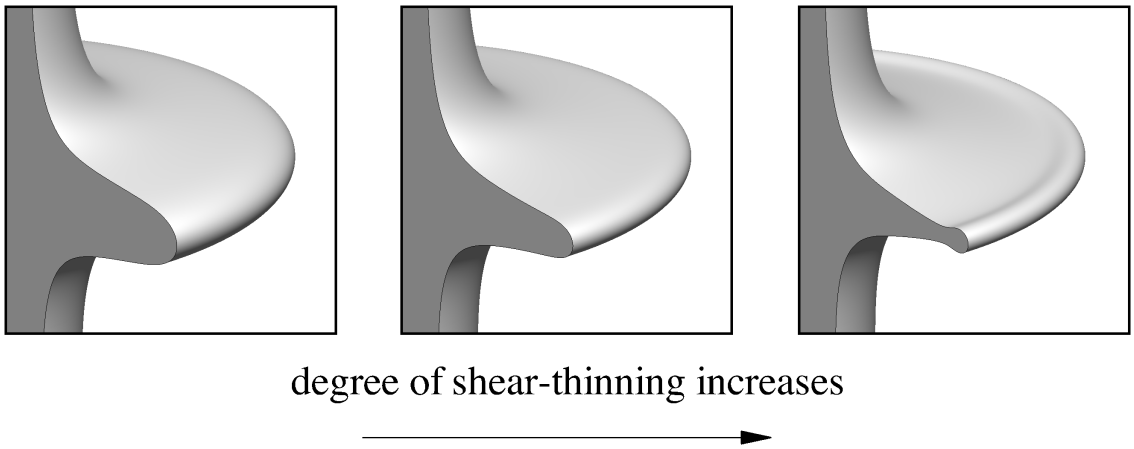


Figure 1.3. **Effect of shear-thinning on sheet and toroidal rim formation during jet impingement.** Formation of axisymmetric expanding sheets and toroidal rim during jet impingement of shear-thinning liquids.

## 1.3 Background

### 1.3.1 Drop Coalescence

When two drops come into contact, driven by an uneven surface tension force, they either bounce back or merge into one larger drop, the latter behavior is called drop coalescence. Drop coalescence is a common yet important phenomenon found in nature as well as in many industrial applications and modern technologies.

In nature, for example, the droplet size distribution of rain formation is largely dependent on the process of drop coalescence (Kovetz and Olund, 1969, Thomason and Newall, 1885). Similarly, the quality of spray and atomization processes are also largely affected by drop coalescence (Lefebvre, 1988). The spray and atomization process appears in a wide range of industrial applications such as spray painting, fuel injecton systems, and spray drying. Furthermore, the ability to manipulate the drops by way of coalescence has proven effective in many droplet based microfluidic systems as discussed by Xu et al. (2014).

Although studies of drop coalescence were reported as early as Sartor (1969) and Thomson and Newall (1885) over a century ago, a detailed picture of the mechanisms of coalescence immediately after the drops are brought into contact has only been studied recently, owing to the advancement of modern technologies.

The growth rate of the liquid neck connecting the two merging drops is the focus of many studies on the dynamics of drop coalescence (Aarts et al., 2005, Eggers et al., 1999, Hopper, 1984, Paulsen et al., 2011, Thoroddsen et al., 2008, Yao et al., 2005).

Hopper (1984) studied the two-dimensional coalescence of two equal cylinders under creeping viscous flow surrounded by quiescent ambient gas. Through rigorous mathematical analysis, the author obtained the evolution of interfacial shapes of two-dimensional drop coalescence. The author also proposed a scaling for the growth rate of viscous two-dimensional drop coalescence as a function of the radius of the liquid neck.

This two-dimensional model was later proven to be valid in a three-dimensional extension by Eggers et al. (1999). By asymptotic analysis of the Stokes equation, the authors demonstrated that, in the regime dominated by viscous effects, the speed of coalescence (the growth rate of the liquid neck) depends logarithmically on the radius of the liquid bridge, consistent with the results from Hopper (1984). Eggers et al. (1999) also suggested that the characteristic length of the flow is extremely small in the early stage of the drop coalescence, due to highly localized flow around the liquid neck. Therefore, viscous forces always dominate the dynamics at the early stage of drop coalescence regardless of the material properties of the drops.

Revealing the detailed mechanism of the dynamics of drop coalescence in its early stages is difficult because the time scale of the process is very small, which makes it hard to obtain a satisfying temporal resolution experimentally. Using advanced high-speed imaging systems, Aarts et al. (2005), Paulsen et al. (2011), Thoroddsen et al. (2008), and Yao et al. (2005) studied the dynamics of drop coalescence, in particular the growth of the liquid neck connecting the drops after the onset of coalescence. In these experiments, drops were brought together with negligible speed until coalescence. In order to obtain a relative higher temporal resolution, small drops of very viscous fluids were used, such as silicon oil drops with a viscosity as high as $10^5$ $cS$ (Yao et al., 2005), and 96% glycerin/water mixture (Thoroddsen et al., 2008). High-fidelity computing algorithms were employed in the studies of Duchemin et al. (2003), Martinez-Herrera and Derby (1995), Oguz and Prosperetti (1989), and Paulsen et al. (2012). These studies enabled detailed analysis of the physics of the drop coalescence after the contact of the two liquid drops.

However, the studies mentioned above only focused on the dynamics of drop coalescence between a pair of drops of the same Newtonian liquid. In many applications, such as micro-mixing, coalescence occurs between two miscible liquids that have different surface tension (Luo et al., 2011). Furthermore, surface tension difference may also occur due to temperature difference between the drops (Xu et al., 2012).

When there exists a mismatch in surface tension, a force per unit length is induced. This force is locally tangential to the interface in the direction of the surface tension gradient. As a consequence, flow is pulled from the region of low surface tension to the region of high surface tension. This is known as Maragoni effect, which affects the fluid dynamics on the free surface in addition to the capillary stresses due to the curvature of the fluid interface (Marangoni, 1871).

The critical influence of surface-tension gradients induced by the mismatch of the surface tension between the coalescence of two different but miscible fluids with clean interfaces has been highlighted in recent works by Thoroddsen et al. (2007) and Blanchette et al. (2009).

Using high speed imaging techniques, Thoroddsen et al. (2007) studied coalescence between a 90% ethanol drop and a water droplet. The authors found that, due to Marangoni stress, a capillary wave was induced that travels from the drop of low surface tension to the drop of high surface and that the growth rate of the neck radius is controlled by the droplet of low surface tension.

Blanchette et al. (2009) combined both experimental methods and high fidelity numerical simulation to study the coalescence between a droplet and a reservoir of two different but miscible fluids. Results showed that the gradient of surface tension, and the corresponding Marangoni stress, play an important role in dividing the dynamics of drop coalescence into three distinct regions: coalescence, partial coalescence and non coalescence. In both studies (Blanchette et al., 2009, Thoroddsen et al., 2007), drop coalescence was largely affected by the Marangoni stress due to the surface-tension gradient developed between the drops.

The Marangoni stresses induced by surface tension mismatch are essentially different to those raised by the presence of insoluble surfactant. Surfactant is a surface active agent that lowers the surface tension of a fluid. When insoluble surfactant is applied on the fluid interface, surface tension gradient may be induced due to the transport of surfactant through convection, diffusion and the contraction or dilation of the fluid interface. These surface tension gradient induces Marangoni stresses. In

addition, the interfacial flow field that determines the transport of surfactant will in turn be largely affected by the Marangoni stresses. Therefore, the dynamics of coalescence of surfactant-laden drops is largely affected by these entwined mechanisms.

Although the coalescence of surfactant-laden drops has been studied for a long time, most studies of surfactant-laden drop coalescence focused on the influence of surfactants on the drainage of the fluid film separating the drops just before coalescence (Chesters and Bazhlekov, 2000, Dai and Leal, 2008, Hodgson and Lee, 1969). It has been shown experimentally (Hodgson and Lee, 1969) and numerically (Chesters and Bazhlekov, 2000, Dai and Leal, 2008) that the beginning of drop coalescence is significantly delayed with the presence of insoluble surfactants. Marangoni stresses induced by the surface tension gradient hampers the drainage of the thin fluid film between the drops and so to delay the drop coalescence. The importance of the effect of surfactant on the dynamics of drop coalescence after the drops make contact has never been studied.

### 1.3.2 Jet Impingement

The impingement of liquid jets has been studied for more than a century (Savart, 1833). When two liquid jets hit each other, a thin fluid sheet is formed upon the collision. The sheet then expands and eventually disintegrates into fluid filaments and drops because of the competition between inertia, viscous, capillary, and aerodynamic forces. Impingement of liquid jets are used in a wide range of applications including micro-mixing, fluid extraction, crop spraying, food emulsions, the atomization of fuel in combustion engines, and the atomization of propellants in rocket engines for space and defense technologies (Ashgriz, 2011, Bremond and Villermaux, 2006, Clanet and Villermaux, 2002, Lefebvre, 1988, Mahajan and Kirwan, 1996, Ryan et al., 1993, Sutton, 1992, Villermaux et al., 2013).

There are two major focuses in the studies of jet impingement. The first focus is on the mechanism leading to the break up of the fluid sheet. The second focus is on the

fundamental dynamics of jet impingement, which includes the analysis of the shape, thickness, and velocity distribution of the sheet resulting from the jet impingement.

In response to the first focus, the pioneering work by Savart (1833) revealed two distinct regimes of sheet break up: one is a smooth sheet regime, where disintegration occurs at the boundary of the sheet. The other is a flapping sheet regime, where the break up of the sheet is due to the waves on the fluid interface.

These regimes were later studied experimentally by Heidman et al. (1957), Huang (1970), Taylor (1960), and by Clanet and Villermaux (2002, a,b). It is now known that the break up regions observed by Savart (1833) are characterized by the Weber number of the system. If the Weber number is smaller than 1000, which corresponds to the smooth sheet regime in the work of Savart (1833), then the break up is due to a hydrodynamic instability known as absolute instability (Lin and Jiang, 2003). In this region, a smooth sheet extends with a bounding rim to a distance, where the rim disintegrates from the sheet due to a balance between the inertia of the fluid and the capillary force. This radius is now known as Taylor radius. If the Weber number is larger than a approximately 1000, which corresponds to the flapping sheet region in the work of Savart (1833), the break up is due to strong wavy motion on the fluid sheet far from the impact region due to an aerodynamic instability known as convective instability (Lin and Jiang, 2003).

Also in the high Weber number region, experiments from Dombrowski and Hooper (1964), Huang (1970) and Anderson et al. (1998) showed the formation of waves on the interface and disturbances in the fluid field close to the impact region. These waves, known as impact waves, were observed on the sheet within a few jet radii away of the impact point. The characteristic wave length was about one jet diameter. However, the mechanism of impact wave formation is not well known. It is suspected that these waves can be formed either as a result of an oscillating stagnation point or of fluctuations in the impinging jets Anderson et al. (1998).

To better understand the break up mechanism of the fluid sheets, and to predict the size of the droplet formed from the break up, Ibrahim (1998), Squire (1953)

and Weihs (1978) proposed models based on linear stability analysis. However these models require the fundamental study of the jet impingement such as shape, thickness and velocity distribution of the resulting fluid sheet.

The second focus of jet impingement was pioneered by Taylor (1960). A notable finding from Taylor (1960) and Ranz (1959) is that a sheet formed by impingement of inviscid liquid jets is originated from the point of impact. The velocity of the sheet is exactly the same as the jet velocity. Consequently, the thickness of the fluid sheet decreases radially and is inversely proportional to the radial position measured from the impact point.

The theoretical model describing the thickness and shape of the fluid sheet proposed by Taylor (1960) was later refined by Hasson and Peck (1964) and Ibrahim and Przekwas (1991). These studies provided valuable information for the later the stability analysis (Mallory and Sojka, 2014, Ryan et al., 1993)

In most studies, the focus was on the dynamics of impingements of inviscid Newtonian liquids. However, a growing interest in the use of high viscosity complex fluids such as paints, food emulsions, polymeric solutions and gelled propellants (Baek et al., 2011, Chen et al., 2012b, Kampen et al., 2007, Yang et al., 2012) requires understanding the dynamics of jet impingement of viscous fluid.

However, very little is known about the dynamics of jet impingement of viscous liquids. Lienhard and Newton (1966) pioneered the study of viscous effect on sheet thickness distribution of a radially expanding fluid sheet formed by jet impingement. The authors solved analytically the momentum equation governing the fluid dynamics of the liquid sheet in the Stokes limit and revealed that viscous stresses, resulting from the tangential expansion of the fluid sheet, slowed the fluid in a way that leads to a fluid sheet of constant thickness. However, without a full knowledge of the fluid dynamics at the impact region, where the flow changes direction from radially oriented to axially oriented, the authors cannot predict the actual thickness of the fluid sheet.

To model the fluid sheet formed by jet impingement of viscous fluids, Dombrowski and Johns (1963) developed a two-dimensional linear stability model to study a vis-

cous planar liquid sheet of constant thickness. The model fully considered the interplay between inertia, viscous, capillary and aerodynamics forces. Results showed that if the thickness of the initial fluid sheet or viscosity of the liquid increases, then the wave number that corresponds to the largest growth rate of the disturbance on the sheet decreases, which hints at larger final drops.

Experimental studies on the jet impingement of viscous fluids were also carried out. Choo and Kang (2001) used glycerol solutions with different concentrations to study the effect of viscosity on the thickness of the fluid sheets formed by jet impingement experimentally. The highest viscosity of the working fluids was 0.0194 $Pa.s$ (68% Glycerol), almost 20 times larger than water. Although the authors found that the thickness of the resulting sheets increases as the viscosity increases, the thinning rate of the sheet thickness is the same as the inviscid case.

Shortly after, Lai et al. (2005) also studied the effect of the viscosity on the atomization characteristics of jet impingement. Mixture of water, sugar and alcohol used in the experiments provided a wide range of viscosities up to 40 times larger than that of water. Although the authors did not directly report the thickness of the fluid sheet, results showed that drops resulting from the sheet of more viscous fluid are of larger size, coinciding with the prediction made by Dombrowski and Johns (1963)

Most recently, Villermaux et al. (2013) attempted to study the effect of viscosity on jet impingement systematically by mimicking the work of Savart (1833). A solution of maltodextrin mixed with water was used, which can reach a 300 times higher viscosity than if water were used. The authors also reported a thicker sheet and a delay of the critical Weber number that distinguishes the smooth sheet break up region and wavy sheet break up region reported in the inviscid cases (Clanet and Villermaux, 2002, Huang, 1970).

As mentioned before, the high viscosity and complex fluids that are of great interest exhibit more than just high viscous behaviour; they are in fact non-Newtonain fluids, or shear-thinning in nature. A shear-thinning fluid, such as ketchup, is when the fluid undergoes a large rate of deformation and the viscosity of the fluid decreases.

The effect of viscosity on the dynamics of jet impingement demonstrated in (Choo and Kang, 2001, Lai et al., 2005, Villermaux et al., 2013) indicates that if the local viscosity of the fluid in the flow field varies, such as shear-thinning fluids, the dynamics of sheet formation and the subsequent disintegration of the sheet can be largely altered. Although very little literature exists for the effect of fluid rheology on jet impingement, some of the most recent studies highlighted the importance of non-Newtonain fluid in the dynamics of jet impingement.

Lots of studies were made in order to discover and characterize different spray patterns of jet impingement of non-Newtonian fluids. New patterns of the spray such as fluid web break up Miller et al. (2005), ray shaped pattern and ligament structures Kampen et al. (2007) were reported for the jet impingement of various gelled fluids that are non-Newtonian in nature. These study suggest that sprays from the impingement of gelled fluids show substantially less break-up than their non-gelled counterparts (water) under similar test conditions. (Chojnacki and Feikema, 1994, Negril and Ciezki, 2010)

To better understand the underlying physics of non-Newtonian shear-thinning jet impingement, various theoretical models based on two dimensional linear stability analysis were proposed (Chojnacki, 1997, Liu et al., 1998, Mallory and Sojka, 2014).

In these models, Liu et al. (1998) considered a non-Newtonian fluid described by a power law rheological constitutive equation while ignoring the effect of capillary forces. Chojnacki (1997), also assuming a power law fluid, extends the comprehensive model proposed by Dombrowski and Johns (1963), which incorporates inertial, aerodynamic, surface tension, and viscous forces on the fluid sheet. Most recently, Mallory and Sojka (2014), for the first time, used a nonlinear rheological expression, the Carreau-Yasuda model of non-Newtonian liquids, and extended the model of Dombrowski and Johns (1963). Predictions from Mallory and Sojka (2014)'s model for the droplet's size and break up radius showed a better comparison against experiments than the previous existing models.

However, all of these models assume the initial thickness of the sheet to be constant or to have the thickness of an inviscid fluid sheet. Moreover, all of these model ignore the effect of complicated impact dynamics. Therefore, a huge gap exists that requires the fundamental study of impingement of jets of non-Newtonian liquids for the shape, thickness distribution, and velocity distribution of the sheets. The fundamental studies on a resulting sheet have been useful in understanding the physics of jet impingement of Newtonian fluids.

### 1.3.3 Numerical Methods

An accurate analysis of drop coalescence and jet impingement is challenging because there are major complications. The first major complication is that the conservation equations governing the dynamics of the fluid flow of drop coalescence and jet impingement are highly nonlinear. The nonlinearity can be raised due to convective transport of momentum–inertia effect–if it is relatively important. But most importantly, the presence of free surface, complicated and strongly nonlinear boundary conditions are applied, introducing the nonlinearity of the system.

The second major complication is that the location of the free surface is unknown prior to the knowledge of the flow field, which can not be prescribed at the outset and must be computed instead as part of the solution.

The third major complication is the application of complex fluids. In ordinary Newtonian liquids, laminar flow fields of coalescing drops or impinging liquid jets are very complicated already, and if the non-Newtonian effect is present, such as the application with the presence of insoluble surfactant or shear-thinning liquid, fluid flows can be very different and even more complicated.

When insoluble surfactant is present on the fluid interface, surface tension gradient may be induced due to the transport of surfactant through convection, diffusion and the contraction or dilation of the fluid interface. Such a surface tension gradient results in a force per unit length that is locally tangential to the interface in the direction

of the tension gradient. This is commonly known as Marangoni stress, which affects the fluid dynamics on the free surface in addition to the capillary stresses due to the curvature of the fluid interface.

When the liquid has shear-thinning properties, fluid dynamics can be very different than that of the Newtonian fluid dynamics as shown by Vaidya (2010) for the coalescence of drops of shear-thinning fluid and by Miller et al. (2005) and Kampen et al. (2007) for the jet impingement of gelled fluid.

To address these challenges, this thesis develops a numerical algorithm using Direct Numerical Simulation (DNS). In the numerical algorithm, the coupled governing equations (momentum, continuity and convection-diffusion transport equations, if surfactant is present) with the proper constitutive equations are solved simultaneously using the Galerkin finite element method for spatial discretization and an adaptive, implicit predictor-corrector method for temporal integration. To track the deformation of fluid interfaces, the method of Arbitrary Lagrangian-Eulerian (ALE) method of spines proposed by Kistler and Scriven (1983) is employed. This method has been successfully applied in this research group the simulations of other free surface flows such as the capillary instability of the liquid filament of complex fluids (Dravid et al., 2006, Muddu et al., 2012, Xue et al., 2008).

While there are other numerical algorithms capable of simulating fluid flows with free interface including moving grid method (Braess and Wriggers, 2000), level set method (Osher and Fedkiw, 2001) and volume of fluid method (Scardovelli and Zaleski, 1999), there are advantages to using the finite-element method over other methods. One of the advantages is that the global solution of the velocity and pressure fields of the fluid flow are approximated by a finite number of continuous basis functions, making it a complete functional representation from which physical quantities such as strain rates and stresses can be readily obtained. The most important advantage of using finite-element method for the problem of free surface flows is that the weak form of the conservation equation allows the application of the capillary traction condition (Eq. 3.5), in a most physically natural way.

# 2. COALESCENCE OF VISCOUS DROPS WITH SURFACTANTS

Drop coalescence is a familiar event in both nature and technology, from spray and atomization systems to the production of food emulsions. It is well known that surfactants — which are ubiquitous contaminants and routinely used as industrial additives — play an important role in preventing drop coalescence. Little is known, however, about the mechanisms of coalescence after surfactant-laden drops make contact. Here these mechanisms are analysed using high-fidelity numerical simulation. Results from the simulations show that due to the uneven contraction of the interface the surfactant accumulates on the liquid meniscus bridge joining the drops. Simulations further reveal that the surfactant accumulation is hampered by Marangoni stresses induced, in turn, by the uneven surfactant distribution. This study reveals for the first time how these entwined mechanisms control the rate at which the drops coalesce by modulating the pull of surface tension on the meniscus bridge.

This chapter contains both text and figures from a published manuscript entitled "Coalescence of viscous drops with surfactants." (2012, Chemical Engineering Science, 78, 9–13), the article is a product of joint efforts between Dr. Carlos M. Corvalan and myself.

## 2.1 Introduction

When two liquid drops make contact, they coalesce due to the strong surface tension forces developed on the tiny and highly curved meniscus bridge formed between the drops. Drop coalescence is a common phenomenon in nature — as in the coalescence process that produces raindrops (Berry and Reinhardt, 1974, Bowen, 1950) — and central to many important technological processes ranging from crop spraying and

propulsion systems (Yaghoub et al., 2010) to the formation of food emulsions (Bhakta and Ruckenstein, 1997, McClements, 1999).

Although the coalescence of drops has been studied for more than a century (Thomson and Newall, 1885), only recently have advances in high-speed imaging (Aarts et al., 2005, Thoroddsen et al., 2008, Yao et al., 2005) and high-fidelity computing (Duchemin et al., 2003, Martinez-Herrera and Derby, 1995, Oguz and Prosperetti, 1989) enabled a detailed picture of the mechanisms of coalescence immediately after the drops are brought into contact. How surfactants influence these mechanisms is still an open question. Indeed, most studies on surfactant-laden drops focused on the influence of surfactants on the drainage of the fluid film separating the drops just before coalescence (Chesters and Bazhlekov, 2000, Dai and Leal, 2008, Hodgson and Lee, 1969) but it is still unclear how surfactants affect coalescence after the drops make contact. While recent numerical and experimental works by Thoroddsen et al. (2007) and Blanchette et al. (2009), highlight the critical role played by surface-tension gradients during coalescence of two different liquids, such gradients, arising from the surface-tension mismatch between the merging liquids, are fundamentally different from those induced by the presence of surfactants.

To address this issue, the mechanism of coalescence of surfactant-laden drops is studied here using direct numerical simulation; that is, solving the free-surface hydrodynamics coupled to the convective-diffusion equation that governs the surfactant transport at the phase interface. Results from the simulations reveal that due to the uneven contraction of the phase interface, surfactants accumulate on the liquid meniscus bridge between the drops. At the same time, interfacial motion induced by surface-tension gradients (Marangoni stresses) opposes the accumulation process by dragging surfactant away from the liquid bridge. This study reveals for the first time how these competing surfactant-induced mechanisms control the rate of drop coalesce by modulating the pull of surface tension on the meniscus bridge.

Section 2.2 summarizes the conservation equations and boundary conditions governing the fluid dynamics of coalescence of surfactant-laden drops. Section 2.3 details

the algorithm developed for the direct numerical simulation (DNS) of this nonlinear free-surface flow. The algorithm accurately accounts for the coupled viscous, inertial, capillary, and surfactant effects by simultaneously solving the full system of governing equations using a finite-element method with an arbitrary Lagrangian-Eulerian scheme for tracking the deforming interface. Section 2.4 reports predictions from the simulations which enable detailed characterization of the mechanisms of coalescence of surfactant laden drops. Finally, section 2.5 summarizes the main findings, and discusses limitations of the simulations and developments that are still needed.

## 2.2 Governing Equations

### 2.2.1 The Fluid Mechanics of Drop Coalescence

The dynamics of surfactant-laden drop coalescence is analyzed in this chapter by following the time evolution of two half-drops of an incompressible Newtonian liquid of density $\rho$ and viscosity $\mu_0$ covered with an insoluble surfactant. The drops are initially connected by a narrow neck as sketched in Figure 2.1.

The problem is described below in dimensionless form using the drop radius $a$ as length scale, $\tau = a\mu_0/\sigma_0$ as viscous time scale, and $\sigma_0/a$ as stress scale. The local, time-dependent concentration of surfactant $\gamma(\mathbf{x}, t)$ is measured in units of the initial concentration $\gamma_0$. Similarly, the corresponding local, time-dependent surface tension $\sigma(\mathbf{x}, t)$ is measured in units of the initial surface tension of the drops $\sigma_0$. Both the initial concentration of surfactant $\gamma_0$ and the corresponding initial surface tension $\sigma_0$ are considered spatially uniform at time $t = 0$.

The evolution of the velocity $\mathbf{v}(\mathbf{x}, t)$ and pressure $p(\mathbf{x}, t)$ in the drops are calculated by solving the full dimensionless axisymmetric Navier-Stokes system describing the conservation of mass

$$\nabla \cdot \mathbf{v} = 0, \tag{2.1}$$

and momentum

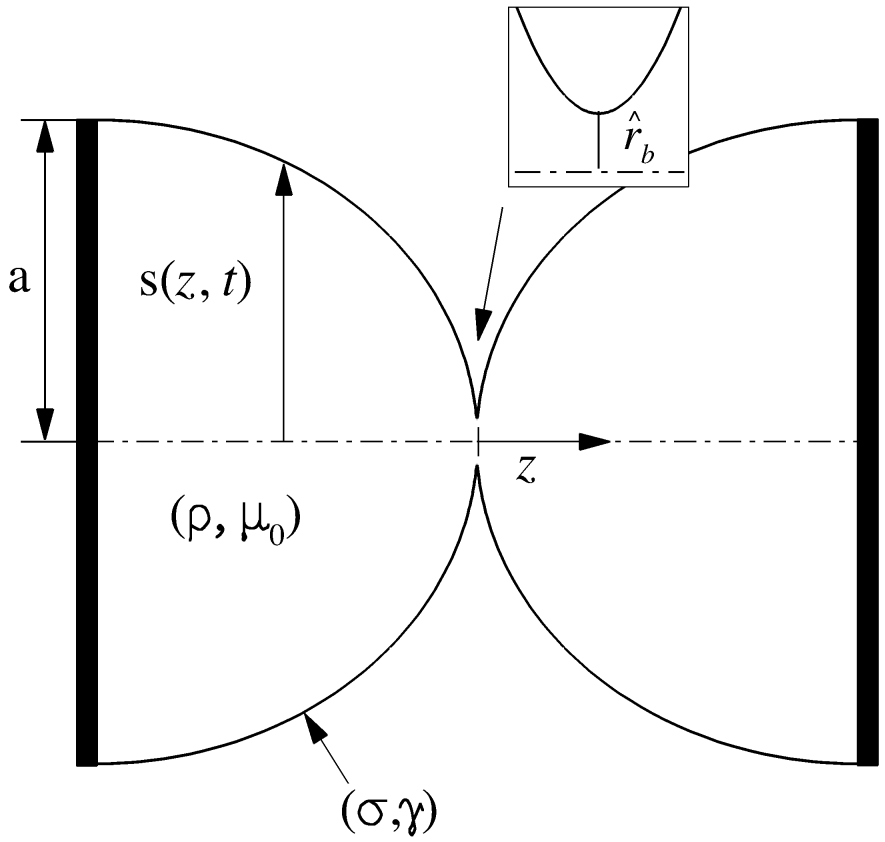


Figure 2.1. **Schematic of the coalescing drops.** The shape of the axisymmetric drop interface is $S(z,t)$. The density of the drops is $\rho$ and the viscosity $\mu_0$. The time-dependent local concentration of surfactant is $\gamma$ and the local dynamic surface tension is $\sigma$; the initial surface tension $\sigma_0$ corresponds to an spatially uniform surfactant concentration $\gamma_0$.

$$Re\left(\frac{\partial \mathbf{v}}{\partial t} + \mathbf{v}\cdot\nabla\mathbf{v}\right) = \nabla\cdot\mathbf{T}. \tag{2.2}$$

The Navier-Stokes system is solved consistent with the balance of forces at the drop interface (Slattery, 1990)

$$\mathbf{T}\cdot\mathbf{n} = 2\mathcal{H}\ \sigma\ \mathbf{n}, \tag{2.3}$$

where

$$\mathbf{T} \equiv -p\mathbf{I} + (\nabla\mathbf{v} + \nabla\mathbf{v}^T) \tag{2.4}$$

is the Cauchy stress tensor, $\mathcal{H}(\mathbf{x},t)$ is the local interfacial curvature, and $\mathbf{n}(\mathbf{x},t)$ the unit vector normal to the interface. For details on the calculation of the curvature and unit normal vector see Equations (2.26) and (2.31) in section 2.3.

This study considers the coalescence of small drops, neglecting the effect of gravity. It is also assumed that the adjoining phase is a dynamically inert gas, and that mass transfer to and from the gas phase can be neglected, as expressed by the kinematic condition

$$\mathbf{n}\cdot(\mathbf{v} - \mathbf{v}_s) = 0, \tag{2.5}$$

where $\mathbf{v}_s(\mathbf{x},t)$ is the velocity of the free interface. The choice of characteristic viscous scales yields a characteristic velocity $\sigma_0/\mu_0$, and thus the Reynolds number in Equation (2.2) is

$$Re \equiv \frac{\rho\sigma_0 a}{\mu_0^2}. \tag{2.6}$$

Following Martinez-Herrera and Derby (1994, 1995) and Eggers et al. (1999), the simulations start with the interfacial shape $S(z, t=0)$ given by the exact solution by Hopper (1984) for the coalescence of two-dimensional (cylindrical) drops. No-slip and no-penetration conditions

$$\mathbf{v} \cdot \mathbf{n} = 0, \ \mathbf{v} \cdot \mathbf{t} = 0, \tag{2.7}$$

where $\mathbf{t}(\mathbf{x}, t)$ is the unit tangential vector, were imposed on the solid surfaces supporting the drops. The circular contact lines where the fluid interface intersects the solid surfaces (Fig. 2.1) were considered pinned, static separation lines. On the plane and axis of symmetry the shear-stress as well as the normal velocity were set to zero because of the non-flux condition. In addition, on the plane of symmetry $z = 0$ the interfacial slope vanishes.

### 2.2.2 Surfactant Transport and Marangoni Stress

Due to the presence of surfactant, the balance of forces at the interface discussed in Equation (2.3) must be extended to consider not only the normal capillary forces $2\mathcal{H}\sigma\mathbf{n}$ but also the tangential forces $\nabla_s\sigma$ induced by gradients of surface tension at the interface (Slattery, 1990):

$$\mathbf{T} \cdot \mathbf{n} = 2\mathcal{H}\sigma\mathbf{n} + \nabla_s\sigma. \tag{2.8}$$

The first term in the left side of Equation (2.8) is the normal capillary stress, and the second term represents the tangential Marangoni stress (Scriven and Sternling, 1960). Both, through the dynamic surface tension $\sigma(\mathbf{x}, t)$, depend on the local distribution of surfactant $\gamma(\mathbf{x}, t)$ along the interface which is calculated here by solving the full convection-diffusion transport equation (Aris, 1962, Stone, 1990, Wong et al., 1996)

$$(\partial\gamma/\partial t)_s + \gamma(\mathbf{v}_s \cdot \mathbf{n})(\nabla_s \cdot \mathbf{n}) + \nabla_s \cdot (\gamma\mathbf{v}_s \cdot \mathbf{t})\mathbf{t} - Pe^{-1}\nabla_s^2\gamma = 0, \tag{2.9}$$

where $\mathbf{t}$ is the unit vector tangent to the interface (see Eq. 2.30) and $\nabla_s$ is the surface gradient operator, which is calculated as the projection

$$\nabla_s \equiv (\mathbf{I} - \mathbf{nn}) \cdot \nabla \tag{2.10}$$

where $\mathbf{I}$ is the unit tensor.

The transport Equation (2.9) includes changes in surfactant concentration due to convection, diffusion and changes in surface area with the surfactant considered insoluble. The dimensionless number $Pe$ in the diffusion term is the Peclet number

$$Pe \equiv (a^2/D)/\tau \tag{2.11}$$

where $D$ is the surfactant diffusion coefficient, and $\tau = a\mu_0/\sigma_0$ the characteristic viscous timescale. A large Peclet number $Pe = 10^3$ is set in the simulations presented in this chapter because the timescale for surfactant diffusion $a^2/D$ is typically much larger than the viscous timescale $\tau$. In addition, following Hansen et al. (1999), Campana et al. (2004) and Dravid et al. (2006) a linear dependence of the surface tension on the surfactant concentration

$$\sigma = 1 - \mathrm{Ma}(\gamma - 1), \tag{2.12}$$

around the initial dimensionless concentration $\gamma = 1$ was assumed. The Marangoni (or Elasticity) number $Ma$ characterizes the surfactant strength (Campana et al., 2004, Hansen et al., 1999) and can be of order unity or larger (Halpern and Grotberg, 1993, Yap and Gaver, 1998).

## 2.3 Direct Numerical Simulation of Free-surface Flows with Surfactants

This section describes the finite element algorithm developed for the numerical simulation of the coalescence of Newtonian drops with surfactants. This algorithm is extended in chapter 3 to include non-Newtonian fluids.

The governing Equations (2.1), (2.2), (2.5), and (2.9) that couple the free surface hydrodynamics and the interfacial mass transport were solved simultaneously for velocity $\mathbf{v}(\mathbf{x}, t)$, pressure $p(\mathbf{x}, t)$, surfactant concentration $\gamma(z, t)$, and location of the free interface $S(z, t)$ using direct numerical simulation (Scardovelli and Zaleski, 1999).

The numerical simulation is based on the finite element method extended with the Arbitrary Lagrangian-Eulerian method of spines pioneered by Kistler and Scriven (1983) to parametrize the deforming drop interface. The interfacial surfactant transport is incorporated to the algorithm following the procedure described by Campana et al. (2004). The algorithm was derived from others that were previously tested and successfully applied in this research group to analyze the capillary breakup into drops of Newtonian and non-Newtonian liquid jets with surfactants (Muddu et al., 2012, Xue et al., 2008).

The complexity of the numerical algorithm is considerable because the problem of surfactant-laden drop coalescence is highly nonlinear and strongly coupled. Indeed, the problem is governed by a highly nonlinear system of partial differential equations in a continually deforming domain bounded by a free interface. The location and shape of the free surface is unknown a priori and entangled to the computation of the flow. The shape (curvature) of the interface drives the flow through capillarity, and the flow, in turn, determines the location of the interface, thus leading to a highly coupled free surface problem.

With the Arbitrary Lagrangian-Eulerian method of spines, the irregular moving boundary $S(z,t)$ enclosing the flow domain $V(t)$ is handled accurately and effectively by parametrization of the free phase interface. The location of the free interface is parametrized by a set of oriented lines called spines, as sketched in Figure 2.2.

Each spine $m$ is defined by a base point $\mathbf{x}_B^m$ from which a straight line (the spine) travels in a direction given by a unit vector $\mathbf{e}^m$. The spine $m$ intersects the fluid interface at a distance $h^m$ from the base point. Using the distance $h^m$, the $m$-th location of the fluid interface $\mathbf{x}_s^m$ is then defined as

$$\mathbf{x}_s^m = \mathbf{x}_B^m + h^m \mathbf{e}^m. \tag{2.13}$$

The set of the changing distances on all the spines form the vector distance

$$\mathbf{h}(t) = [h^1(t), h^2(t), \dots]. \tag{2.14}$$

In order to accommodate the irregular configuration of the free surface, both the base points $\mathbf{x}_B^m(t)$ and directions $\mathbf{e}^m(t)$ can be chosen arbitrarily and can change with time, as long as the free boundary representation does not become singular (Saito and Scriven, 1981). In the simulations of drop coalescence in this chapter the base points $\mathbf{x}_B^m$ were fixed and located along the axis of symmetry $r = 0$. In addition, the spines are allowed to move only in the radial direction, that is $\mathbf{e}^m = \mathbf{e}_r$. Therefore, the location of the phase interface is only a function of the vector distance $\mathbf{h}$, which is calculated simultaneously with the velocity, pressure and surfactant concentration fields in the deforming flow domain.

The flow domain enclosed by the free surface is then discretized into quadrilateral finite elements (Reddy, 2004), so that the vertices of the elements (nodes) are aligned along the spines as sketched in Figure 2.2. The interfacial nodes $\mathbf{x}_s^m$ change location following the material motion of the free interface as it deforms with the flow field as discussed above (Lagrangian motion). But the internal nodes $\mathbf{x}_j$ are arbitrarily restricted to move along the spines following the deformation of the interface to ensure a smooth distortion of the elements (Eulerian motion). Therefore, the coordinates of all the internal nodes $\mathbf{x}_j = (z_j, r_j)$ depend on the location of the corresponding interfacial node, and, through Equation (2.13), on the vector distance $\mathbf{h}(t)$. That is,

$$z_j = z_j(\mathbf{h}),\ r_j = r_j(\mathbf{h}). \tag{2.15}$$

To account for the arbitrary motion of the nodes originated by the deformation of the free phase interface, the material derivative in the momentum equation is redefined as

$$\frac{D}{Dt} = \frac{\partial}{\partial t} + (\mathbf{v} - \dot{\mathbf{x}}) \cdot \nabla \mathbf{v}, \tag{2.16}$$

where $\dot{\mathbf{x}}$ is the Eulerian velocity of the individual grid nodes.

Following the conventional approach in computational fluid dynamics, mixed finite-element interpolation was used to expand the velocity and pressure fields (Reddy, 2004). Therefore, while the velocity field $\mathbf{v}(\mathbf{x}, t)$ was interpolated using nine-node bi-

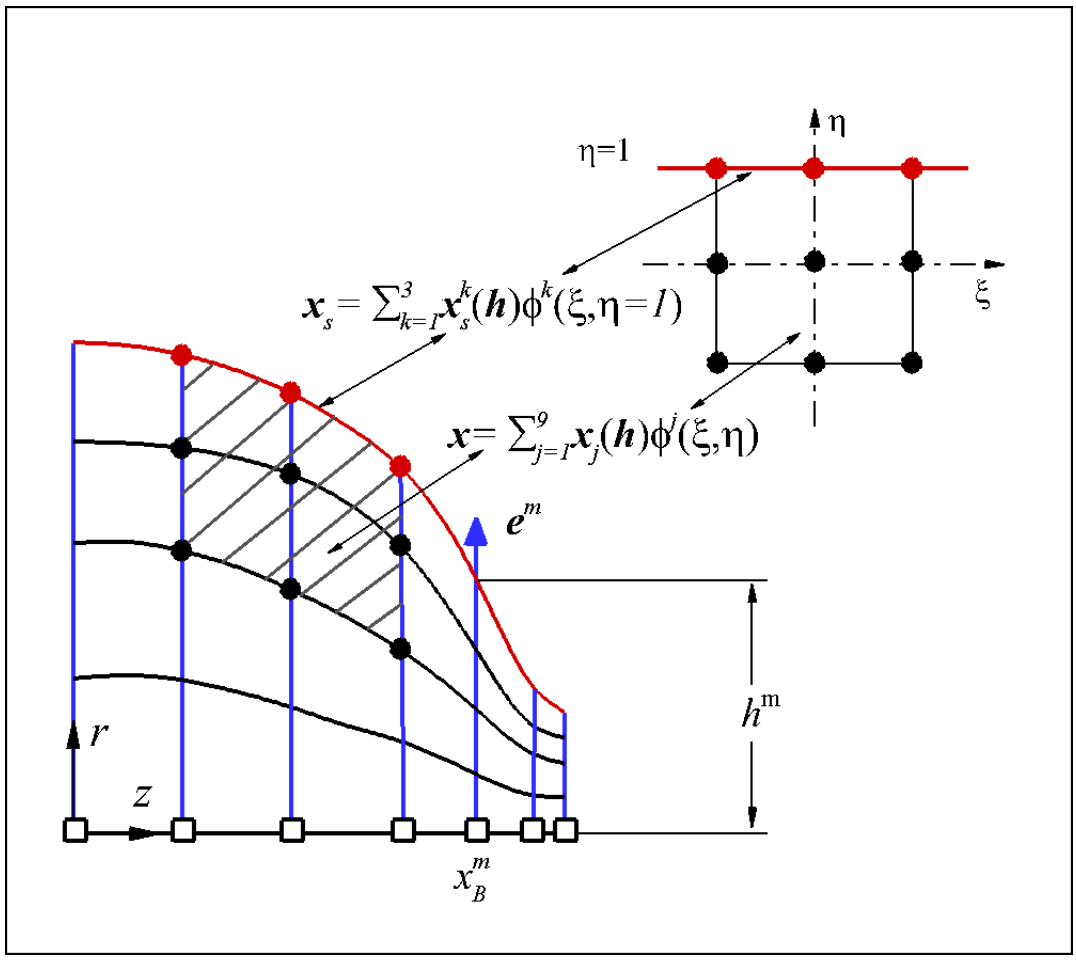


Figure 2.2. **Parametrization of the free interface using the method of spines.** The location of the deforming interface (red line) is parametrized at each time step by a distance $h^m$ measured along arbitrary spines (blue lines) defined by a base point $\mathbf{x}_B^m$ and a direction $\mathbf{e}^m$.

quadratic finite-element basis functions $\phi^j$, the pressure field $p(\mathbf{x}, t)$ was interpolated using four-node bi-linear finite-element basis functions $\psi^i$. That is,

$$\mathbf{v}(\mathbf{x}, t) = \sum_{j=1}^{9} \mathbf{v}_j(t)\phi^j(\xi, \eta), \tag{2.17}$$

$$p(\mathbf{x}, t) = \sum_{i=1}^{4} p_i(t)\psi^i(\xi, \eta). \tag{2.18}$$

The deforming finite-elements in the physical domain are mapped isoparametrically mapped in the computational domain defined by the coordinates $(\xi, \eta)$ on an non-deforming unit square, as shown in Figure 2.2 (Reddy, 2004).

Using Equation (2.15), the global coordinates $(z, r)$ are then expanded as

$$z(\xi, \eta, t) = \sum_{j=1}^{9} z_j(\mathbf{h}(t))\phi^j(\xi, \eta), \tag{2.19}$$

$$r(\xi, \eta, t) = \sum_{j=1}^{9} r_j(\mathbf{h}(t))\phi^j(\xi, \eta). \tag{2.20}$$

Similarly, using Equations (2.13) and (2.15), the location of the interface $\mathbf{x}_s$ is expanded as

$$\mathbf{x_s}(\mathbf{h}(t)) = \sum_{k=1}^{3} h^k(t)\hat{\phi}^k(\xi). \tag{2.21}$$

Here, the basis functions $\hat{\phi}^k$ are one-dimensional quadratic functions. These one-dimensional functions result from collapsing the two-dimensional bi-quadratic basis functions $\phi^j(\xi, \eta)$ onto the line $\eta = 1$ which corresponds to the free interface in the computational domain. That is,

$$\hat{\phi}^k(\xi) = \phi^j(\xi, \eta = 1), \tag{2.22}$$

as sketched in Figure 2.2 (red line).

The Galerkin/finite-element weighted residual of the continuity $R_c$ and momentum equations $\mathbf{R}_m$ were formulated by first multiplying Equation (2.1) and Equation (2.2)

by the bi-linear $\psi^i$ and bi-quadratic $\phi^j$ basis functions used to expand the pressure and velocity respectively, and then integrating in the domain $V(t)$:

$$R_c^i = \int_{V(t)} \psi^i (\nabla \cdot \mathbf{v}) \, dV = 0, \tag{2.23}$$

$$\mathbf{R}_m^j = \int_{V(t)} \phi^j \{ Re \left[ \frac{\partial \mathbf{v}}{\partial t} + (\mathbf{v} - \dot{\mathbf{x}}) \cdot \nabla \mathbf{v} \right] - \nabla \cdot \mathbf{T} \} \, dV = 0. \tag{2.24}$$

In order to apply the traction boundary condition Equation (2.8) accounting for the capillary and the Marangoni stresses, the term ($\phi^j \ \nabla \cdot \mathbf{T}$) in the weighted residual Equation (2.24) was reformulated by applying the divergence theorem as

$$\mathbf{R}_m^j = \int_{V(t)} \phi^j \{ Re \left[ \frac{\partial \mathbf{v}}{\partial t} + (\mathbf{v} - \dot{\mathbf{x}}) \cdot \nabla \mathbf{v} \right] + \nabla \phi^j \cdot \mathbf{T} \} \, dV - \int_{A(t)} \phi^j \left[ 2\mathcal{H} \sigma \mathbf{n} + \nabla_s \sigma \right] \, dA = 0, \tag{2.25}$$

The curvature $\mathcal{H}$ on the capillary term was calculated as

$$2\mathcal{H} = -\nabla_s \cdot \mathbf{n} = (\kappa_1 + \kappa_2), \tag{2.26}$$

where $\mathbf{n}$ is the unit vector normal to the interface.

The surface gradient operator $\nabla_s = (\mathbf{I} - \mathbf{nn}) \cdot \nabla$ can be expressed in terms of the arc length $s$ of the interface as:

$$\nabla_s ( \ ) = \frac{d( \ )}{ds} \mathbf{t}, \tag{2.27}$$

where $\mathbf{t}$ is the unit vector tangential to the interface. Therefore the axial curvature $\kappa_1$ and the azimuthal curvature $\kappa_2$ in Equation (2.26) were calculated as

$$\kappa_1 = \frac{d\mathbf{t}}{ds} \cdot \mathbf{n} \tag{2.28}$$

and

$$\kappa_2 = -\frac{(\mathbf{n}\cdot\mathbf{e}_r)}{r_s}, \tag{2.29}$$

where $r_s$ is the radial coordinate of the interface (Kistler and Scriven, 1983).

The unit tangent and normal vectors to a free surface were calculated using the computationally convenient form (Kistler and Scriven, 1983):

$$\mathbf{t} = \left.\frac{r_\xi \mathbf{e}_r + z_\xi \mathbf{e}_z}{\sqrt{r_\xi^2 + z_\xi^2}}\right|_{\eta=1}, \tag{2.30}$$

$$\mathbf{n} = \left.\frac{-z_\xi \mathbf{e}_r + r_\xi \mathbf{e}_z}{\sqrt{r_\xi^2 + z_\xi^2}}\right|_{\eta=1}, \tag{2.31}$$

where $z_\xi$ and $r_\xi$ are obtained directly from Equations (2.19) and (2.20)

$$z_\xi\Big|_{\eta=1} = \sum_{j=1}^{9} z_j(\mathbf{h}(t)) \left.\frac{\partial \phi^j(\xi,\eta)}{\partial \xi}\right|_{\eta=1}, \tag{2.32}$$

$$r_\xi\Big|_{\eta=1} = \sum_{j=1}^{9} r_j(\mathbf{h}(t)) \left.\frac{\partial \phi^j(\xi,\eta)}{\partial \xi}\right|_{\eta=1}. \tag{2.33}$$

The weighted residual $R_k^k$ of the kinematic equation was formulated by first multiplying Equation (2.5) by the quadratic basis functions $\hat{\phi^k}$ used to expand the location of the interface in Equation (2.21), and then integrating on the interface $A(t)$,

$$R_k^k = \int_{A(t)} \hat{\phi^k}\,[(\mathbf{v} - \dot{\mathbf{x}}_s)\cdot\mathbf{n}]\,dA = 0. \tag{2.34}$$

Similarly, the Galerkin weighted residual $R_s^k$ of the convection-diffusion equation is obtained by multiplying Equation (2.9) by the quadratic functions $\hat{\phi^k}$, and then integrating the product on the interfacial area $A(t)$ of the drops,

$$R_s^k = \int_{A(t)} \hat{\phi}^k \Bigg[ \frac{\partial \gamma}{\partial t} - \dot{\mathbf{x}}_s\cdot\nabla_s\gamma + \gamma(\mathbf{v}_s\cdot\mathbf{n})(\nabla_s\cdot\mathbf{n}) + \nabla_s\cdot(\gamma\mathbf{v}_s\cdot\mathbf{t})\mathbf{t} - \frac{1}{Pe}\nabla_s^2\gamma \Bigg]\,dA = 0. \tag{2.35}$$

In order to apply appropriate boundary conditions for the transport of surfactant, the weighted residual of the convection-diffusion equation (Eq. 2.35) was first rearranged as:

$$R_s^k = \int_{A(t)} \left\{ \hat{\phi}^k \Big[ \frac{\partial \gamma}{\partial t} - \dot{\mathbf{x}}_s \cdot \nabla_s \gamma \Big] + \hat{\phi}^k \gamma (\mathbf{v}_s \cdot \mathbf{n})(\nabla_s \cdot \mathbf{n}) \right.$$
$$\left. - \nabla_s \hat{\phi}^k \cdot (\gamma \mathbf{v}_s \cdot \mathbf{t})\mathbf{t} + \frac{1}{Pe}(\nabla_s \hat{\phi}^k \cdot \nabla_s \gamma) \right\} dA$$
$$+ \int_{A(t)} \nabla_s \cdot \Big[ \hat{\phi}^k (\gamma \mathbf{v}_s \cdot \mathbf{t})\mathbf{t} - \frac{1}{Pe} \hat{\phi}^k \nabla_s \gamma \Big] \, dA = 0. \quad (2.36)$$

Then, the divergence theorem was applied to the last integral term of Equation (2.36) yielding,

$$R_s^k = \int_{A(t)} \left\{ \hat{\phi}^k [\frac{\partial \gamma}{\partial t} - \dot{\mathbf{x}}_s \cdot \nabla_s \gamma] + \hat{\phi}^k \gamma (\mathbf{v}_s \cdot \mathbf{n})(\nabla_s \cdot \mathbf{n}) \right.$$
$$\left. - \nabla_s \hat{\phi}^k \cdot (\gamma \mathbf{v}_s \cdot \mathbf{t})\mathbf{t} + \frac{1}{Pe}(\nabla_s \hat{\phi}^k \cdot \nabla_s \gamma) \right\} dA$$
$$+ \left\{ \left[ \hat{\phi}^k \gamma (\mathbf{v}_s \cdot \mathbf{t}) - \frac{1}{Pe} \hat{\phi}^k (\nabla_s \gamma \cdot \mathbf{t}) \right] r_s \right\} \Bigg|_{S=0}^{S=S_F} = 0 \quad (2.37)$$

where $S = 0$ and $S = S_F$ represent the arc length of the points located at the interface at $z = -1$ and $z = 0$, respectively.

After the application of the divergence theorem, the two boundary conditions on the supporting solid surface ($S = 0$) and on the symmetry contact line between the drops ($S = S_F$) can both be applied in a natural way. First, the condition of null transport of surfactant at the solid surface and at the symmetry contact line require that

$$\nabla_s \gamma = \frac{d\gamma}{ds} \mathbf{t} = 0, \; at \; S = 0, \; S = S_F. \quad (2.38)$$

Second, the non-slip and the symmetry boundary conditions at the solid surface and at the symmetry contact line require that

$$\mathbf{v}_s \cdot \mathbf{t} = 0, \ at \ S = 0, \ S = S_F. \tag{2.39}$$

Therefore, the boundary conditions Equations (2.38) and (2.39) can both be imposed in a natural way by simply eliminating the last term in Equation (2.37).

The finite element formulation reduces the governing Equations (2.1), (2.2), (2.5), and (2.9) to a system of nonlinear ordinary differential equations with respect to time. A second-order trapezoidal finite difference method was used to discretize the time derivative with an Adam-Bashforth predictor as proposed by Gresho et al. (1980). Initial transients were smoothed using a backward difference method with constant time step during the first four time steps, as proposed by Kheshgi and Scriven (1983). After the initial smoothing, the time steps were chosen adaptively by using the continuation method proposed by Corvalan and Saita (1991).

The resulting nonlinear system of equations was then solved using full Newton's method. The advantage of using a full Newton iteration is that the convergence rate is quadratic due to the asymptotic behavior of the Newton's method. However, such a benefit requires careful derivation of the elements of the analytical Jacobian matrix with respect to the location of the free interface.

## 2.4 Results and Discussion

### 2.4.1 The Fluid Dynamics of Coalescence

When two liquid drops make contact, the narrow liquid neck that connects the drops widens driven by the strong capillary force acting on the meniscus formed around the neck. Figures 2.3 and 2.4 illustrate key features of this dynamics for drops with clean interface.

Figure 2.3 shows predictions of the capillary pressure and stream paths at an early stage in the coalescence of two viscous drops ($Re = 10$). Due to the large axial curvature of the interface in the vicinity of the contact point, the capillary pressure

on the meniscus is comparatively low (red in the figure) and, as a consequence, the liquid is rapidly drawn into the liquid neck.

Figure 2.4 shows predictions of the velocity field and the interfacial shape at three different times during the coalescence process. A key feature of the coalescence dynamics observed in the figure is that because the meniscus joining the drops is highly curved the flow rearranges drastically over very short distances (inset).

Comparing the numerical simulations against high-speed visualization data in Figures 2.5 and 2.6 shows that the simulations closely follow the dynamics of coalescence. In Figure 2.5, results from high-speed visualization experiments made by Yao et al. (2005) for the time evolution of the radius of the neck found between the drops were used as a benchmark. The experiments were carried out using viscous silicone-oil drops with viscosities $10^3$ cS (squares) and $10^5$ cS (circles). As shown in the figure the computational results obtained with the algorithm developed in section 2.3 (red line) show very good agreement with the experimental data (symbols).

Figure 2.6 compares numerical simulations against a tiny meniscus profile observed by Thoroddsen et al. (2005) using high-speed visualization experiments. The experiments were carried out using silicone drops with a viscosity of 0.22 Pa.s. As in Figure 2.5, the agreement between the experiments (diamonds) and the simulations (red line) in Figure 2.6 is excellent. The figure compares three simulations (solid lines in the figure) with different number of meshes. The degree of freedom ranges from $8,000$ to $10,000$ with the minimum size of the mesh defined as $10^{-8}$, $5 \times 10^{-8}$ and $10^{-9}$. The simulations are overlapped and the set of mesh with the smallest minimum size $10^{-9}$ is used for rest of the simulations in this chapter.

Together, the experiments in Figures 2.5 and 2.6 provide observational evidence for the direct numerical simulations, and strengthen the confidence in the conclusion the simulations help reveal in the next section.

An additional test was developed to compare the numerical simulations against results from an analytical solution developed by Hopper (1984). The analytical solution corresponds to the coalescence of two-dimensional (cylindrical) drops in the

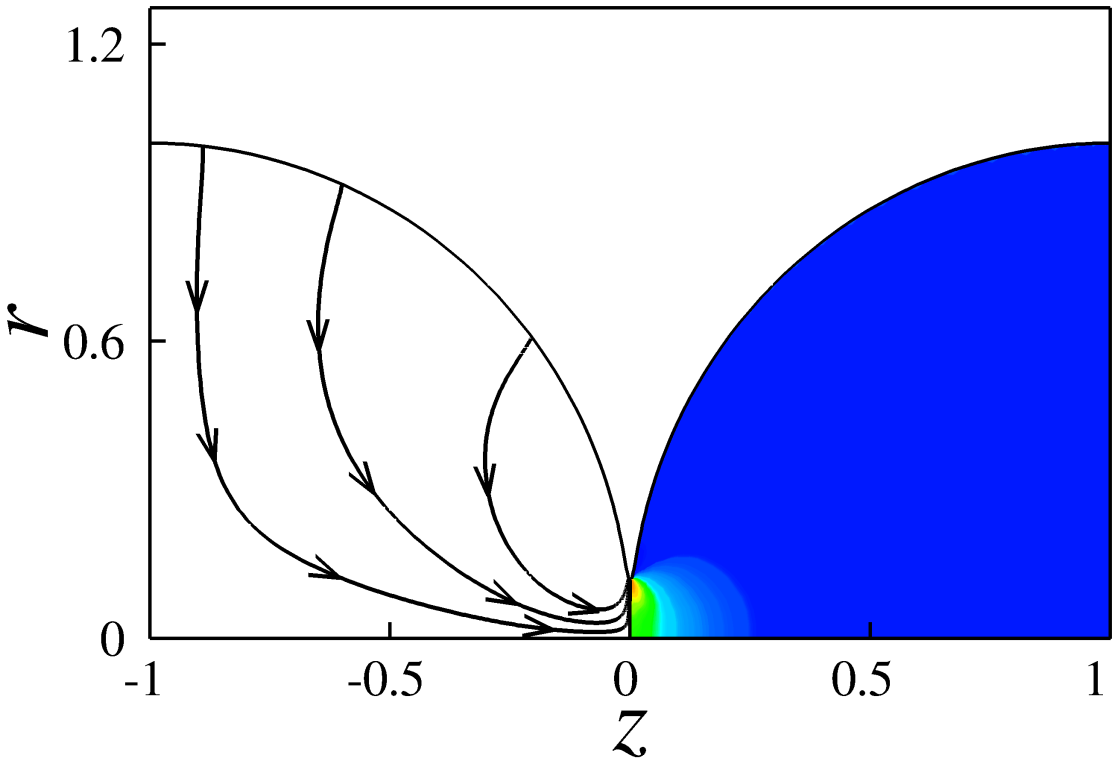


Figure 2.3. **Flow and pressure field at the onset of coalescence.** The fluid is driven into the liquid bridge (left drop) by the gradient of capillary pressure in the highly curved meniscus joining the drops (right drop). Here, the Reynolds number is $Re = 10$, and the dimensionless viscous time is $t = 0.045$.

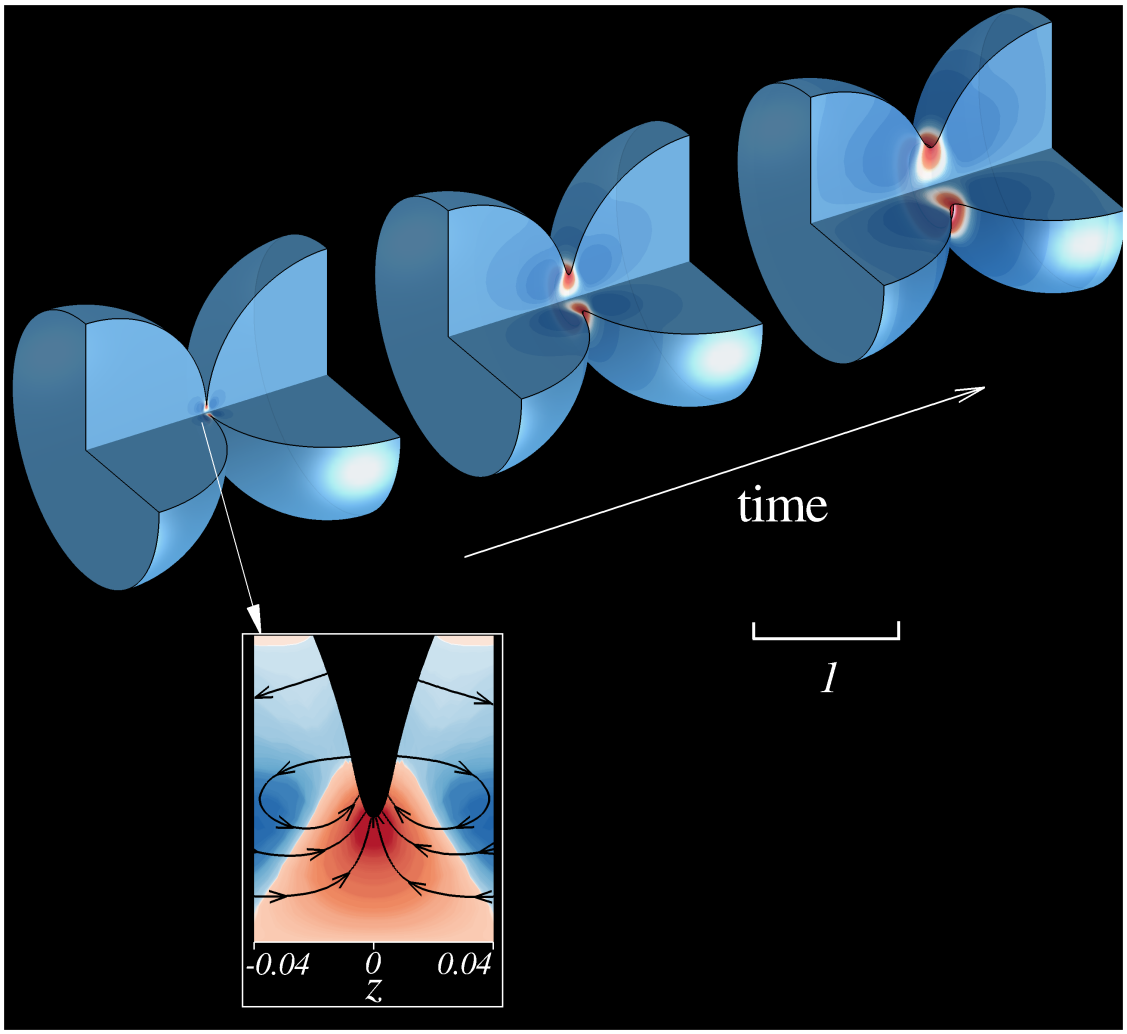


Figure 2.4. **Evolution of drop coalescence.** Shape and cross-sectional radial velocity during the coalescence of two viscous drops. The Reynolds number is $Re = 10$, and the dimensionless viscous times are $t = 0.035$, 0.160 and 0.230. Here dark red represents large radial velocity.

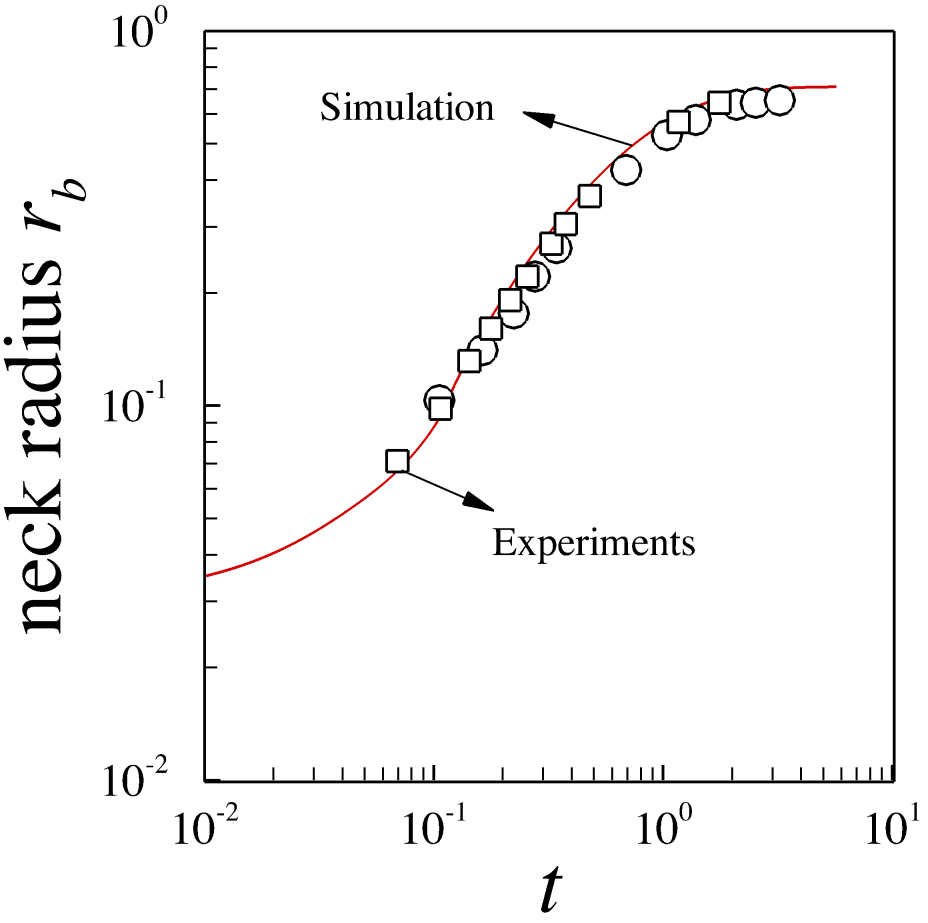


Figure 2.5. **Coalesce of viscous drops.** Experimental data by Yao et al. (2005) show the time evolution of the minimum neck radius $r_b$ during the coalescence of highly viscous silicone-oil drops with Reynolds numbers $Re = 0.0044$ (circles) and $Re = 0.44$ (squares). Simulation data corresponds to the Stokes regime (red solid line). The initial bridge radius cannot be determined from the experiments, so it was chosen to match the experimental data.

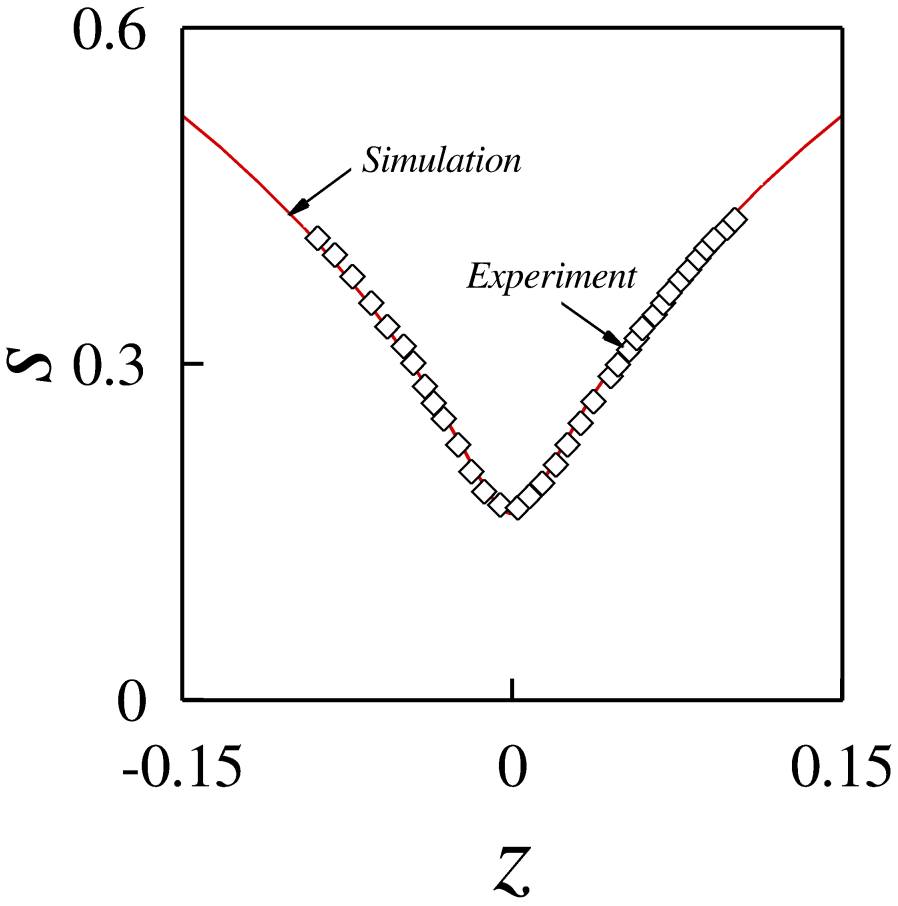


Figure 2.6. **Meniscus profile between two glycerin drops.** Meniscus profile from simulations (red solid line) shows excellent agreement with high-speed photography data by Thoroddsen et al. (2005) for the coalescence of two viscous glycerin drops (diamonds). The viscosity of the drops is $\mu = 0.22$ Pa.s. Simulations with three different mesh sizes are tested and the results are overlapped. The degree of freedom ranges from $8,000$ to $10,000$ with the minimum size of the mesh defined as $10^{-8}$, $5 \times 10^{-8}$ and $10^{-9}$.

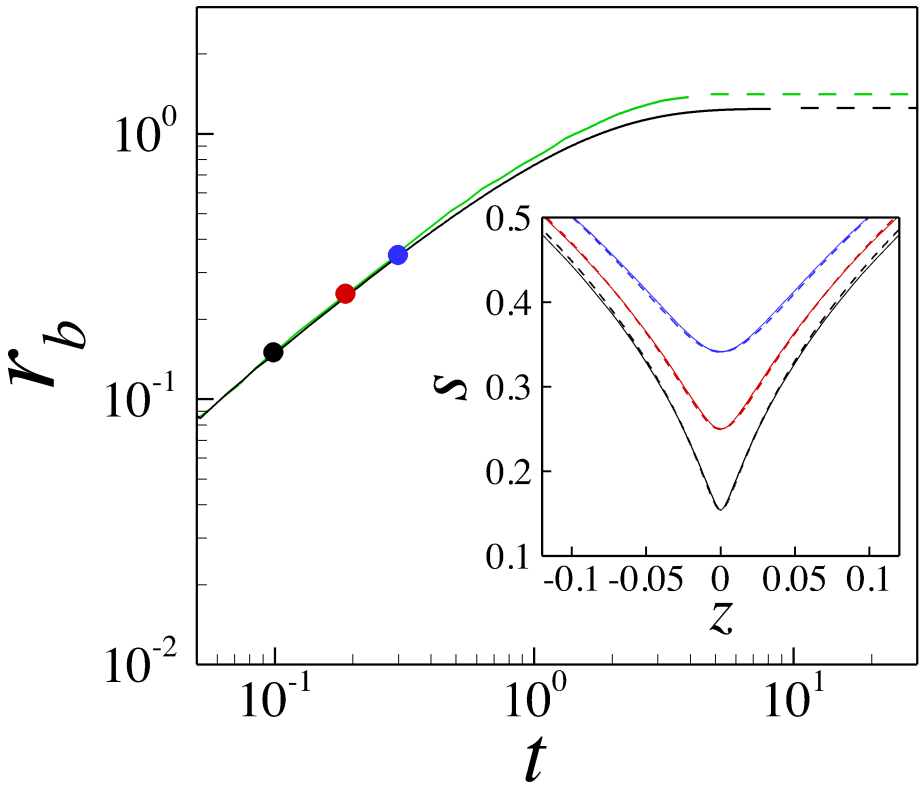


Figure 2.7. **Drop coalescence in the Stokes limit.** Time evolution of the minimum neck radius $r_b$ during the coalescence of two-dimensional (cylindrical) drops obtained analytically by Hopper (1984) (green solid line) and three-dimensional drops from the simulations (black solid line) in the Stokes limit. The theory and the simulations show excellent agreement up to neck radius $r_b \approx 0.5$. Three meniscus profiles at bridge radius $r_b = 0.15$ (black), $r_b = 0.25$ (red), and $r_b = 0.35$ (blue) from the simulation (solid lines) also show excellent agreement with the analytical interfacial shapes (dashed lines)

Stokes limit ($Re = 0$). Although clearly different at later times, the evolution of the meniscus during the coalescence of two-dimensional cylindrical drops is expected to agree with that of three-dimensional spherical drops at early times, as demonstrated by Eggers et al. (1999). Figure 2.7 shows an excellent agreement between the simulations (black line) and the two-dimensional analytical solution (green line) up to a neck radius $r_b \approx 0.5$, or about one half of the initial drop radius. For additional comparison, the figure also shows the theoretical equilibrium radius $2^{1/2}$ for cylindrical drops (green dashed line) and the equilibrium radius $2^{1/3}$ for spherical drops (black dashed line).

### 2.4.2 Rate of Coalescence of Surfactant-laden Drops

To gain initial insight into the mechanisms behind the coalescence of surfactant-laden drops, this section compares the rate of coalescence of pairs of drops with ($Ma = 0.6$) and without ($Ma = 0$) surfactant, starting from quiescent identical viscous drops ($Re = 10$) connected by a thin liquid bridge.

Both the bridge between the drops with clean interface and the bridge between the surfactant-laden drops widen under the outward pull of surface tension at the joining meniscus, as shown in Figure 2.8.

For the drops with clean interface (Fig. 2.8, red line), the bridge radius $r_b(t) = S(z = 0, t)$ exhibits a rapid initial growth, which then slows in a manner similar to what is observed in experiments. (See, for example, the experiments by Yao et al. (2005) shown in Fig. 2.5).

For the drops with surfactant (Fig. 2.8, blue line), the liquid bridge grows significantly more slowly, despite the fact that both computations in Figure 2.8 begin with identical dimensionless surface tension $\sigma = 1$. That is, the drops with clean interface and the drops with surfactant both have the same initial dimensional surface tension $\sigma_0$.

Meniscus profiles in Figure 2.9 further illustrate the significance of the lower coalescence rate in the surfactant-laden drops. Whereas the liquid bridge between the drops with surfactant doubles in size at a viscous dimensionless time $t = 0.11$ after the onset of coalescence (Fig. 2.9, blue line), the bridge between the drops with clean interface reaches almost a three-fold increase during the same time span (Fig. 2.9, red line).

Figure 2.10 illustrates the bulk and interfacial velocity corresponding to the drops in Figure 2.9 . The figure shows that at the same neck radius ($r_b \approx 0.15$), the bulk fluid in the vicinity of the meniscus flows at higher radial velocity (red in the figure) in the drops with clean interface. At the interface, the velocity for the drops with clean interface almost double that of the drops with surfactant.

### 2.4.3 Effect of the Uneven Contraction of the Drop Interface

This section seeks to uncover what causes the lower rate of coalescence in surfactant-laden drops, such as those illustrated in Figure 2.8. It is important to reiterate here that both coalescence processes illustrated in Figure 2.8 start with drops with identical initial surface tension $\sigma_0$. In addition, the convective capillary flow drags the insoluble surfactant away from the meniscus. Therefore, it is unclear what causes the lower rate of coalescence in the surfactant-laden case. As there are several forces at play at the tiny scale of the joining meniscus, the precise mechanism of coalescence of surfactant-laden drops has been, so far, elusive.

Results from the simulations demonstrate that the cause of the slower rate of coalescence in the surfactant-laden case is that the fast contraction of the meniscus surface area that occurs in the early stages locally increases the concentration of surfactant. Indeed, due to large differences in local interfacial curvature, and consequently in local interfacial velocity, the surface of coalescing drops contracts at different rates, and this contraction is most severe on the meniscus bridge. Accordingly, the predicted concentration field shows an important and highly localized accumula-

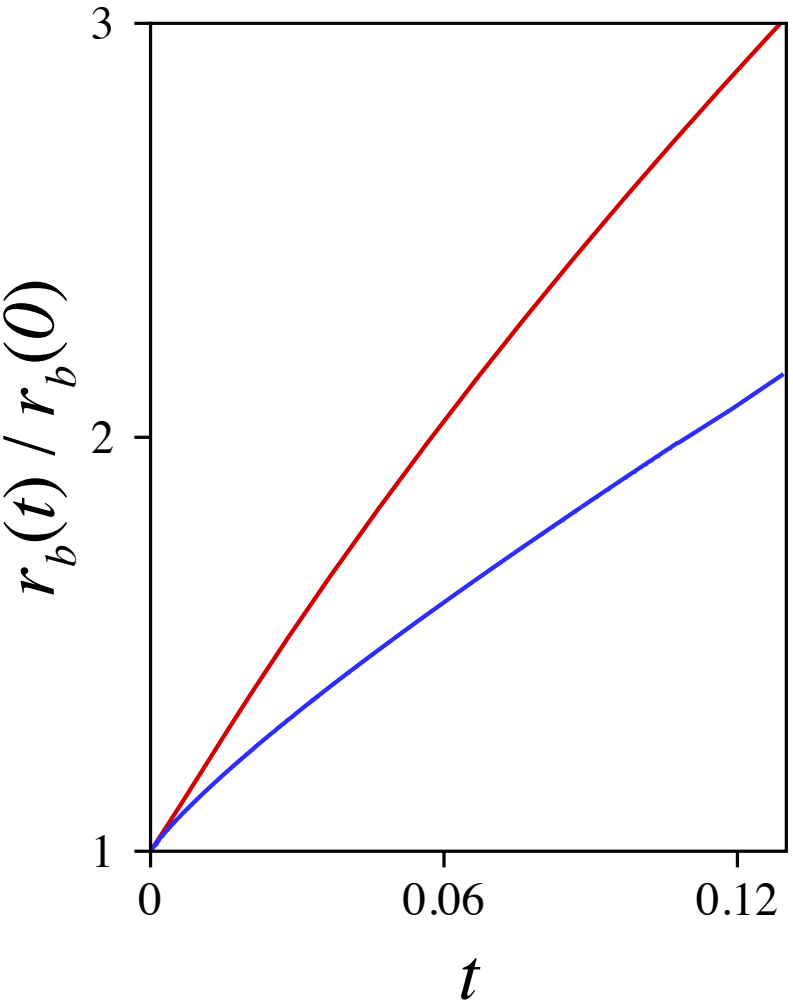


Figure 2.8. **Normalized bridge radius.** Time evolution of the minimum radius of the liquid bridge $r_b(t)$ connecting two drops with clean interface (red line) and two drops with surfactant (blue line) normalized with respect to the initial bridge radius $r_b(0)$. Here, the initial bridge radius is $r_b(0) = 0.07$, and the Marangoni number is $Ma = 0.6$ for the drops with surfactant.

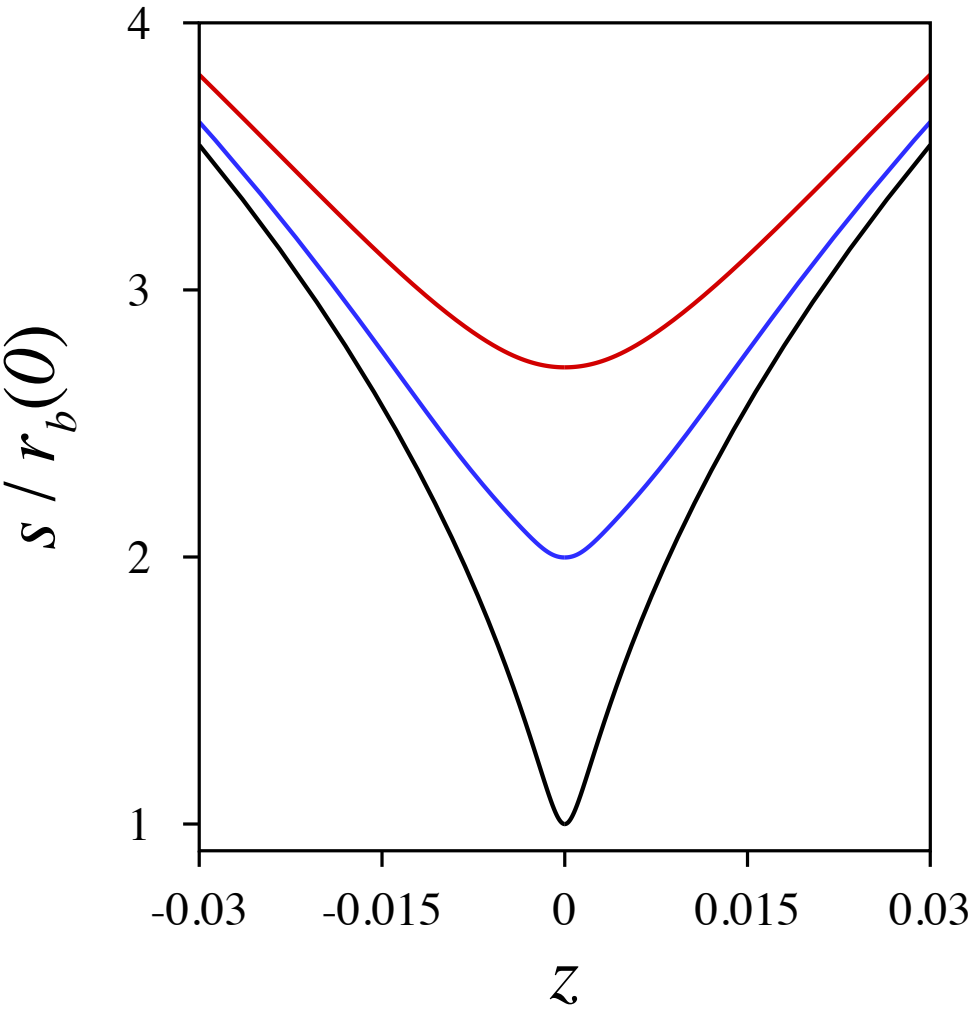


Figure 2.9. **Normalized interfacial shape.** Profiles $S(z,t)$ of the meniscus bridge formed between drops with clean interface (red line) and drops with surfactant (blue line) at times $t = 0.11$ and time $t = 0$ (black line). Here, the initial bridge radius is $r_b(0) = 0.07$, and the Marangoni number is $Ma = 0.6$ for the drops with surfactant.

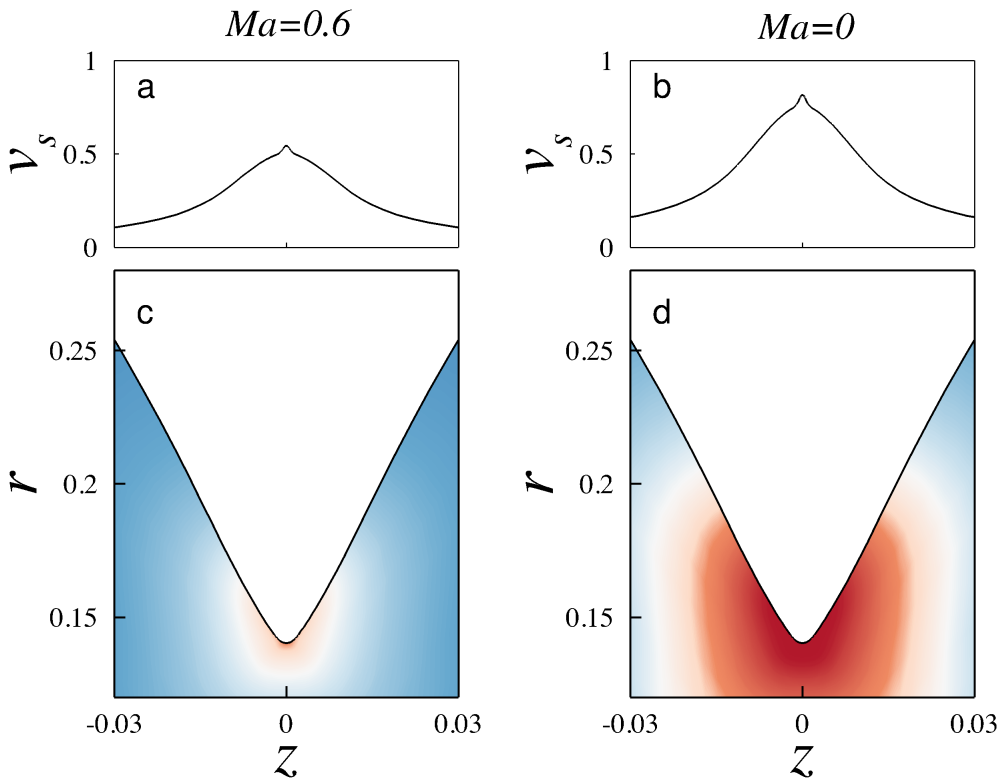


Figure 2.10. **Bulk and interfacial radial velocity in the meniscus bridge.** Bulk and interfacial radial velocities $v_s$ around the meniscus bridges corresponding to Figure 2.9 between drops with clean interface ($Ma = 0$, right panel) and drops with surfactant ($Ma = 0.6$, left panel) at neck radius $r_b = 0.147$. Here, red represents high radial velocity and blue represents low radial velocity.

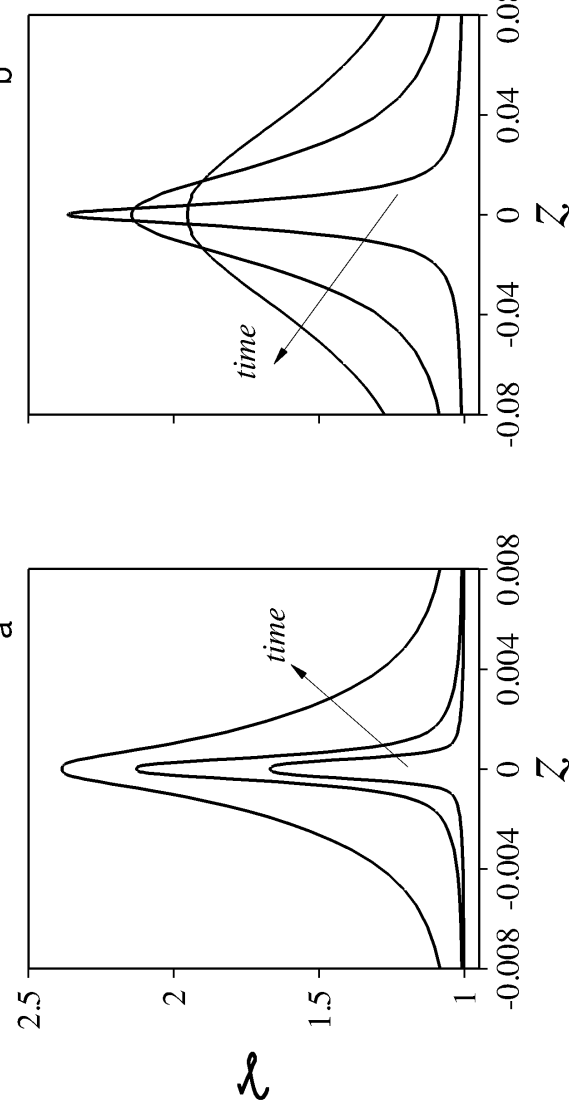


Figure 2.11. **Profiles of interfacial surfactant concentration on the joining meniscus.** Concentration profiles $\gamma(z,t)$ in units of initial surfactant concentration $\gamma_0$ for **(a)** viscous times $t < 0.064$ at $t = 0.0018$, 0.0087 and 0.046, and **(b)** viscous times $t > 0.064$ at $t = 0.12$, 0.33 and 0.54. Here, the Marangoni number is $Ma = 0.6$.

tion of surfactant on the meniscus during the early stages of coalescence, as shown in Figure 2.11a. To gain a sense of scale, note that the domain of Figure 2.11a showing early profiles of interfacial concentration is about a hundredth of the drop diameter. This accumulation of surfactant directly affects the rate at which the drops coalesce by decreasing the pull of surface tension on the highly curved meniscus bridge.

Interestingly, the simulations also show that although the concentration of surfactant is dominated by the contraction of the meniscus at early times, at later times the surrounding flow limits the extent to which this concentration can grow. Indeed, during the initial period of surfactant accumulation the influence of the accelerating convective flow around the meniscus becomes increasingly important. This convective flow — and in much less extent, diffusion — drags the surfactant up the side of the drops decreasing the rate of surfactant accumulation. Accordingly, the simulations show that the concentration of surfactant on the meniscus reaches a maximum and then decreases as shown in Figure 2.11b. Note that, despite the decrease in surfactant concentration due to the convective flow, the surface tension on the meniscus remains low because the convective process does not deplete the previously accumulated surfactant below the initial (dimensionless) concentration $\gamma = 1$. As shown in Figure 2.12, the maximum concentration of surfactant at the meniscus occurs early in the process, at a viscous time $t \approx 0.064$ .

### 2.4.4 Effect of the Marangoni Stress

The convective flow responsible for surfactant transport in the vicinities of the meniscus is driven by capillarity, but also includes an important contribution induced by Marangoni stresses. Indeed, the rapid contraction of the tiny meniscus results not only in lower local surface tension but also leads to strong surface-tension gradients (cf. Fig. 2.11). These gradients, in turn, generate tangential Marangoni stresses $\mathbf{n} \cdot \mathbf{T} \cdot \mathbf{t} = \nabla_s \sigma$ that pull the interface from the regions of high surface tension to

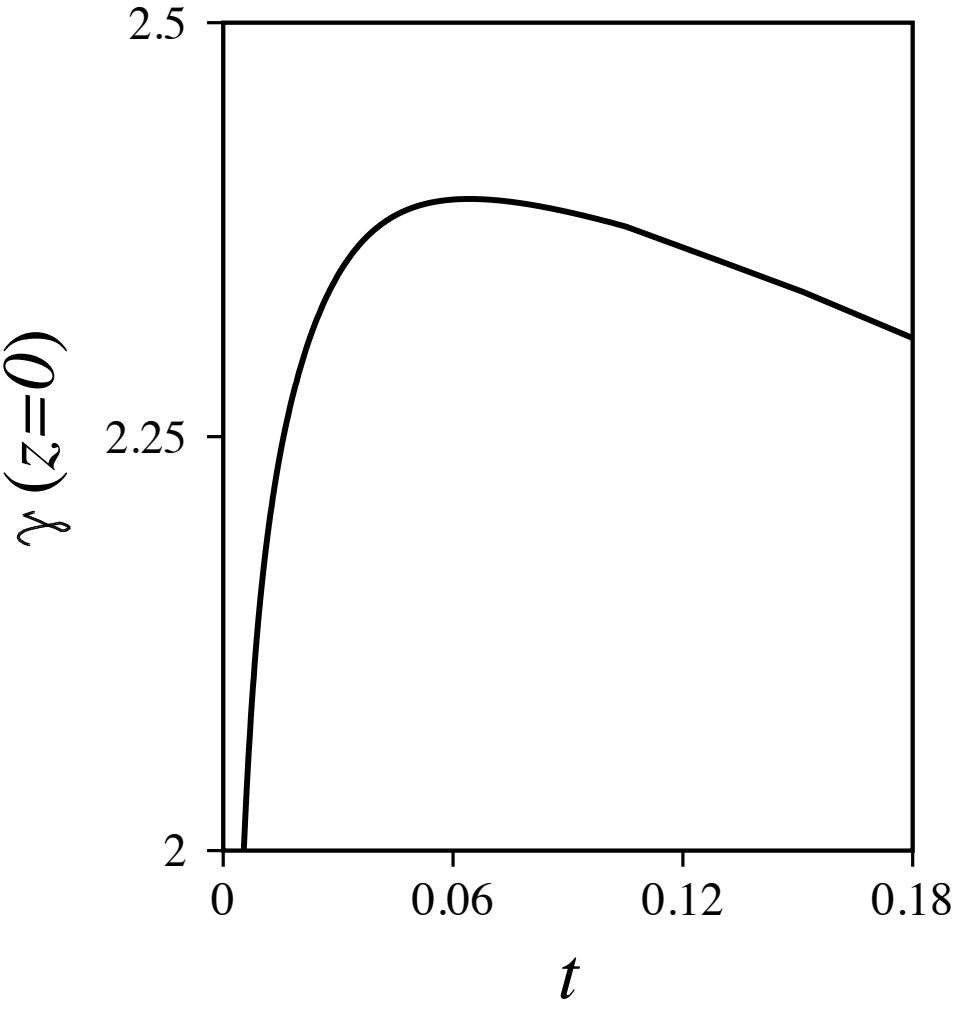


Figure 2.12. **Time evolution of the interfacial surfactant concentration on the joining meniscus.** The surfactant concentration on the joining meniscus bridge $\gamma(z = 0, t)$ increases to almost two times the initial concentration $\gamma_0$ at a viscous time $t \approx 0.064$. Here, the Marangoni number is $Ma = 0.6$.

regions of low surface tension, and enhance the flow up the side of the drops through momentum transfer.

Early velocity fields close to the meniscus illustrated in Figures 2.14 demonstrate the important contribution of the Marangoni stress to the interfacial tangential motion and the surrounding fluid. Note that the intrusion of the enhanced tangential velocity into the flow field creates recirculation patterns (Figs. 2.14b and c) that are not observed in the absence of surfactant (Fig. 2.14a) at the instance.

The resulting changes in the bulk flow may suggest new avenues for the design of improved mixing patterns in microfluidic applications (Lai et al., 2010), while the enhanced tangential interfacial flow could have important consequences on the phenomenon of partial drop coalescence (Blanchette and Bigioni, 2006, Blanchette et al., 2009). The significance of the Marangoni stress is further emphasized in Figure 2.13, which compares the tangential velocity $v_t \equiv \mathbf{v}_s \cdot \mathbf{t}$ along the interface of the drop for the three cases depicted in Figures 2.14. From this new perspective, it becomes clear that the portion of the interface where the liquid moves away from the meniscus ($v_t < 0$) can reach values more than six times larger on the surfactant-laden drops than on the drops with clean interface (Fig. 2.13).

## 2.5 Conclusion

Results from this numerical study uncover the main physical mechanisms involved in the coalescence of drops with surfactant after the drops make contact. Simulations show that when two liquid drops coalesce their surface area decreases unevenly. The surface contraction is most severe right on the meniscus bridge between the drops and becomes much less noticeable toward the side of the drops. As a result surfactants accumulate on the joining meniscus. Interestingly, this process is hampered by Marangoni flows driven by surface-tension gradients which, in turn, are induced by the uneven surfactant accumulation. These entwined mechanisms, uncovered for the first time in this study, directly affects the rate at which the drops coalesce by modu-

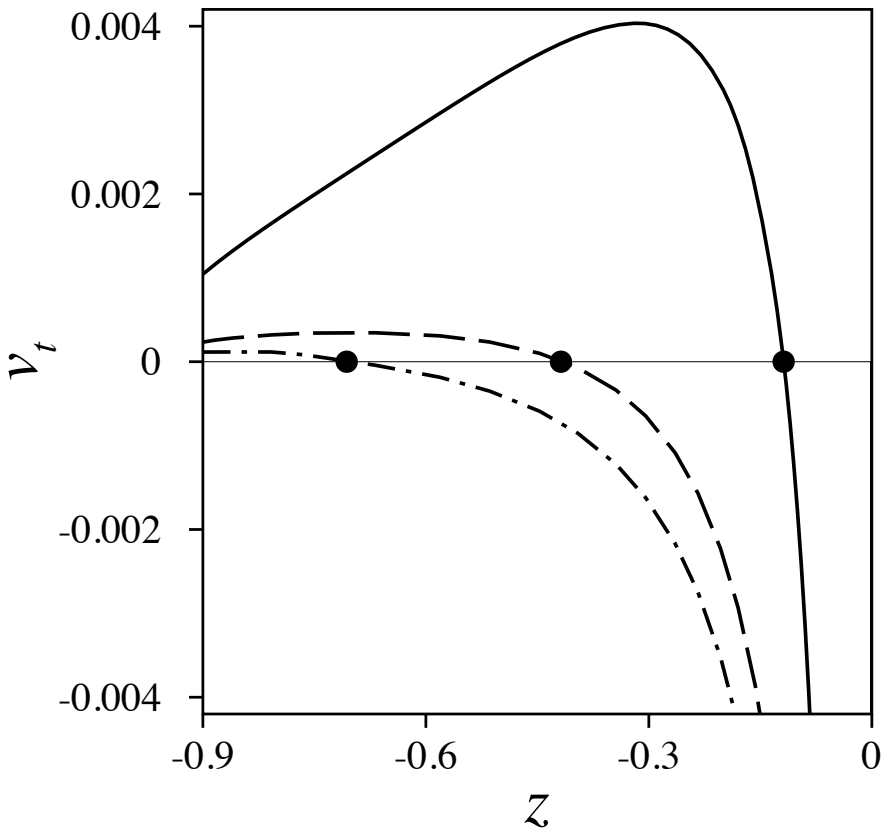


Figure 2.13. **Interfacial velocity profile.** Interfacial tangential velocity corresponding to the three cases depicted in Figure 2.14: $Ma = 0$ (solid line), $Ma = 0.6$ (dashed line) and $Ma = 1.2$ (dash dot line). Negative velocity indicates flow away from the meniscus and the solid circle indicates the location on the interface where the tangential velocity is zero.

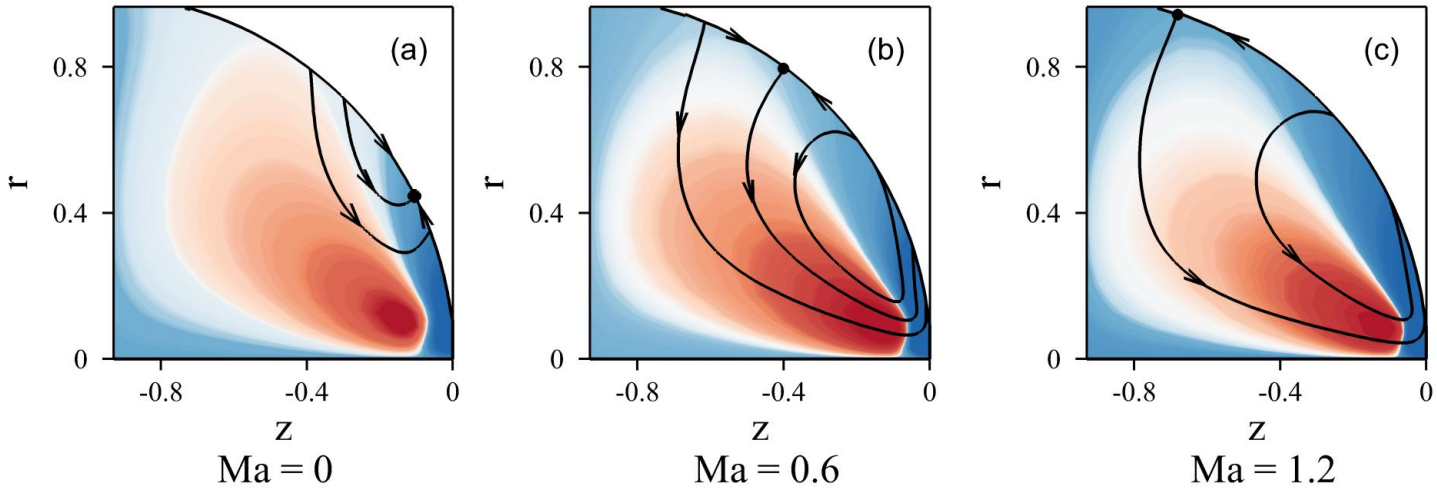


Figure 2.14. **Radial flow field as a function of surfactant strength.** Cross-sectional radial velocity field with blue indicating positive radial motion and red indicating negative radial motion. Computations were carried out with Marangoni numbers $Ma = 0$, 0.6 and 1.2.

lating the pull of surface tension on the widening meniscus bridge. It is expected that this new insight into the physical mechanisms of coalescence will enhance the understanding of two-phase systems involving small drops, such as spray, atomization, food emulsions, and microfuidic applications.

Although the numerical simulations in this study solve the full system of Navier-Stokes and surfactant-transport equations, the results are certainly limited by several simplifying assumptions in the model system. Future works should generalize these results to include soluble surfactants (Lobo and Svereika, 2003), higher Reynolds numbers (Eggers et al., 1999), and nonlinear surfactant equations of state (Milliken et al., 1993) (including potential micellar interactions on the meniscus (Craster et al., 2009)) to ensure a more complete understanding of the mechanisms of coalescence in the presence of surfactants.

# 3. IMPINGEMENT OF VISCOUS AND SHEAR-THINNING LIQUID JETS

## 3.1 Impingement of Viscous Liquid Jets

The impingement of low-viscosity liquid jets has been studied extensively for over a century due to its fundamental scientific interest and its practical importance in spray and atomization technologies. However, the role of the fluid viscosity on the impingement of viscous liquid jets is largely unknown despite the fact that viscous liquids are common in spray and atomization processes ranging from spray drying in the food industry to the atomization of gelled propellants in rocket engines.

This Section reports direct numerical simulations that enable a detailed analysis of the influence of viscosity on the impingement dynamics. The simulations solve the complete Navier-Stokes system governing the free-surface dynamics, and so fully account for the interplay of inertia, viscous and capillary forces. Results show that the liquid viscosity profoundly affects the impingement dynamics. The simulations demonstrate that the collision of moderately viscous jets generates a fluid sheet that thins at a rate $r^{-1}$ with the distance $r$ from the impact point, in contrast to the inertial case in which the sheet thins at a faster rate $r^{-2}$. As the viscosity increases further, the fluid sheets become thicker and more uniform, and contrary to the inertial case, the velocity of the sheets are lower than the velocity of the jets. Results further reveal that due to viscous stresses the impact pressure generated by the collision of viscous liquid jets scales as $Re^{-1}$, where $Re$ is the jet Reynolds number.

This section contains both text and figures from a published manuscript entitled "Influence of viscosity on the impingement of laminar liquid jets." (2014, Chemical Engineering Science, 119, 182–186), the article is a product of joint efforts between Dr. Carlos M. Corvalan and myself.

### 3.1.1 Introduction

The collision of two inviscid liquid jets facing one another has been extensively studied since the pioneering works of Savart (1833) and later Ranz (1959) and Taylor (1960) due to its fundamental fluid mechanics interest and its practical importance in spray and atomization processes. As a result of these studies, it is now known that inertial liquid sheets resulting from the collision of low-viscosity liquid jets expand radially at constant speed unopposed by viscosity (Ranz, 1959, Taylor, 1960). As the inertial sheets expand, the liquid at the edge of the sheets accumulates in a toroidal rim which eventually disintegrates into drops at a distance from the impact point which is known as the Taylor radius (Bush and Hasha, 2004, Clanet and Villermaux, 2002, Huang, 1970, Taylor, 1960). Understanding this free-surface flow is relevant to diverse spray technologies including spray drying, spray painting and crop spraying, and is central to the production of food emulsions, the atomization of fuel in combustion engines, and the atomization of propellants in rocket engines for space and defense technologies (Ashgriz, 2011, Bremond and Villermaux, 2006, Clanet and Villermaux, 2002, Lefebvre, 1988, Mahajan and Kirwan, 1996, Ryan et al., 1993, Sutton, 1992, Villermaux et al., 2013).

Although the bulk of the research has focused on the dynamics of inertial jets, understanding the influence of viscosity on the dynamics of jet impingement is critical, as viscous fluids are ubiquitous in spray and atomization processes. Examples of these fluids include inks, paints, food emulsions and polymeric solutions, and, more recently, gelled propellants for rocket and missile engines (Baek et al., 2011, Chen et al., 2012a,b, Howell et al., 2010, Kampen et al., 2007, Mallory and Sojka, 2014, Villermaux et al., 2013, Yang et al., 2012, 2014). These are typically highly viscous fluids, which may also exhibit non-Newtonian shear-thinning and elastic behaviour (James et al., 2009, Santos et al., 2010, Yang et al., 2013).

Recent studies using viscous glycerol solutions (Choo and Kang, 2001, Yang et al., 2014) and viscous alcohol-sugar solutions (Lai et al., 2005) have shown that the colli-

sion of viscous jets generates expanding sheets which are thicker than those generated from the collision of inviscid jets, with the consequent impact in sheet stability and drop size. However, how precisely viscous stresses influence the impingement dynamics, and how these dynamics determine the velocity and thickness of the expanding sheets remain poorly understood.

Here high-fidelity numerical simulation is used to gain insight into the influence of viscosity on the dynamics of jet impingement. Section 3.1.2 states the Navier-Stokes system governing the axisymmetric impingement of two facing laminar jets, and the direct numerical simulation procedure used to simultaneously solve the full Navier-Stokes system for velocity, pressure and location of the interface by Newton iteration. Section 3.1.4, discusses the results from the simulations. By varying the liquid viscosity over about six decades, results help identify the influence of viscous stresses in the dynamics of jet impingement at intermediate liquid viscosities, and contrast these novel findings against the inviscid and Stokes limits.

### 3.1.2 Problem Description and Governing Equations

The dynamics of jet impingement is analyzed here by following the evolution of the axisymmetric collision of two identical facing jets of an incompressible Newtonian liquid of constant density $\rho$, viscosity $\mu$, and surface tension $\sigma$. The configuration of the system is sketched in Figure 3.1.

The problem is described below in dimensionless form using the jet radius $a$ as the characteristic length scale, $a\mu/\sigma$ as the viscous timescale, and $\sigma/a$ as the stress and pressure scale.

The evolution of the liquid velocity $\mathbf{v}(\mathbf{x}, t)$ and pressure $p(\mathbf{x}, t)$ are calculated by solving the full, axisymmetric Navier-Stokes system:

$$\nabla \cdot \mathbf{v} = 0, \tag{3.1}$$

$$Re^2 \left( \frac{\partial \mathbf{v}}{\partial t} + \mathbf{v} \cdot \nabla \mathbf{v} \right) = \nabla \cdot \mathbf{T}, \tag{3.2}$$

where

$$\mathbf{T} \equiv \frac{1}{2}\, We\, (-p\mathbf{I} + \nabla \mathbf{v} + \nabla \mathbf{v}^T) \tag{3.3}$$

is the dimensionless Cauchy stress tensor.

The liquid viscosity enters in the Navier-Stokes system through the jet Reynolds number

$$Re \equiv \frac{\rho \hat{U} a}{\mu}, \tag{3.4}$$

which measures the importance of inertia relative to viscous forces. The velocity $\hat{U}$ is the dimensional jet velocity, the profiles of which are considered constant in all the simulations in this Chapter.

The effect of capillarity enters in the Navier-Stokes system through the balance of forces at the free interface (Slattery, 1990):

$$\mathbf{T} \cdot \mathbf{n} = We\, \mathcal{H}\mathbf{n}, \tag{3.5}$$

where

$$We \equiv \frac{2a\rho \hat{U}^2}{\sigma}, \tag{3.6}$$

is the Weber number based on the jet diameter $2a$, which represents the ratio of inertial forces to surface tension forces, and $\mathbf{n}$ is the unit vector normal to the interface.

The mean curvature of the interface $\mathcal{H}$ is calculated as

$$\mathcal{H} = -1/2\ \nabla_s \cdot \mathbf{n}, \tag{3.7}$$

where

$$\nabla_s = (\mathbf{I} - \mathbf{nn}) \cdot \nabla \tag{3.8}$$

is the surface gradient operator (Deen, 2011, p. 580; Slattery, 1990, p. 653). Simulations are carried out in the smooth region $We < 1000$ in which the adjoining gas

phase can be considered dynamically inert (Clanet and Villermaux, 2002, Huang, 1970).

The requirement that there is no liquid crossing the phase interface is guaranteed by imposing the kinematic condition

$$\mathbf{n} \cdot (\mathbf{v} - \mathbf{v}_s) = 0 \tag{3.9}$$

where $\mathbf{v}_s$ is the velocity of the points on the interface. At the plane and axis of symmetry the shear stress vanishes and the velocity normal to the boundaries are set to zero because of the non-flux condition.

### 3.1.3 Direct Numerical Simulation of Jet Impingement

In this Chapter the full Navier-Stokes system of equations (Eqs. 3.1 and 3.2) and the kinematic condition (Eq. 3.9) governing the free-surface dynamics of axisymmetric jet impingement are solved simultaneously for velocity, pressure and location of the moving interface using direct numerical simulation.

The direct numerical simulation scheme is analogous to the numerical algorithm already described in Section 2.3, and so is only briefly summarized here. In this algorithm the finite-element method along with the arbitrary Lagrangian-Eulerian method of spines (Kistler and Scriven, 1983) is used to discretize the governing partial differential equations in space. Then, the resulting ordinary differential equations are discretized in time using a second-order Adam-Bashforth predictor-corrector with a trapezoidal rule (Gresho et al., 1980) in which the time steps are adaptively chosen using a first order continuation method (Corvalan and Saita, 1991). To enhance convergence and numerical efficiency, the set of highly coupled, strongly non-linear algebraic equations resulting from the spatial and temporal discretization are simultaneously solved by Newton's method with full analytical Jacobian.

The arbitrary Lagrangian-Eulerian method of spines used in this chapter to parametrize the deforming free interface was also described in detail in Section 2.3. In the

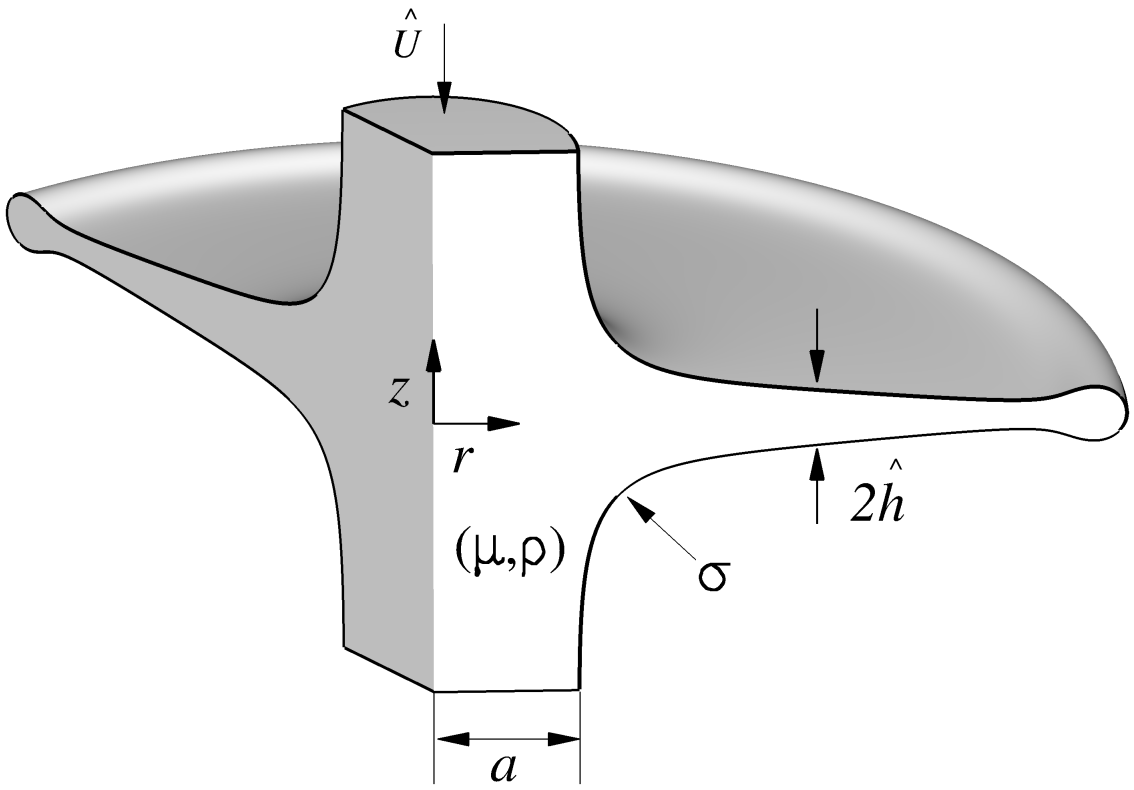


Figure 3.1. **Impingement of two laminar liquid jets.** Axisymmetric impingement of two facing liquid jets of radius $a$ and velocity $\hat{U}$. The density of the liquid is $\rho$, the viscosity $\mu$, and the surface tension $\sigma$. The thickness of the radially expanding liquid sheet is $2\hat{h}$. The sheet profile in this sketch corresponds to the case discussed in Figure 3.7b.

method of spines, the location $\mathbf{x}_s^m$ of a generic finite-element node $m$ on the interface is parametrized by a distance $h^m$ along a directed line (or spine) defined by a base point $\mathbf{x}_B^m$ and a unit direction vector $\mathbf{e}^m$; that is,

$$\mathbf{x}_s^m = \mathbf{x}_B^m + h^m \mathbf{e}^m. \tag{3.10}$$

However, the parametrization of the deforming interface in the problem of jet impingement is much more challenging than in the problem of drop coalescence discussed in Section 2.3 for two main reasons.

The first challenge is that during jet impingement the dominant direction of the flow changes from axially dominated in the colliding jets to radially dominated in the expanding liquid sheet (see Figure 3.1). To address this challenge, the base points $\mathbf{x}_B^m$ were located not only along the axis of symmetry in the jets, but also along the radial axis in the fluid sheet. Moreover, the spines were allowed to expand not only in the axial ($\mathbf{e}^m = \mathbf{e}_z$) and radial ($\mathbf{e}^m = \mathbf{e}_r$) directions but also in oblique directions given by $\mathbf{e}^m = \cos\theta^m \ \mathbf{e}_z + \sin\theta^m \ \mathbf{e}_r$, where the angle $\theta^m$ characterizes suitable directions chosen to better describe the deforming interface.

A second important challenge is that the radial liquid sheet expands from a tiny nascent sheet immediately after the impact to a fully developed sheet bounded by a toroidal rim in the long time limit (see Figure 3.7). To address this challenge, the base points $\mathbf{x}_B^m$ were allowed to change location at each time step along the radial axis, that is $\mathbf{x}_B^m = \mathbf{x}_B^m(t)$. The movement of the base point follows the material motion of the edge of the sheet as it expands with the flow field, thus avoiding large distortion of the finite element mesh (see Figure 3.2). Moreover, mesh independence studies were conducted in order to make sure that pressure, velocity and the sheet profile and its bounding toroidal rim were well defined as the sheet expands. From these studies, finite-element meshes with $8000 - 10000$ degrees of freedom were selected for the simulations depending on the jet Reynolds number $Re$ and the Weber number $We$ (see Fig. 3.3).

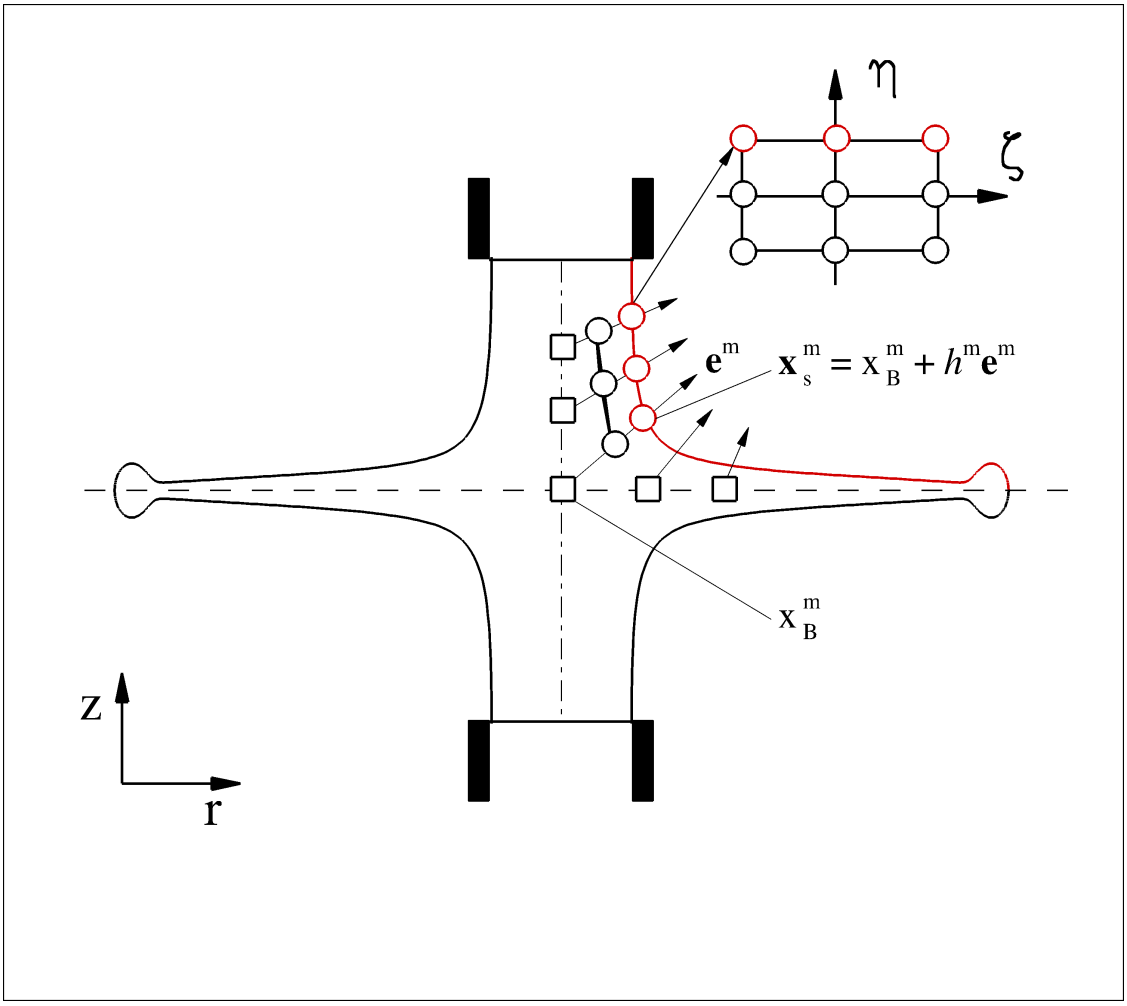


Figure 3.2. **Parametrization of the free interface using the method of spines.** The location $\mathbf{x}_s$ of the finite element nodes on the deforming interface (red line) is parametrized at each timestep by a distance $h^m$ measured along spines (arrows) defined by base point $\mathbf{x}_b^m$ and a direction $\mathbf{e}_m$.

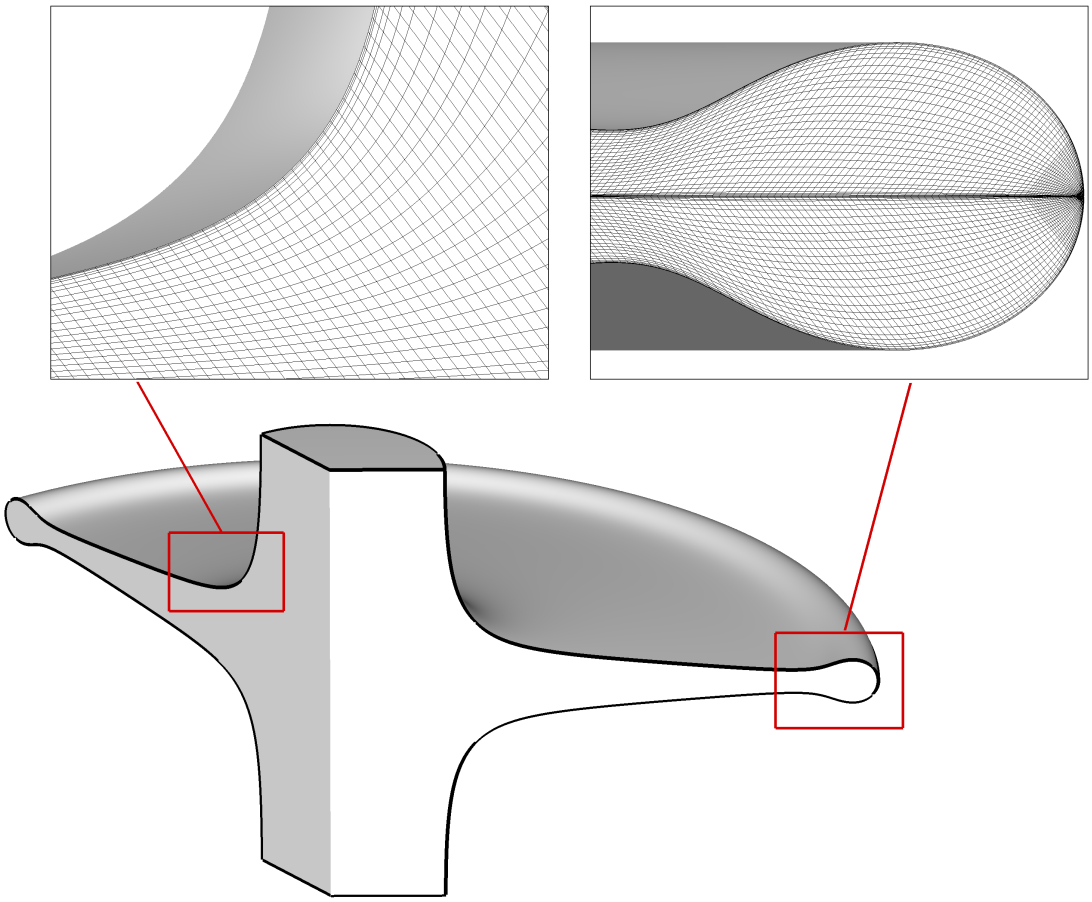

Figure 3.3. **Typical finite element mesh on the expanding liquid sheet.** An example of finite element mesh of jet impingement used in the simulations in this Chapter show that mesh is structured in a way to better represent the fluid interface, both at the transition region (left inset) and close to the bounding rim (right inset).

### 3.1.4 Results and Discussion

By solving the full Navier-Stokes system of equations, the direct numerical simulations enabled a detailed analysis of the influence of viscosity on the dynamics of jet impingement. The analysis reveals important differences between the viscous and inertial impingement dynamics in both the early and the late stages of sheet formation.

#### Early Stages of Sheet Expansion

Figure 3.4 illustrates the free-surface dynamics developed immediately after the impact of two laminar liquid jets in the inertial regime ($Re = 3000$). The pressure field shows that, as expected, the pressure rises sharply in the vicinities of the impact point due to the dissipation of the kinetic energy of the jets. Accordingly, results shows that the dimensionless stagnation pressure $p \approx 200$ (red in the figure) agrees well with the estimate $p = 1/4\ We$, which can be calculated by balancing pressure and inertia forces. This region of high pressure around the stagnation point drives flow in the radial direction forming the incipient liquid sheet observed in Figure 3.4. This is probably the first time that the formation of the expanding sheet is analyzed numerically at such an early stage.

As time progresses, the liquid at the tip of the expanding sheet accumulates in a toroidal rim under the influence of surface tension, as exemplified in the high Re case of Figure 3.5. The toroidal rim begins to form very early in the expansion process, in a manner similar to that observed in the experiments by Clanet and Villermaux (2002, Fig. 10).

As time progresses further, inertia generates additional capillary waves behind of the bounding rim of the low-viscosity sheet, as shown in Figure 3.6a. Moreover, Figure 3.6b demonstrates that the liquid attains the jet velocity at about two jet radii from the stagnation point and, after a brief acceleration at the rim neck, the velocity decreases near the edge of the sheet because of the surface tension forces

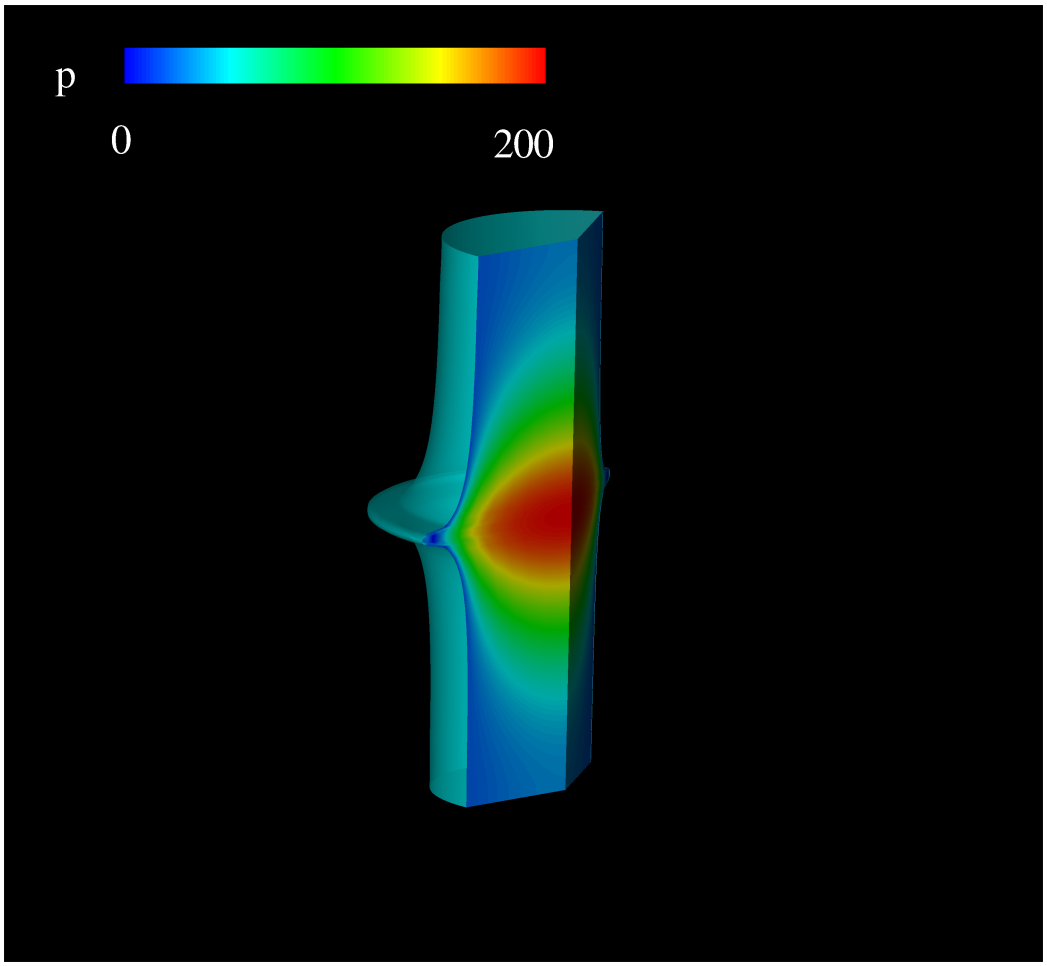


Figure 3.4. **Incipient radial sheet formed by the impingement of two laminar liquid jets.** Pressure field developed immediately after the impingement of two laminar liquid jets in the inertial regime. The high pressure developed in the impact region (red in the figure) drives fluid in the radial direction forming an incipient liquid sheet. Here, the jet Reynolds number is $Re = 3000$, and the Weber number is $We = 800$.

Figure 3.5. **Toroidal rim formed during impingement of two laminar liquid jets.** Liquid sheet developed shortly after the impingement of two laminar jets in the inertial regime. The liquid at the edge of the expanding sheet accumulates in a toroidal rim under the influence of surface tension. Here, the jet Reynolds number is $Re = 1000$, and the Weber number is $We = 200$.

and the inertia of the mass of fluid accumulated in the rim. A clear indication exists in the experiments by Clanet and Villermaux (2002) that the velocity of the liquid sheet is larger than the speed of the bounding rim, as observed in the simulations in Figure 3.6b.

The critical influence of the liquid viscosity in the early stages of sheet formation is illustrated in Figure 3.7, which compares incipient sheet profiles for three different jet Reynolds numbers. In the high Re case illustrated in Figure 3.7a the liquid accumulates in a toroidal rim under the influence of surface tension as discussed above.

As the jet Reynolds number progressively decreases, viscous forces delay the formation of the toroidal rim as shown in Figures 3.7b and 3.7c. Although in a different setting, the gradual disappearance of the toroidal rim as the liquid viscosity increases has been reported by Brenner and Gueyffier (1999) when comparing inertial and viscous planar sheets retracting under the action of capillary forces.

Moreover, the sheet profiles in Figures 3.7 also uncover the dramatic influence of viscosity on the thickness of the expanding sheets. As $Re$ decreases, from Figure 3.7d to Figure 3.7f, viscous effects become increasingly important, and the thickness of the liquid sheets increases as a consequence of the enhanced momentum transfer.

### Later Stages of Sheet Expansion

The influence of viscosity in the long time limit is illustrated in Figures 3.8 and 3.9. The figures compare both the midplane velocity $v$ (Fig. 3.8) and the dimensionless half sheet thickness $h$ (Fig. 3.9) for a high viscosity sheet with $Re = 0.001$ and for the high inertia sheet with $Re = 1000$ discussed at early times in Figure 3.7a.

For the high jet Reynolds number case, inertial effects dominate the dynamics, and so the liquid sheet expands at constant velocity $U$ unopposed by viscous stresses as shown in Figure 3.8 (triangles).

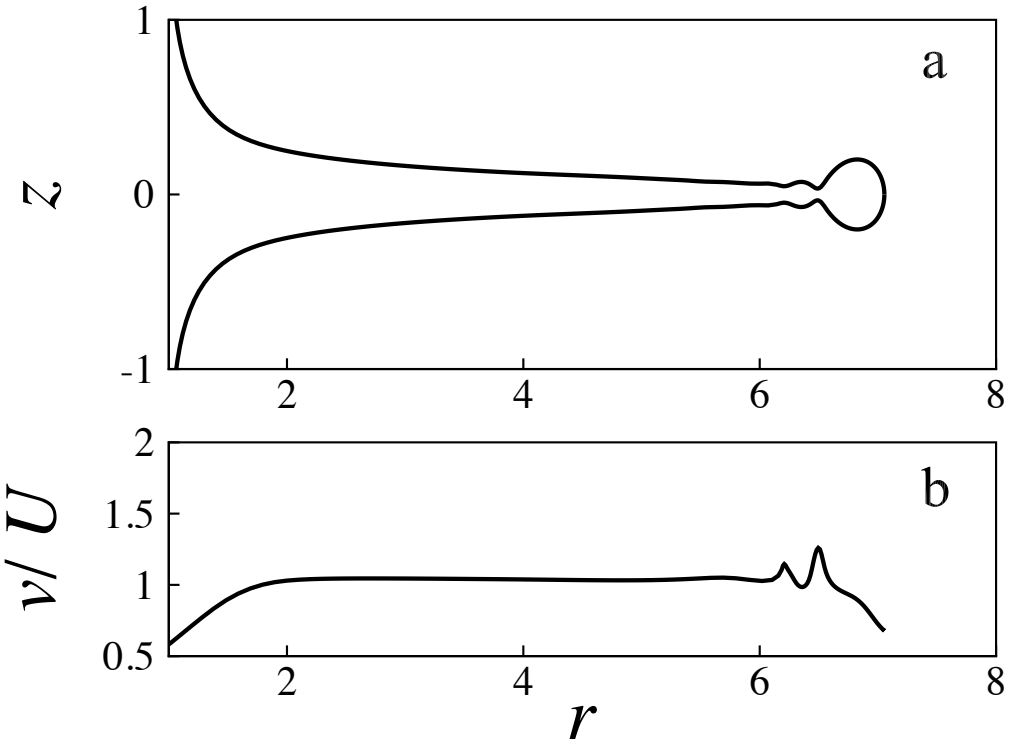


Figure 3.6. **Shape and midplane velocity of an expanding inertial sheet. (a)** Profile of the liquid sheet corresponding to Figure 3.5 at a later time in which the sheet edge is 7 jet radii away from the impact point. As time progresses, the inertia of the sheet generates capillary waves behind the bounding rim. **(b)** Normalized velocity $v/U$ along the impact plane. The liquid attains the jet velocity $U$ shortly after the stagnation region, and then slows near the edge of the sheet due to the action of surface tension.

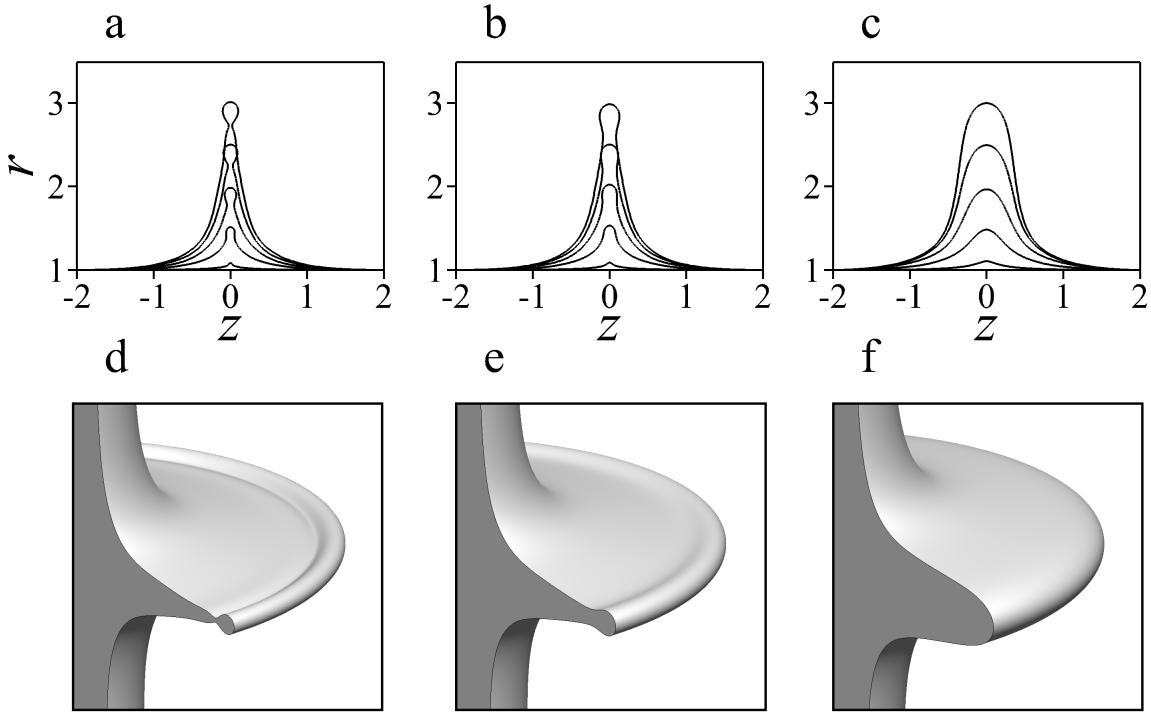


Figure 3.7. **Influence of viscosity on the shapes of radially expanding sheets.** Profiles of axisymmetric liquid sheets during the early stages of expansion for the jet Reynolds number are **(a, d)** $Re = 1000$, **(b, e)** $Re = 100$, and **(c, f)** $Re = 10$. As the viscosity of the liquid increases, the thickness of the sheet increases, and viscous forces delay the formation of the toroidal bounding rim. Here, the Weber number is $We = 200$, and the profiles correspond to sheet edges located at 1.1, 1.5, 2, 2.5 and 3 jet radii away from the impact point.

Accordingly, the sheet thickness decreases as $h = 1/2\ r^{-1}$ as required by mass conservation as shown in Figure 3.9 (triangles). Therefore, the simulations for the high inertia sheet are in good agreement with the classical results by Taylor (1960) for inviscid sheets, which are depicted as a solid line in Figures 3.8 and 3.9 for comparison. Note, however, that the agreement between theory and simulations occurs after a flow rearrangement zone, which is confined to approximately two jet radii from the impingement region as shown by the cross-sectional velocity field of Figure 3.10.

More recently, observations of this inertial scaling were reported by Clanet and Villermaux (2002) from measurements in water sheets in the smooth region ($We < 1000$). Figure 3.11 shows that the agreement between their experiments and the simulations is excellent. In addition, both simulations (circles) and experiments (squares) confirm that inertial sheets thin at the theoretical rate $dh/dr = -1/2\ r^{-2}$ (solid line).

For the low jet Reynolds number case in Figure 3.8 viscous effects dominate the dynamics, and so the sheet expands at decreasing velocity hampered by viscous stresses (Fig. 3.8, circles). Contrary to the inertial case in which the sheet travels with velocity $U$, in the viscous case the velocity of the sheet is strongly affected by the viscous stresses developed during the transition from axial to radial flow in the impact region. Nevertheless, the scaling of the viscous velocity can be explained by a simple one-dimensional force balance in the Stokes limit, which yields the relationship $v \sim 1/r$ exhibited by the simulations.

Indeed, neglecting inertial and surface tension forces in the Stokes limit, a simple force balance shows that the radial gradient of momentum flux must remain constant in the liquid sheet. This approximation yields

$$\frac{d}{dr}\left(r\frac{dv}{dr}\right) - \frac{v}{r} = 0, \tag{3.11}$$

which prescribes a radial velocity $v$ that must scale as $r^{-1}$, as observed in the simulations in Figure 3.8 (circles) for radius $r > 2$. Accordingly, the simulations show that the axisymmetric sheet profile remains uniform to satisfy mass conservation (Fig. 3.9, circles). The simulations also confirm results from the one-dimensional force balance

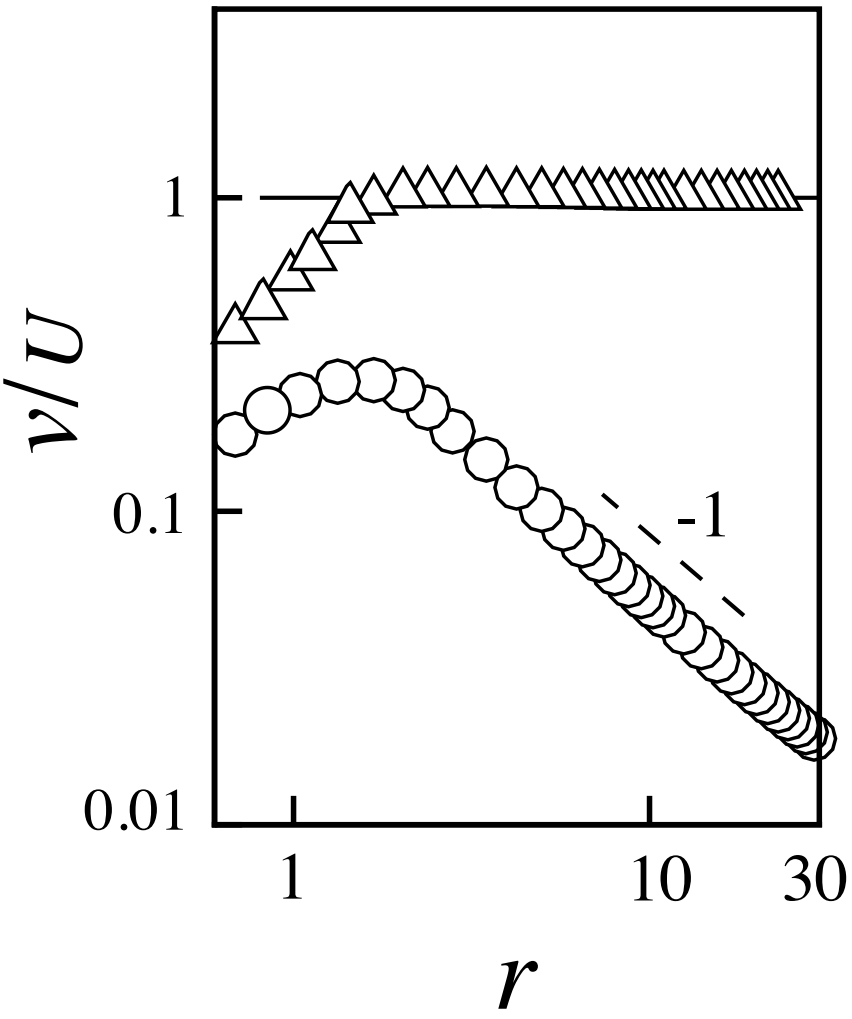


Figure 3.8. **Normalized sheet velocity in the inertial and Stokes regimes.** The normalized velocity $v/U$ along the impact plane remains constant in the inertial regime ($Re = 1000$, triangle) but decreases as $r^{-1}$ in the Stokes limit ($Re = 0.001$, circle).

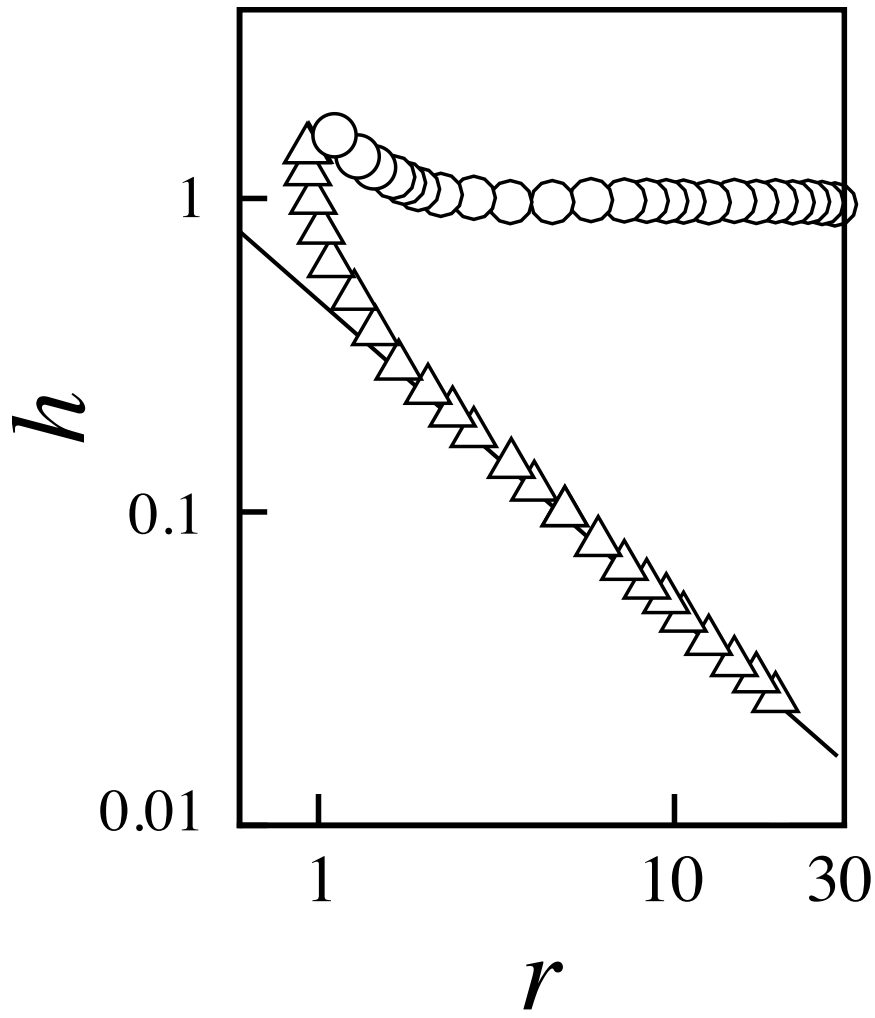


Figure 3.9. **Sheet thickness in the inertial and Stokes regimes.** The sheet thickness $h$ decreases as $r^{-1}$ in the inertial regime ($Re = 1000$, triangle) but remains essentially constant in the Stokes limit ($Re = 0.001$, circle).

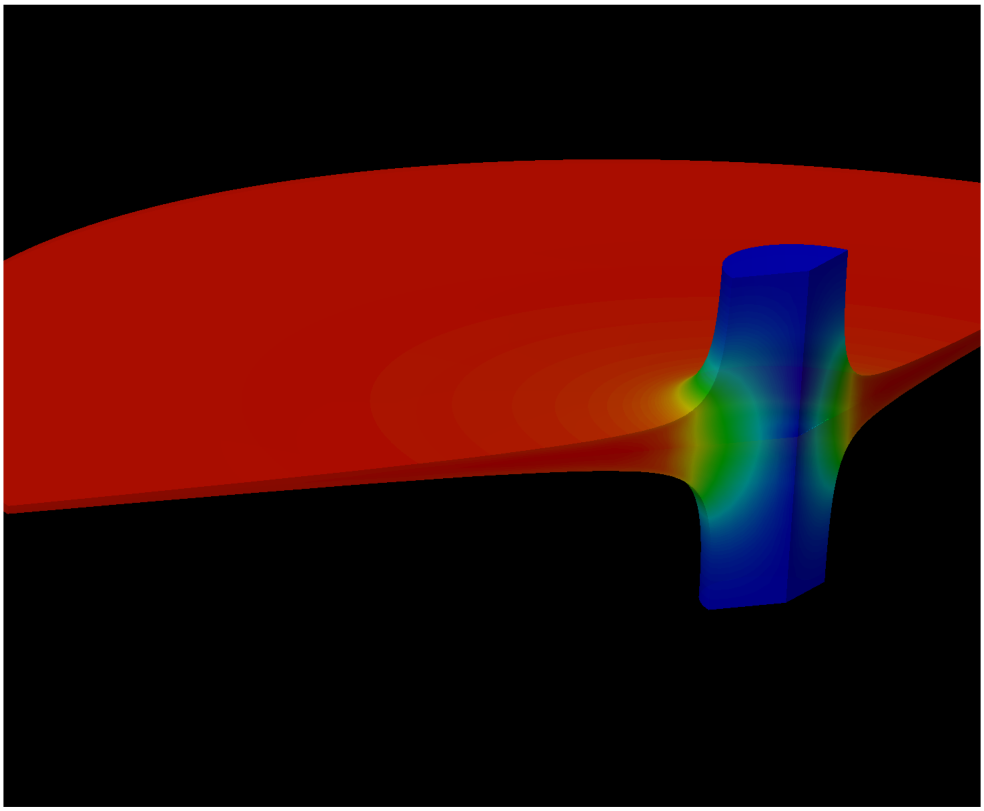

Figure 3.10. **Radial velocity field in the inertial regime.** Cross sectional radial velocity field shows that after approximately two jet radii from the impact point the sheet velocity both reaches the initial velocity $U$ of the jets (red in the figure) and becomes essentially uniform across the sheet thickness. Here, the jet Reynolds number is $Re = 1000$, and the Weber number is $We = 200$, red indicates high radial velocity and blue indicates low radial velocity.

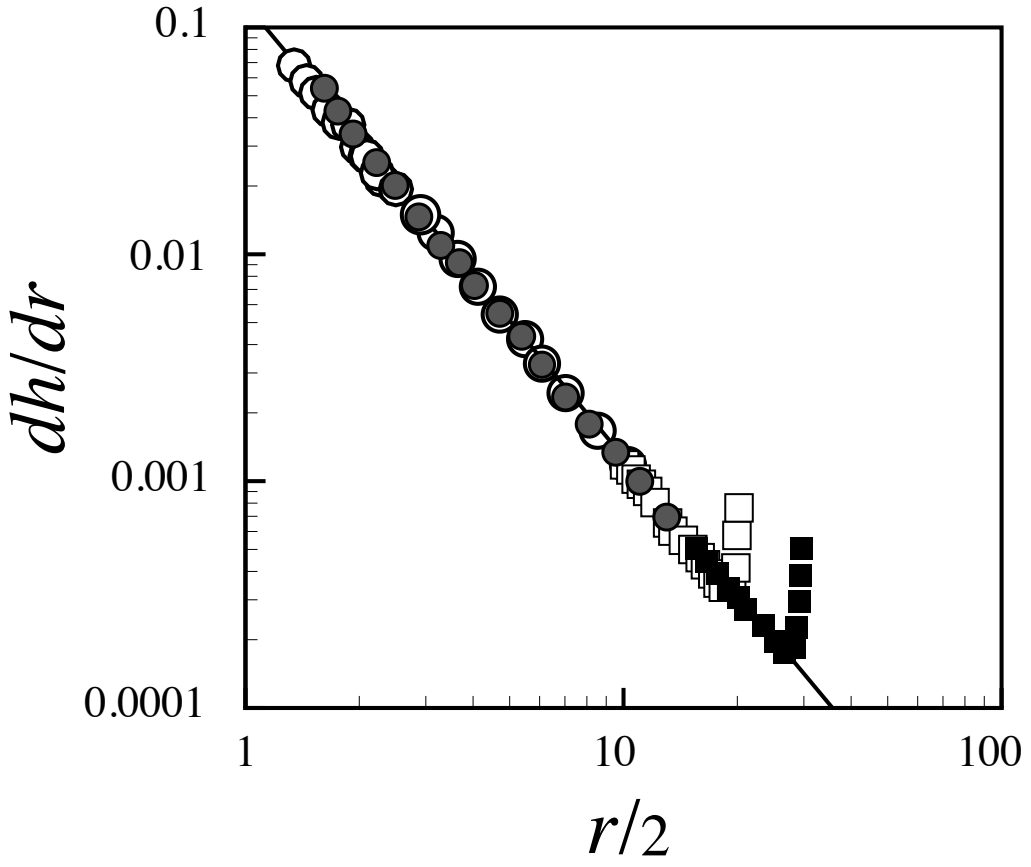


Figure 3.11. **Sheet thickness variation in the inertial regime.** Simulations results (circles) are in good agreement with measurements by interferometry technique by Clanet and Villermaux (2002) (squares) for water sheets with the jet Reynolds number $Re = 4100$, and the Weber numbers $We = 320$ (open symbols), and $We = 400$ (solid symbols). Both simulations and experiments confirm the power law relationship $dh/dr = -1/2r^{-2}$ predicted by Taylor (1960) (solid line).

developed by Lienhard and Newton (1966), which predicts the $r^{-1}$ scaling of the Stokes velocity. However, as with Equation (3.11), the one-dimensional approximation by Lienhard and Newton (1966) cannot predict the actual velocity and thickness of the viscous sheet predicted by the direct numerical simulations in Figures 3.8 and 3.9 due to the two-dimensional viscous stresses developed in the impingement region.

**Transition from Inertia to Viscous Dominated Impingement Dynamics**

Much as the dissipation of the kinetic energy of the jets drives the expansion of the inertial sheets, viscous dissipation generates the impact pressure that drives the radial expansion of the viscous sheets. Therefore, following the evolution of the impact pressure with the jet Reynolds number can give valuable insight into the transition from the inertia to viscous dominated impingement dynamics.

Figure 3.12 illustrates the evolution of the impact pressure for a large range of jet Reynolds numbers: $10^{-3} < Re < 10^{3}$. At low $Re$, while viscous effects are important, the simulations demonstrate that the impact pressure exhibits a power-law decline that scales as $Re^{-1}$. As $Re$ increases, viscous effects become less important, and the scaling abruptly changes at about $Re = 1$.

At high jet Reynolds numbers, the pressure rapidly stabilizes to a value $p \approx 1/4\ We$ independent of the $Re$ as the inviscid limit is approached. Transformed to its dimensional form, this expression becomes $\hat{p} \approx 1/2\ \rho\hat{U}^2$, which shows that the dimensional impact pressure $\hat{p}$ originates from the dissipation of the characteristic kinetic energy $\rho\hat{U}^2/2$, and thus confirms that the impingement dynamics is in the inviscid regime (Taylor, 1960).

Figure 3.13 illustrates sheet profiles in the region corresponding to the scaling $Re^{-1}$ in Figure 3.12. In this region, the simulations show that the viscous sheets are much thicker than the corresponding inertial sheet, which is depicted as a dashed line in Figure 3.13 for comparison. In addition, the simulations show for the first time

that in this region the thickness follow a logarithmic relationship $h \propto \ln r$ with the distance $r$ from the impact point.

As the liquid viscosity increases further, the sheets become thicker and more uniform, and the results in Figure 3.13 (circles) show that for $Re < 0.1$ the sheet thickness becomes essentially constant. This indicates that the dynamics has reached the Stokes limit previously discussed in Figure 3.9 (circles).

Contrary to the inertial regime in which the impact pressure is independent of the jet Reynolds number, the simulations show that when viscous effects are important the impact pressure depends on both the $Re$ and $We$ numbers. Indeed, a series of simulations in the viscous region $Re < 1$ and several $We$ numbers demonstrate that the dimensionless pressure scales precisely as $p \sim We/Re$, as illustrated in the Figure 3.14. In its dimensional form, this expression becomes $\hat{p} \sim \mu\hat{U}/a$, which shows that the dimensional pressure $\hat{p}$ scales as the characteristic viscous stress $\mu\hat{U}/a$, and so confirms that the dynamics is in the viscous regime.

**Internal Transition from Inertia to Viscous Dominated Impingement Dynamics**

A limited but interesting situation occurs in the transition region from inertia to viscous dominated dynamics. The simulations show that for jets with $Re = O(1)$, the viscous dominated regime is limited in space to a concentric belt around the impact point. This occurs because the contribution from the viscous term $v/r$ in Equation (3.11) is larger when the distance $r$ from the impact point is short.

Because the contribution from the viscous term $v/r$ decreases with the distance $r$ from the impact point, a liquid sheet which is viscously dominated near the impact point may become inertialy dominated away from it, if the contribution from the term $v/r$ is sufficiently small. Figure 3.15 tests this hypothesis for a liquid sheet with $Re = 3$. Note that the sheet profile (circles) precisely follows the viscous relationship

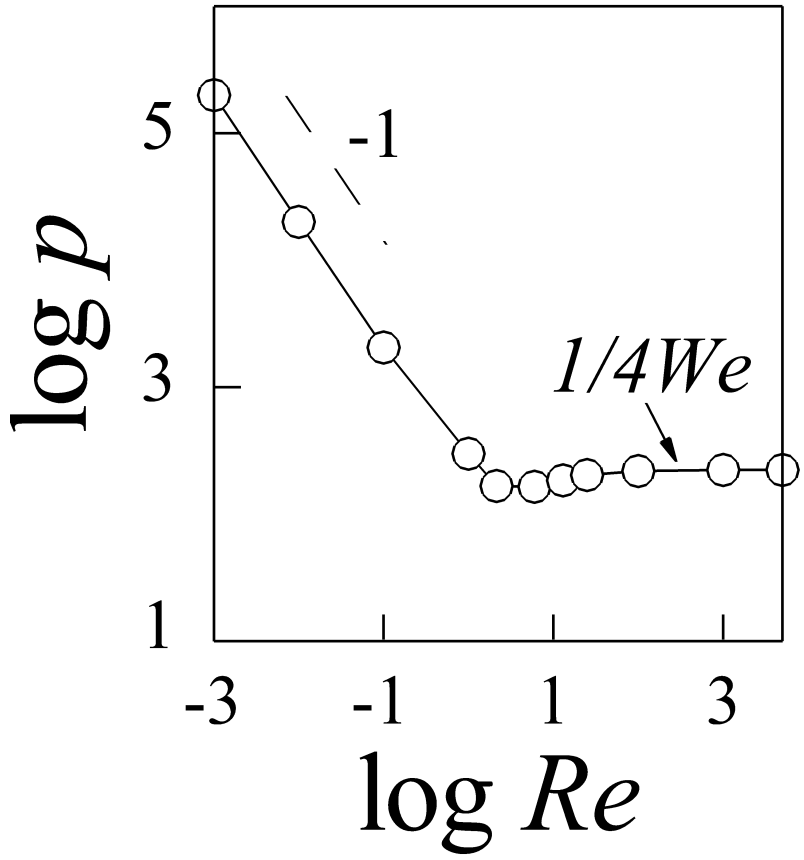


Figure 3.12. **Evolution of the impingement pressure as a function of the jet Reynolds number** $Re$**.** The dimensionless pressure in the impingement region follows a scaling $p \sim Re^{-1}$ at low $Re$, and approaches the relationship $p \approx 1/4\ We$ at high $Re$. Here the Weber number is $We = 800$.

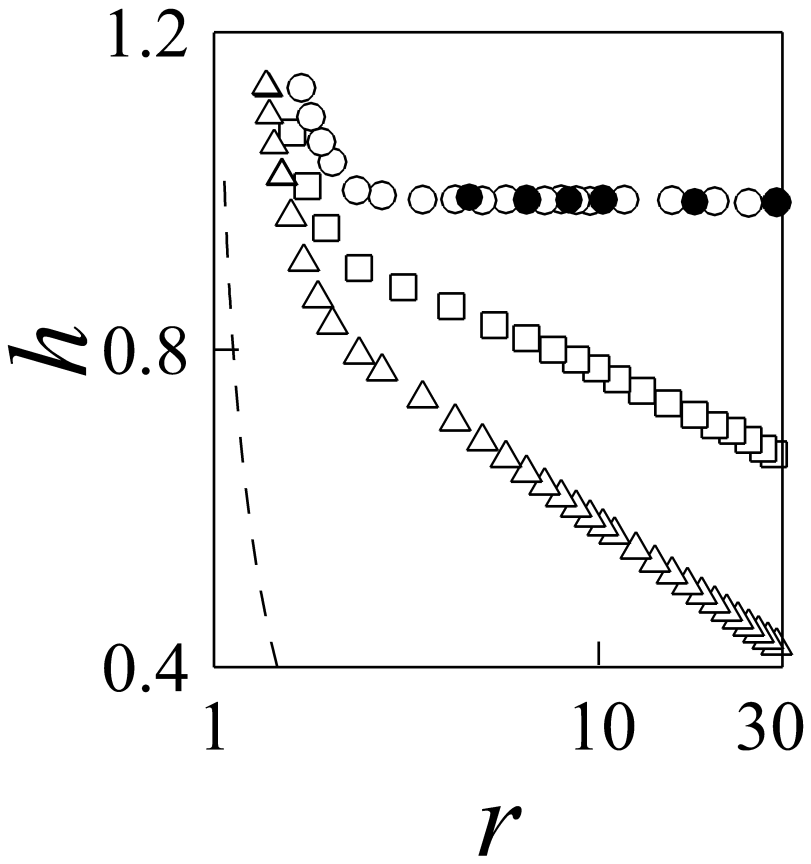


Figure 3.13. **Interfacial shapes with different jet Reynolds numbers** $Re$**.** Sheet profiles with the jet Reynolds numbers: $Re$ = 0.01 (open circle), $Re$ = 0.1 (solid circle), $Re$ = 1 (square), and $Re = 2$ (triangle). At low $Re$, the sheets are thicker than the inviscid one (dashed line), and closely follow a relationship $h \propto \ln r$.

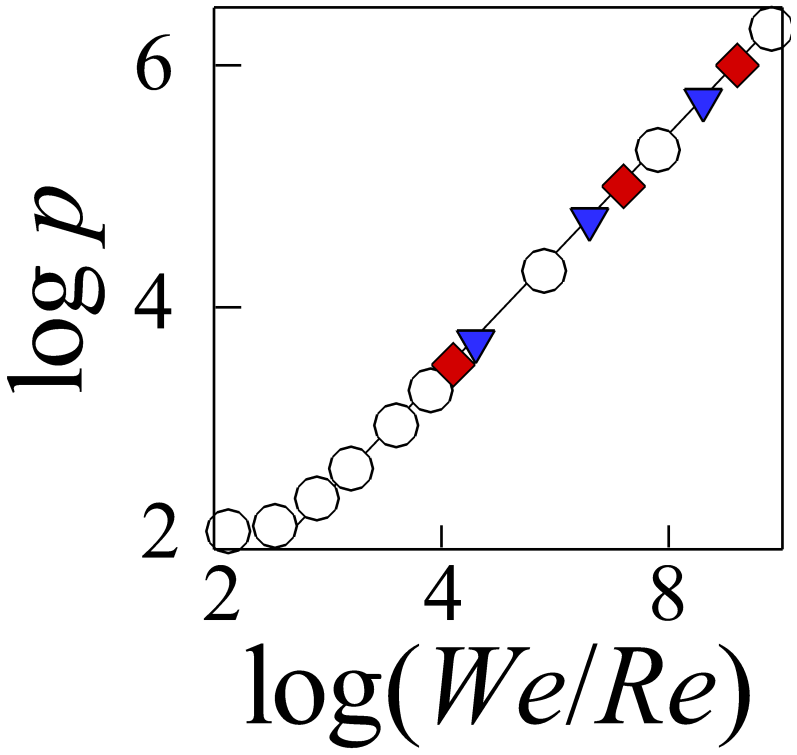


Figure 3.14. **Evolution of the impingement pressure as a function of the jet Reynolds number $Re$ and Weber number $We$.** At low $Re$ the dimensionless impingement pressure scales as $p \sim We/Re$. Here the Weber numbers are $We = 800$ (circle), $We = 400$ (red square), and $We = 200$ (blue triangle).

$h \propto \ln r$ (solid line) up to a distance $r \approx 10$, and above this distance the sheet abandons the viscous scaling.

A number of simulations for the jet Reynolds numbers $Re = O(1)$ show that the viscous belt shrinks rapidly as $Re$ increases, and essentially disappears at $Re \approx 10$. This is in agreement with the observed stabilization of the inertial pressure previously observed in Figure 3.12 for $Re > 10$. It is also in direct agreement with recent experimental observations by Villermaux et al. (2013, Fig. 3), which show that radially expanding liquid sheets are still inertial for jet Reynolds number as low as $Re \approx 30$. Figure 3.16 illustrates the shrinkage of the concentric viscous belt. The figure shows the radial velocity contours (Fig. 3.16a) and sheet thickness (Fig. 3.16b) for a radially expanding liquid sheet with $Re = 10$. For this jet Reynolds number, the viscous belt is very small, and the cross-over from viscous to inertial dynamics occurs at approximately three jet radii from the impact point. Indeed, Figure 3.16a shows that above $r \approx 3$ the velocity remains essentially constant, which is the characteristic behavior of the inviscid dynamics. The transition is clearly observed in Figure 3.16b, which shows the sheet thickness as a function of the radial distance. The figure shows that the sheet thickness (circles) decreases following the scaling $h \sim \ln\ r$ characteristic of the viscous dynamics up to the cross-over radius $r \approx 3$ (solid line), and then decreases with the radial distance following the inertial scaling $h \sim 1/r$ (dashed line).

### 3.1.5 Conclusion

This Section presented a numerical analysis of the influence of the liquid viscosity on axisymmetric sheets resulting from the impingement of laminar liquid jets. Results show that viscous sheets expand at a gradually diminishing speed hampered by viscous stresses. As a consequence, viscous sheets are thicker than the corresponding inertial ones, and become thicker and more uniform as the viscosity of the liquid increases.

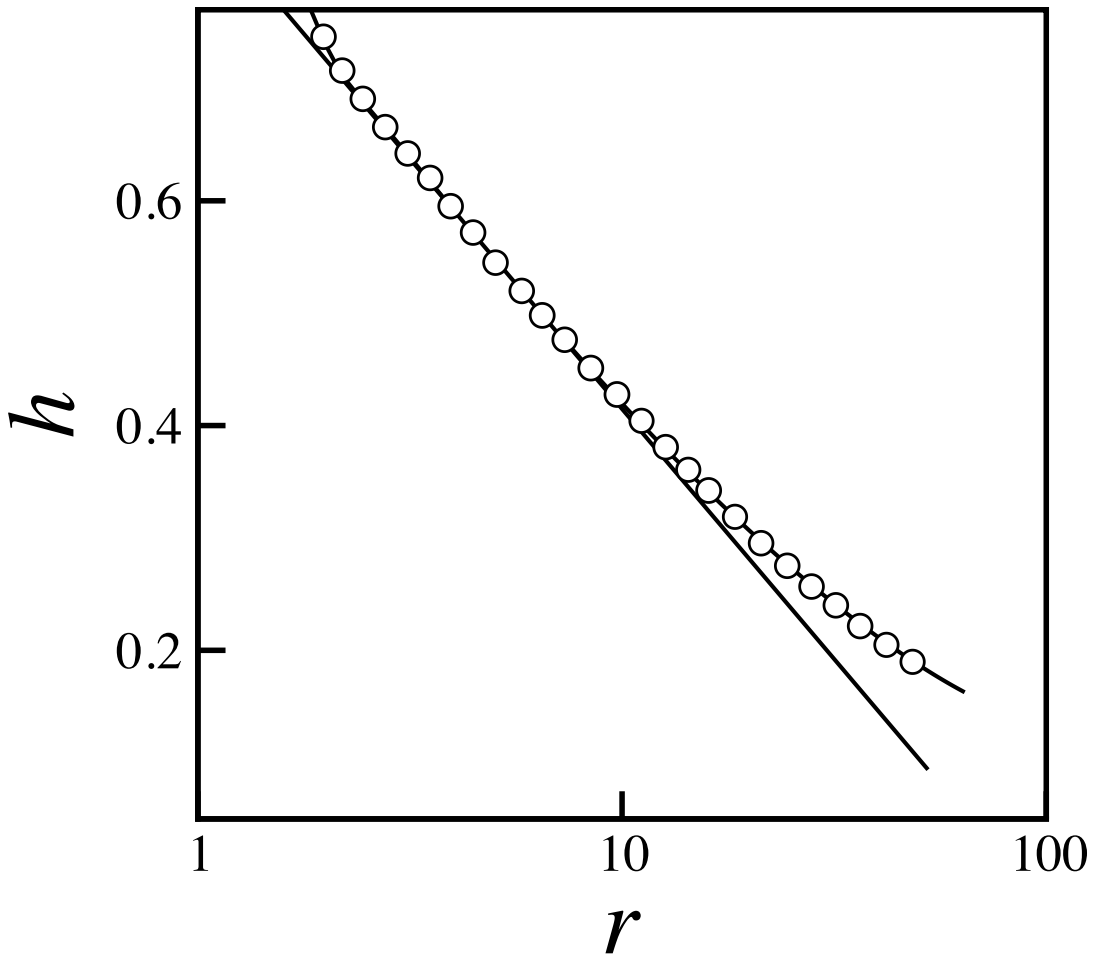


Figure 3.15. **Impingement dynamics for the jet Reynolds number $Re = O(1)$.** Profile of a liquid sheet with the jet Reynolds number $Re = 3$ (circle) illustrates the formation of a viscous belt around the impact region. The profile falls onto the viscous scaling at small radius but departs from it at $r \approx 10$ where tangential viscous stresses are weaker.

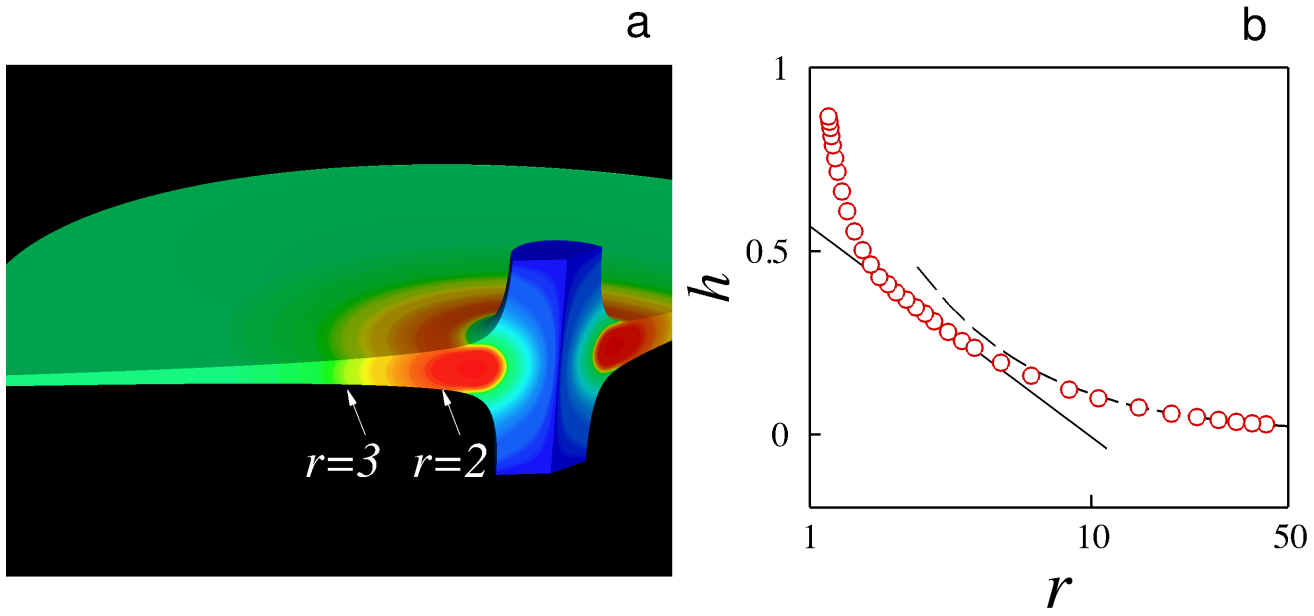


Figure 3.16. **Viscous belt in a fluid sheet for the jet Reynolds number** $Re = 10$**.** Cross sectional radial velocity and profile of a liquid sheet with $Re = 10$ illustrate the formation of a small viscous belt around the impact region. **(a)** The radial velocity remains essentially constant in the inertial region $r > 3$. **(b)** The sheet profile (circles) falls onto the viscous scaling at small radius (solid line) and onto the inviscid scaling for $r > 10$ where tangential stresses are weaker.

Simulations also show that for intermediate liquid viscosities the thickness of the expanding sheet decreases at a rate $dh/dr \sim r^{-1}$, contrary to the inviscid case in which the thickness decreases at the much faster rate $dh/dr \sim r^{-2}$. For high liquid viscosities, the velocity of the expanding sheets decrease as $1/r$, and so the thickness becomes uniform to satisfy mass conservation.

Results also demonstrate that the impact pressure responsible for driving the radial expansion of the liquid sheet scales as $We/Re$ in the viscous dominated regime due to the viscous dissipation in the impingement region. As a consequence, and contrary to the inviscid case, the velocity of a viscous sheet after impingement is lower than the velocity of the impinging jets.

It is expected that these new insights into the mechanisms of jet impingement at intermediate and low Reynolds numbers will enhance the current understanding of industrial spray and atomization systems involving viscous fluids. The model solves the complete Navier-Stokes system, and so fully account for the interplay of inertia, capillary and viscous forces during jet impingement. However, the results are limited by model assumptions that restrict the analysis to smooth axisymmetric systems. Therefore, future works should generalize this study to allow different angles of impingement, or to include the action of the surrounding air at high Weber numbers, in order to enable a more complete understanding of the influence of viscosity in the mechanisms of jet impingement.

## 3.2 Impingement of Shear-thinning Liquid Jets

Due to its fundamental scientific interest and numerous applications in spray and atomization systems, the physics of impinging liquid jets has been extensively studied since the pioneering works by Savart (1833) and Taylor (1960). However, most studies have only considered impinging jets of simple fluids such as water, where rheology plays no role, and little is known about the impingement of jets of complex fluids, despite their importance in industrial, space and defense technologies.

Section 3.1 reported simulations that enabled a detailed analysis of the influence of viscosity on the impingement of viscous liquid jets. This Section extends the analysis to viscous jets of complex fluids. Specifically, high-fidelity numerical simulations are used to study the dynamics of non-Newtonian shear-thinning impinging jets as a model system for jets of complex fluids frequently used in industrial and defense technologies, such as paints, food emulsions, polymeric solutions, and gelled propellants.

Computations reveal that during the impingement of jets of complex fluids, shear stresses create a region of low-viscosity in the vicinity of the impact point. As a consequence, viscous shear-thinning sheets are thinner and flow faster than the corresponding Newtonian ones. Shear thinning also enhances the growth of the toroidal rim bounding the resulting expanding liquid sheet. Together, results in this Section highlight the large impact of the fluid rheology on the dynamics of jet impingement. This study is anticipated to be a starting point for more sophisticated rheological models for the impingement of jets of non-Newtonian viscoelastic fluids.

### 3.2.1 Introduction

The impingement of facing liquid jets is of fundamental fluid mechanics interest and practical importance in numerous industrial applications, from spray drying, micro-mixing, and emulsification in the food processing industry to fuel and propellant atomization in combustion and propulsion engines (Ashgriz, 2011, Bremond and Villermaux, 2006, Clanet and Villermaux, 2002, Lefebvre, 1988, Mahajan and Kirwan, 1996, Ryan et al., 1993, Sutton, 1992, Villermaux et al., 2013).

Due to its fundamental and practical implications, theories and computational models to describe the dynamics of jet impingement have being actively developed since the pioneering works by Savart (1833), Ranz (1959), Taylor (1960), and later by Huang (1970). Most of these works, however, are limited to the impingement of simple liquid jets. In contrast, the impingement of complex liquid jets has re-

ceived much less attention, even though industrial applications often involve the use of complex fluids with non-Newtonian shear-thinning or viscoelastic rheological behavior (Baek et al., 2011, James et al., 2009, Kampen and Ciezki, 2007, Mallory and Sojka, 2014, Miller et al., 2005, Yang et al., 2012).

Here, the objective is to extend the current understanding of the nonlinear impinging dynamics of shear-thinning liquid jets. Previous theoretical and numerical works on the impingement of jets of shear-thinning liquids include linear stability analysis by Chojnacki (1997) and Liu et al. (1998). More recently, Mallory and Sojka (2014) developed a two dimensional linear stability analysis for the break up of expanding shear-thinning liquid sheets that extended previous works by Chojnacki (1997) and Dombrowski and Johns (1963) by considering a more realistic constitutive equation — the Carreau-Yasuda model — to describe the non-Newtonian liquid rheology. From these works, shear-thinning effects emerged as a critical issue on the dynamics of expanding liquid sheets. However, as demonstrated in several experimental works (Baek et al., 2011, James et al., 2009, Kampen and Ciezki, 2007, Miller et al., 2005, Yang et al., 2012), spray patterns and mechanisms leading to the atomization of the fluid sheet are largely affected by the flow dynamics in the impinging region, that is the region where the direction of the flow changes from axially dominated to radially dominated. How precisely the non-linear shear stresses developed in the impact region influence the impingement dynamics of shear-thinning liquid jets, and how these dynamics determine the velocity and thickness of the resulting radially expanding sheets remains poorly understood.

To better understand the nonlinear impinging dynamics of shear-thinning liquid jets the direct numerical simulation algorithm developed in Section 3.1 is extended here to include non-Newtonian liquid rheology. Following Mallory and Sojka (2014), the realistic Carreau-Yasuda model is used to describe the non-Newtonian shear-thinning behavior. The numerical model, which simultaneously resolves both the fluid dynamics of the impact region and that of the expanding liquid sheet, is described in Section 3.1.2. Section 3.2.4 discusses the results from the simulations. By varying

the degree of shear-thinning to represent non-Newtonian fluids frequently used in applications, the results reveal the influence of shear-thinning on the dynamics of jet impingement and contrast these new findings against the impingement dynamics of Newtonian liquid jets. Moreover, with focus on understanding shear-thinning effect at the impact point, results help reveal scaling laws describing the local viscosity in the impact region as a function of the Capillary number, and the degree of shear-thinning.

### 3.2.2 Problem Description and Governing Equations

The dynamics of non-Newtonian impinging jets are analyzed here by following the axisymmetric collision of two identical facing jets of a Carreau-Yasuda liquid. The colliding jets are characterized by a radius $a$ and axial velocity $\hat{U}$, as sketched in Figure 3.17. The fluid is characterized by a constant density $\rho$, viscosity $\mu_0$, and surface tension $\sigma$. The characteristic viscosity $\mu_0$ corresponds to the zero-shear-rate viscosity of the Carreau-Yasuda rheological model.

The governing equations and boundary conditions of the problem were previously stated in Section 3.1.2 and therefore will be briefly summarized here. The results will be discussed in dimensionless form using the jet radius $a$ as the characteristic length scale, $a\mu_0/\sigma$ as the viscous timescale, and $\sigma/a$ as the stress and pressure scale. Accordingly, the characteristic velocity is $\sigma/\mu_0$.

The evolution of the liquid velocity $\mathbf{v}(\mathbf{x}, t)$ and pressure $p(\mathbf{x}, t)$ are calculated by solving the full, generalized Navier-Stokes system:

$$\nabla \cdot \mathbf{v} = 0, \tag{3.12}$$

$$Re^2 \left( \frac{\partial \mathbf{v}}{\partial t} + \mathbf{v} \cdot \nabla \mathbf{v} \right) = \nabla \cdot \mathbf{T}, \tag{3.13}$$

where

$$\mathbf{T} \equiv \frac{1}{2}\, We \quad \left[ -p\mathbf{I} + \mu \left( \nabla \mathbf{v} + \nabla \mathbf{v}^T \right) \right] \tag{3.14}$$

is the dimensionless Cauchy stress tensor.

The dimensionless number of the problem include the jet Reynolds number

$$Re \equiv \frac{\rho \hat{U} a}{\mu_0}, \tag{3.15}$$

which characterizes the importance of inertial forces relative to viscous forces, and the Weber number

$$We \equiv \frac{2a\rho\ \hat{U}^2}{\sigma}, \tag{3.16}$$

which represents the ratio of inertial forces to surface tension forces. Simulations are carried out in the smooth region $We < 1000$ in which the adjoining gas phase can be considered dynamically inert (Clanet and Villermaux, 2002, Huang, 1970).

During the impingement of the Newtonian jets studied in Section 3.1, the liquid viscosity remains constant in space and time. By contrast, the viscosity of non-Newtonian liquid jets can change, and generally will. Places where the shear stress is large — for instance in the impact region — are places where the local viscosity is small. Places where the shear stress is small — for instance on the expanding liquid sheet — are places where the local viscosity is large.

The influence of the shear stress on the liquid viscosity is described here via a three parameter Carreau-Yasuda model. In the Carreau-Yasuda model, the local viscosity changes following a power-law relationship between the zero-shear-rate viscosity $\mu_0$ and the, typically much smaller, infinite-shear-rate viscosity $\mu_\infty$. In dimensionless form the Carreau-Yasuda model is:

$$\mu = \beta + (1-\beta)\big[\ 1 + (\alpha\ \dot{\gamma})^2\ \big]^{(n-1)/2}. \tag{3.17}$$

In Equation (3.17), $\mu$ is the dimensionless apparent viscosity in units of the zero-shear viscosity $\mu_0$. The parameter $\beta \equiv \mu_\infty/\mu_0$ is the dimensionless infinite-shear viscosity, the parameter $n$ is the Carreau flow index, and the parameter $\alpha$ is the dimensionless Carreau time constant. The dimensionless rate of deformation $\dot{\gamma}$ is calculated for axisymmetric jet impingement as

$$\dot{\gamma} = \sqrt{2\left(\frac{\partial v}{\partial r}\right)^2 + 2\left(\frac{v}{r}\right)^2 + \left(\frac{\partial v}{\partial z} + \frac{\partial u}{\partial r}\right)^2 + 2\left(\frac{\partial u}{\partial z}\right)^2}. \tag{3.18}$$

where $v$ and $u$ are the dimensionless radial and axial fluid velocity, respectively.

The relationship between the apparent viscosity $\mu$ and the rate of deformation $\dot{\gamma}$ is exemplified in Figure 3.18 for $n = 0.7$, $\alpha = 1$ and $\beta = 10^{-5}$. At low deformation rates the apparent viscosity is comparatively large, and shows a Newtonian plateau typically observed in non-Newtonian liquids, which corresponds to the dimensionless zero-shear viscosity $\mu = 1$. When the deformation rate is larger than $1/\alpha$, the viscosity decreases with the deformation rate following a power-law relationship with slope $n - 1$. As the deformation rate increases further, the viscosity approaches a second Newtonian plateau, which corresponds to the dimensionless infinite-shear viscosity $\beta$.

### 3.2.3 Direct Numerical Simulation

The numerical method used in this Section follows the same design that applied to the direct numerical simulations of viscous jet impingement in Section 3.1, and, therefore is only briefly summarized here. The Navier-Stokes system equations (Eq. 3.12 and 3.13) with the incorporation of the Carreau-Yasuda model (Eq. 3.17) describing the non-linear rheological property of the fluids used in the jet impingement along with the kinematic equation (Eq. 3.9) are simultaneously solved using a finite-element algorithm with the arbitrary Lagrangian-Eulerian method of spines to parametrize the deforming fluid interface and adaptive time integration. A second-order trapezoidal Adam-Bashforth predictor method was used to discretize the time derivatives (Gresho et al., 1980) to reduce time truncation errors, and the time steps were adaptively chosen using the first-order continuation method by Corvalan and Saita (1991) to improve computational efficiency. Mesh independence studies at various resolutions were carried out and meshes with 8000-10000 degree of freedom were selected for the simulations depending on the jet Reynolds number $Re$ and Weber number $We$.

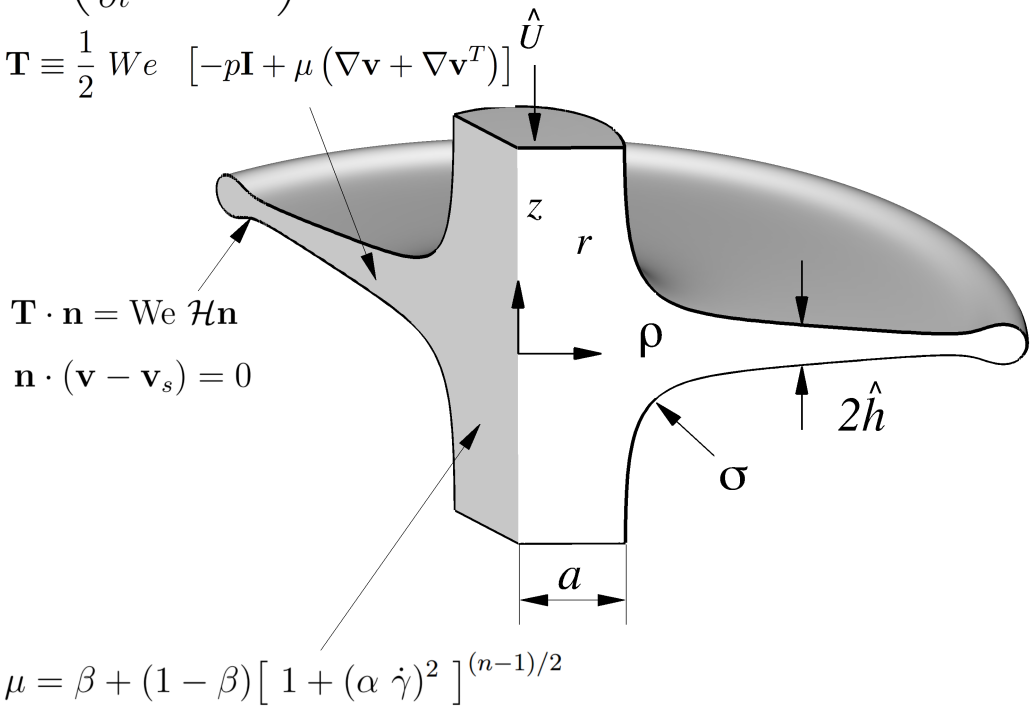


Figure 3.17. **Impingement of two laminar jets of Non-Newtonian fluids.** Axisymmetric impingement of two shear-thinning liquid jets of radius $a$ and velocity $\hat{U}$. The density of the liquid is $\rho$, and the surface tension $\sigma$. The thickness of the radially expanding liquid sheet is $2\hat{h}$. The sheet profile corresponds to the case discussed in Figure 3.21c.

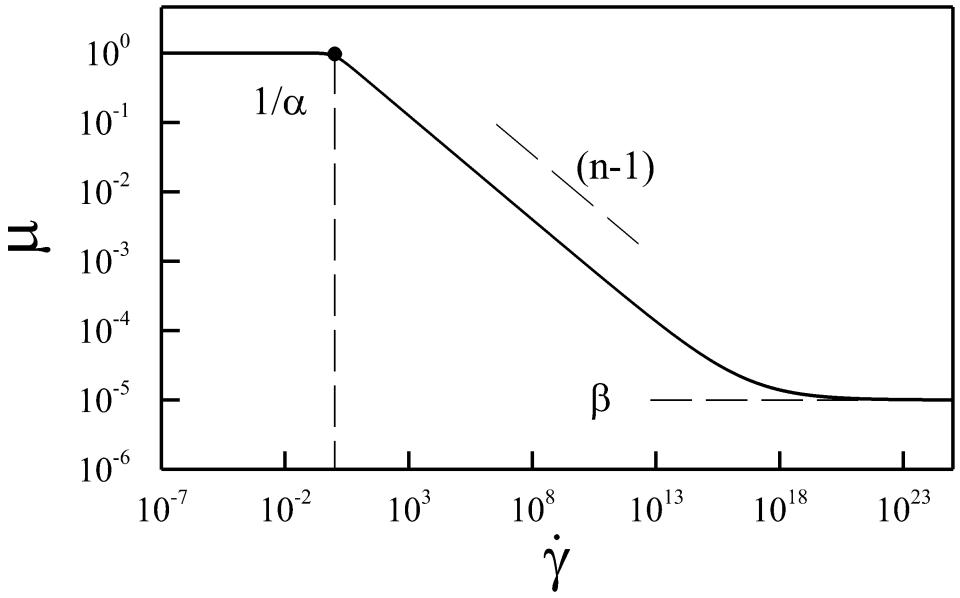


Figure 3.18. **Apparent non-Newtonian viscosity $\mu$ as function of the dimensionless shear rate $\dot{\gamma}$ predicted by the Carreau-Yasuda model.** Here the Carreau flow index is $n = 0.7$, Carreau time constant is $\alpha = 1$, and the dimensionless infinite shear viscosity is $\beta = 10^{-5}$.

### 3.2.4 Results and Discussion

This Section presents direct numerical simulations that enable a detailed analysis of the influence of shear-thinning rheology on the free-surface dynamics of jet impingement. The analysis reveals important differences between the Newtonian and the non-Newtonian impingement dynamics.

The non-Newtonian fluid rheology is described here by the three-parameter Carreau-Yasuda model of Equation (3.17), which realistically accounts for shear-thinning behavior. The parameters of the model vary widely with the type of fluid considered. To fix ideas, Table 3.1 summarizes data from a detailed study of the rheology of shear-thinning liquid gels carried out by Mallory (2012, Table 4.4) in the context of an study for the U.S. Army Research Office on the impingement of jets of gelled propellants.

Table 3.1. Carreau Yasuda rheological parameters for typical gelled fluids

| **Solution** | $\mu_0$ (**Pa.s**) | $\mu_\infty$ (**Pa.s**) | **n** | time constant (**s**) |
|---|---|---|---|---|
| 3 wt.-% HPC | $723 \pm 36$ | $1.45E-06$ | $0.23 \pm 0.01$ | $5.1 \pm 0.3$ |
| 0.5 wt.-% CMC-7HF | $0.11 \pm 0.01$ | $4.80E-08$ | $0.68 \pm 0.03$ | $0.031 \pm 0.002$ |
| 1.4 wt.-% CMC-7MF | $0.18 \pm 0.01$ | $3.13E-07$ | $0.8 \pm 0.04$ | $0.0103 \pm 0.005$ |
| 0.8 wt.-% CMC-7MF | $0.05 \pm 0.003$ | $3.99E-06$ | $0.85 \pm 0.04$ | $0.037 \pm 0.02$ |
| 0.06 wt.-% CMC-7MF 75 wt.-% glycerin | $0.2 \pm 0.01$ | $1.11E-07$ | $0.85 \pm 0.04$ | $0.158 \pm 0.008$ |
| 1 wt.-% Kappa carrageenan | $142 \pm 7$ | $1.61E-09$ | $0.113 \pm 0.006$ | $7.4 \pm 0.4$ |
| 1 wt.-% Agar | $743 \pm 37$ | $3.68E-09$ | $0.111 \pm 0.006$ | $64 \pm 3$ |

HPC: Hydroxypropylcellulose

CMC: Carboxymethylcellulose

According to these data, the dimensionless infinite viscosity of the gels $\beta = \mu_0/\mu_\infty$ varies in the range $10^{-9} < \beta < 10^{-3}$, and the Carreau time constant $\alpha$ varies approximately in the range $1 < \alpha < 100$, assuming a surface tension similar to that of water, and a jet radius of 0.1 mm. Accordingly, for the simulations in this Section the dimensionless infinite viscosity is fixed at $\beta = 10^{-4}$, and the Carreau time constant is

fixed at $\alpha = 10$, unless otherwise stated. In the simulations, the Carreau flow index $n$ varies in the range $0.2 < n < 1$ (with $n = 1$ for Newtonian jets) during parametric analysis.

**Early Stages of Sheet Expansion**

The critical influence of the non-Newtonian rheology in the very early stages of sheet expansion is illustrated in Figure 3.19 for the impingement of viscous, moderately shear-thinning jets ($n = 0.6$). The figure shows the apparent viscosity field developed during the early stages of sheet expansion. Results demonstrate that the liquid viscosity drops significantly in the impact region, reaching values as low as 5% of the zero-shear viscosity shortly after impingement (Fig. 3.19). This is due to the strong deformation rate developed in the impact region as the fluid abruptly changes direction from axial to radial flow. As time progresses, and the shear stress decreases in the expanding sheet, the apparent viscosity slowly increases to about 40% of the zero-shear viscosity in the incipient toroidal rim as illustrated in Figure. 3.20.

Results further reveal that shear-thinning favors the early formation of a bounding toroidal rim in the expanding liquid sheets. This is illustrated in Figure 3.21, which compares incipient sheet profiles for shear-thinning jets with three different flow indexes: $n = 1$, $n = 0.8$, and $n = 0.6$. For the Newtonian ($n = 1$) and the weakly shear-thinning jets ($n = 0.8$) the toroidal rim is not observed at early times, as shown in Figures 3.21a and 3.21b. But this is not the case with the moderately shear-thinning jets ($n = 0.6$) shown in Figure 3.21c. Here, the fluid at the edge of the sheet accumulates in a well defined toroidal rim since very early in the expansion process, similarly to what is observed in inertial fluid sheets (Clanet and Villermaux, 2002). The sheet profiles in Figures 3.21 also demonstrate the dramatic influence of shear-thinning on the thickness of the nascent sheets. Indeed, as the flow index $n$ decreases, inertia becomes increasingly important, and the sheet thickness decreases due to the acceleration of the fluid (Figs. 3.21d, e, f).

Figure 3.22 compares the sheet profiles and the normalized midplane velocities as the edge of the sheets discussed in Figure 3.21 approaches $r = 10$. Results show that despite having identical viscosity at rest, the sheets flow at very different velocities. While the Newtonian liquid sheet with $n = 1$ flows at decreasing velocity opposed by viscous stresses (as discussed in Section 3.1), the shear-thinning liquid sheet with $n = 0.6$ flows at about the velocity of the impinging jets essentially unopposed by viscosity. Therefore, in this example the sheet dynamics transition from viscous dominated when $n = 1$ to inertially dominated when $n = 0.6$.

Together, these results demonstrate that the impingement dynamics of viscous liquid jets may become inertially dominated as a consequence of shear-thinning effects.

### Late Stages of Sheet Expansion

The influence of the non-Newtonian rheology in the late stages of sheet expansion is illustrated here by analyzing the impingement of moderately shear-thinning jets with flow index $n = 0.7$.

Figure 3.23 shows the cross-sectional viscosity field along the resulting radially expanding sheet. The results highlight the development of three qualitatively different regions depending on the distance $r$ from the impact point. First, in the region $r < 1$, the liquid viscosity reaches a minimum, approximately constant value due to the high but relatively uniform local stresses developed near the stagnation point. Second, in the intermediate region $1 < r < 10$, the liquid viscosity increases rapidly as the local shear stress decreases with the radial distance. Finally, in the region $r > 10$, the liquid viscosity reaches a maximum value and then remains essentially constant. Note that the local viscosity changes little across the thickness of the liquid sheet because the flow is essentially uniform in the axial direction.

The development of the three distinct regions is further highlighted in Figure 3.24, which shows the value of the midplane apparent viscosity as a function of the radial position for the same case discussed in Figure 3.23. In this example, the minimum

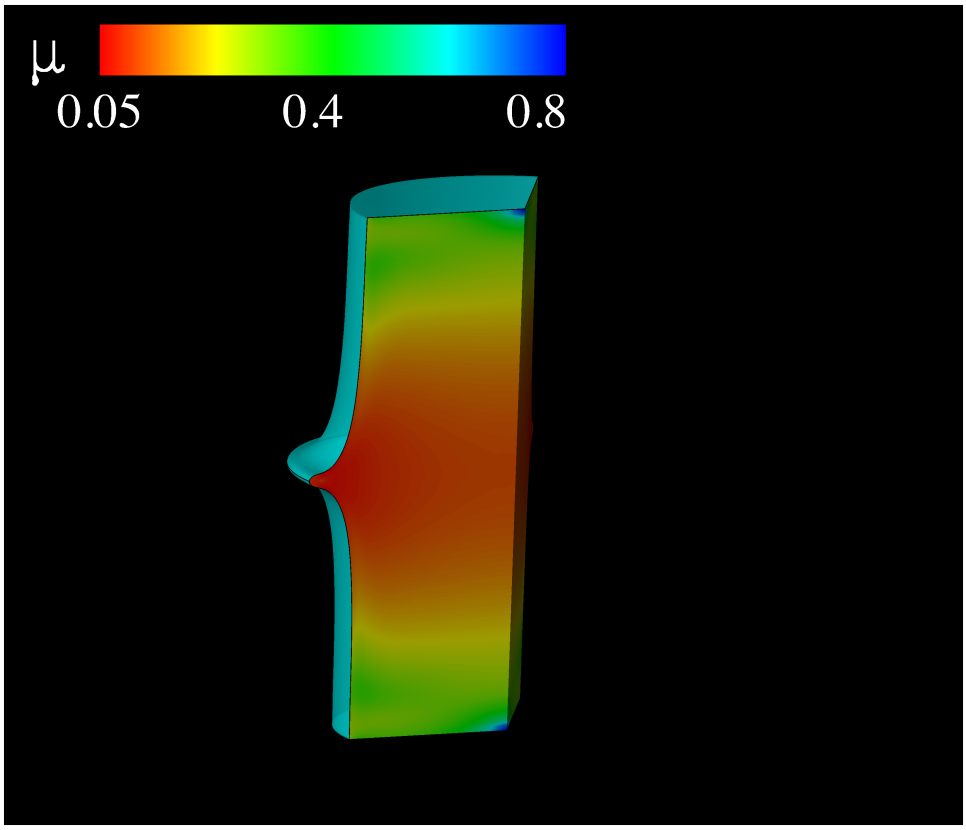


Figure 3.19. **Nascent sheet formed by impingement of shear-thinning liquid jets.** Apparent viscosity field $\mu$ developed immediately after the impingement of two laminar jets of moderately shear-thinning fluids ($n = 0.6$). The high rate of deformation developed in the impinging region creates a region of low viscosity (red in the figure) around the impact point.

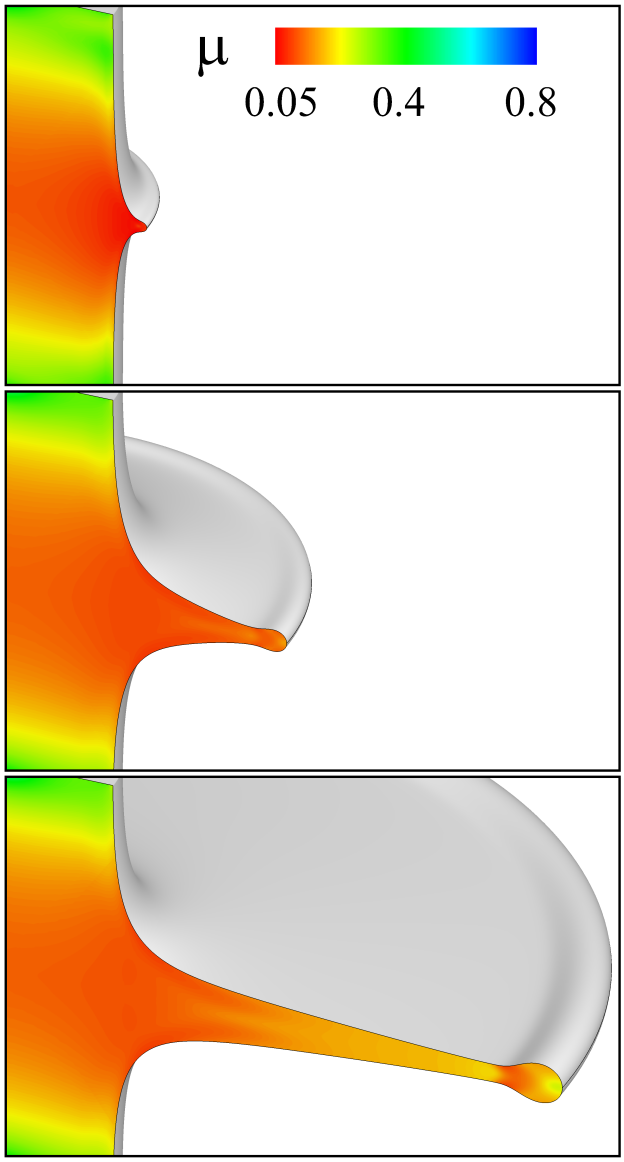


Figure 3.20. **Fluid sheet formed by impingement of laminar jets of shear-thinning liquids.** Evolution of the apparent viscosity field $\mu$ during the early stages of expansion for a slightly viscous ($Re = 10$), moderately shear-thinning fluid ($n = 0.6$). As the sheet expands, the viscosity slowly increases with the distance from the impact point. Here the Weber number is $We = 200$, and the profiles correspond to sheet edges are located at 1.2, 2, and 5 jet radii away from the impact point.

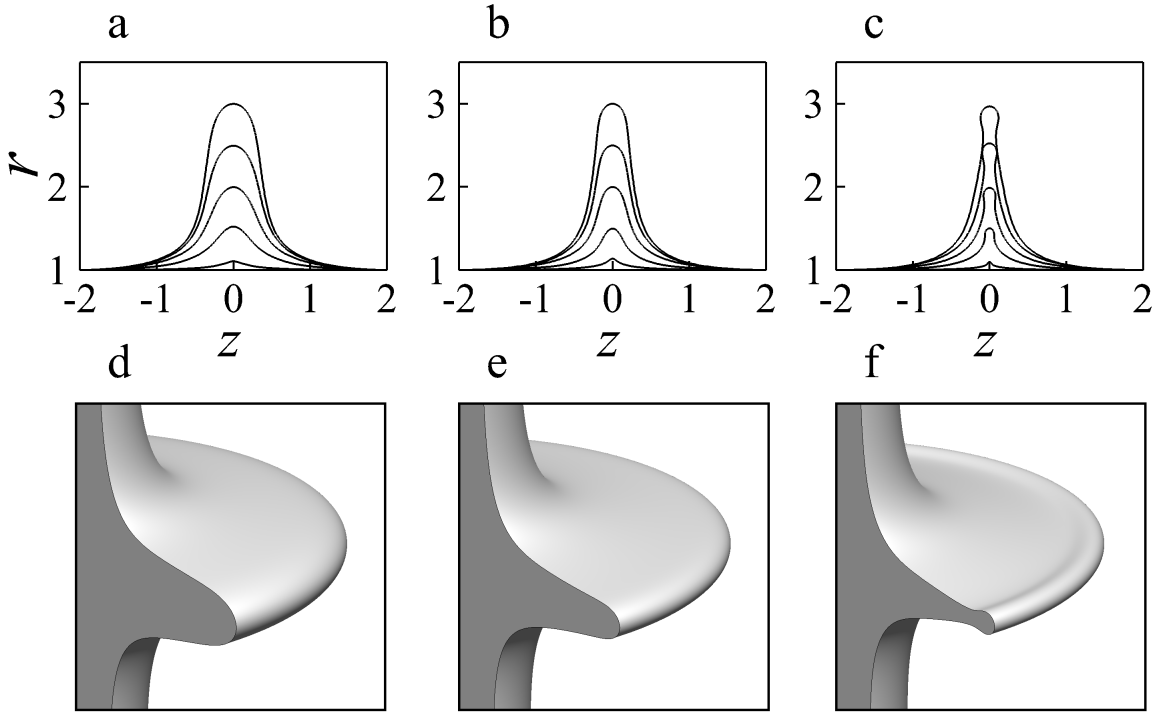


Figure 3.21. **Influence of shear-thinning on the shapes of radially expanding sheets.** Profiles of axisymmetric fluid sheets during the early stages of expansion for **(a, d)** Newtonian liquid $n = 1$, and shear-thinning liquid **(b, e)** $n = 0.8$, and **(c, f)** $n = 0.6$. As the flow index of the liquid decreases, the thickness of the sheet decreases, and higher degree of shear-thinning favors the formation of a bounding toroidal rim. Here, the jet Reynolds number is $Re = 10$, the Weber number is $We = 200$, and the profiles correspond to sheet edges located at 1.1, 1.5, 2, 2.5 and 3 jet radii away from the impact point.

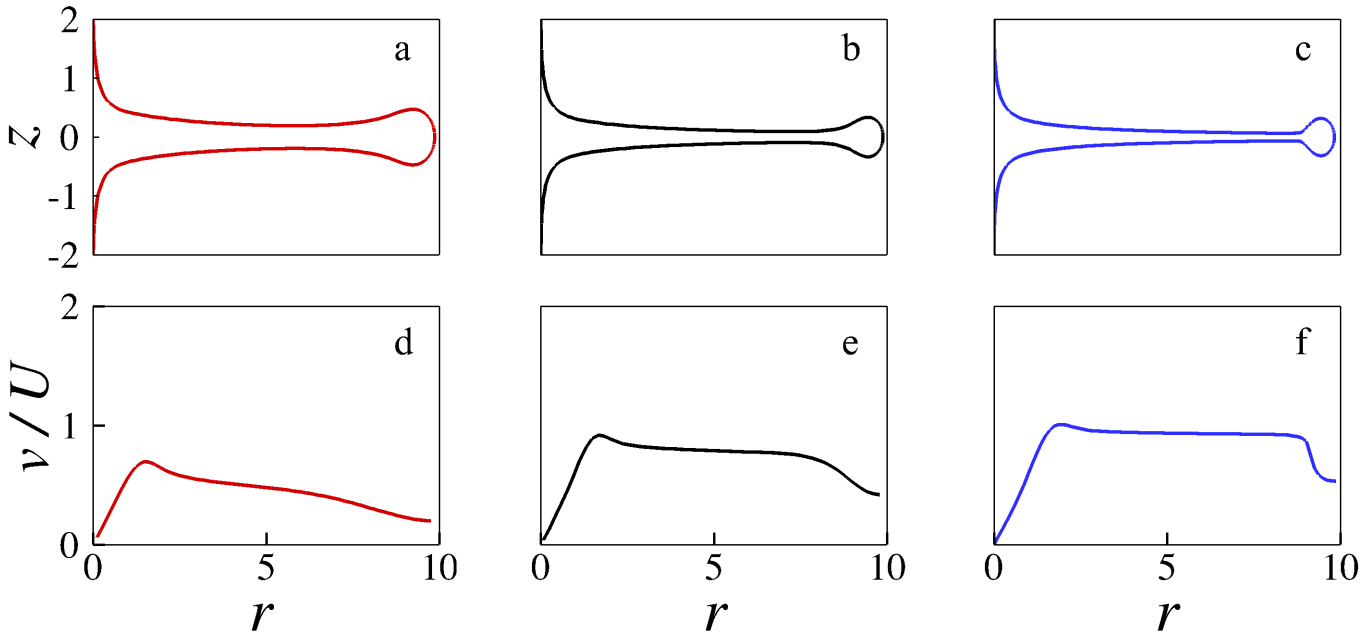


Figure 3.22. **Shape and midplane velocity of expanding shear-thinning sheets.** Profiles of axisymmetric fluid sheets for **(a)** Newtonian liquid $n = 1$, and shear-thinning liquids **(b)** $n = 0.8$, and **(c)** $n = 0.6$ corresponding to Figure 3.21 at later times in which sheet edges are 10 jet radii away from the impact point. As the degree of shear-thinning decreases, the sheet velocity increases and approaches the jet velocity $U$ **(d, e, f)**. Here, the jet Reynolds number is $Re = 10$, and the Weber number is $We = 200$.

dimensionless viscosity in the impact region is approximately $\mu \approx 0.17$, or about 1/6 of the zero-shear viscosity. Then the midplane viscosity increases in the intermediate region, and finally recovers the zero-shear normalized value $\mu = 1$.

These changes on the local viscosity of the shear-thinning sheet play a critical role in the resulting sheet thickness. Figure 3.25 shows the half thickness $h$ of the shear-thinning sheet of Figure 3.23 as a function of the radial distance (red circles). For comparison, the figure also shows three other cases. First, the green line shows the thickness of a Newtonian liquid sheet with constant viscosity $\mu = 1$, which corresponds to the zero-shear viscosity of the shear-thinning sheet. Second, the black line shows the thickness of a Newtonian sheet with constant dimensionless viscosity $\mu = 1/6$, which corresponds to the local viscosity of the shear-thinning sheet in the impact region. Finally, the figure also shows the thickness of the corresponding inviscid liquid sheet (blue line). A finding of practical importance illustrated in Figure 3.25 is that the shear-thinning sheet (circles) is substantially thicker than the corresponding inviscid Newtonian sheet (blue), and considerably thinner than the Newtonian sheet with the same zero-shear viscosity (green). Interestingly, near the impact region the thickness of the shear-thinning sheet decreases in a way that closely resembles that of the Newtonian sheet with the same viscosity as the shear-thinning sheet in the impact region (black solid line). In addition, after approximately 10 jet radius away from the impact point, where the viscosity of the shear-thinning liquid sheet becomes essentially constant, the shear-thinning sheet thins following the scaling $h \sim \ln r$ (black dashed line), characteristic of viscous Newtonian sheets (cf. Sec. 3.1.4).

**Effect of the Carreau Flow Index $n$**

For given values of the jet Reynolds and the Weber numbers, results show smaller viscosities at the impact point, and, therefore, thinner liquid sheets, with increasing degree of shear-thinning.

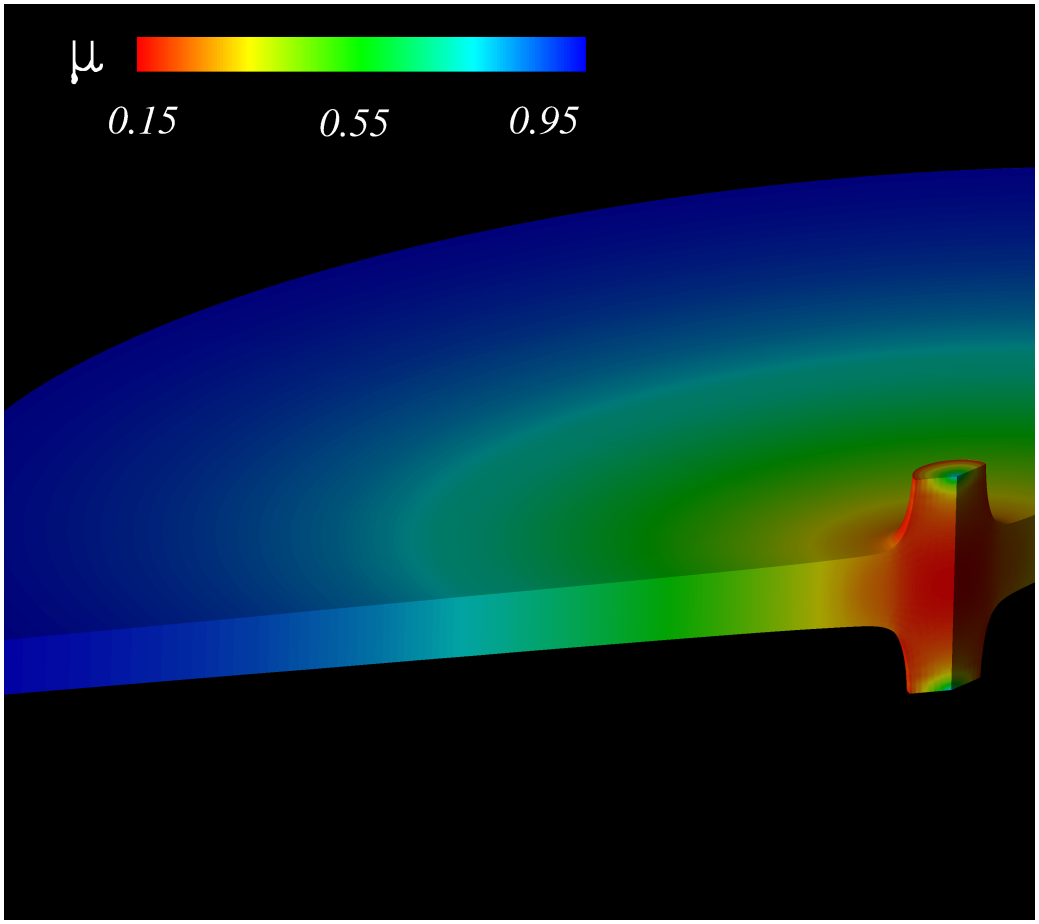


Figure 3.23. **Impingement of shear-thinning jets.** Local viscosity field developed during the axisymmetric collision of two identical shear-thinning laminar jets ($n = 0.7$). Large stresses developed in the impact region (red in the figure) drastically reduces the local viscosity. Here, the jet Reynolds number is $Re = 1$, and the Weber number is $We = 400$.

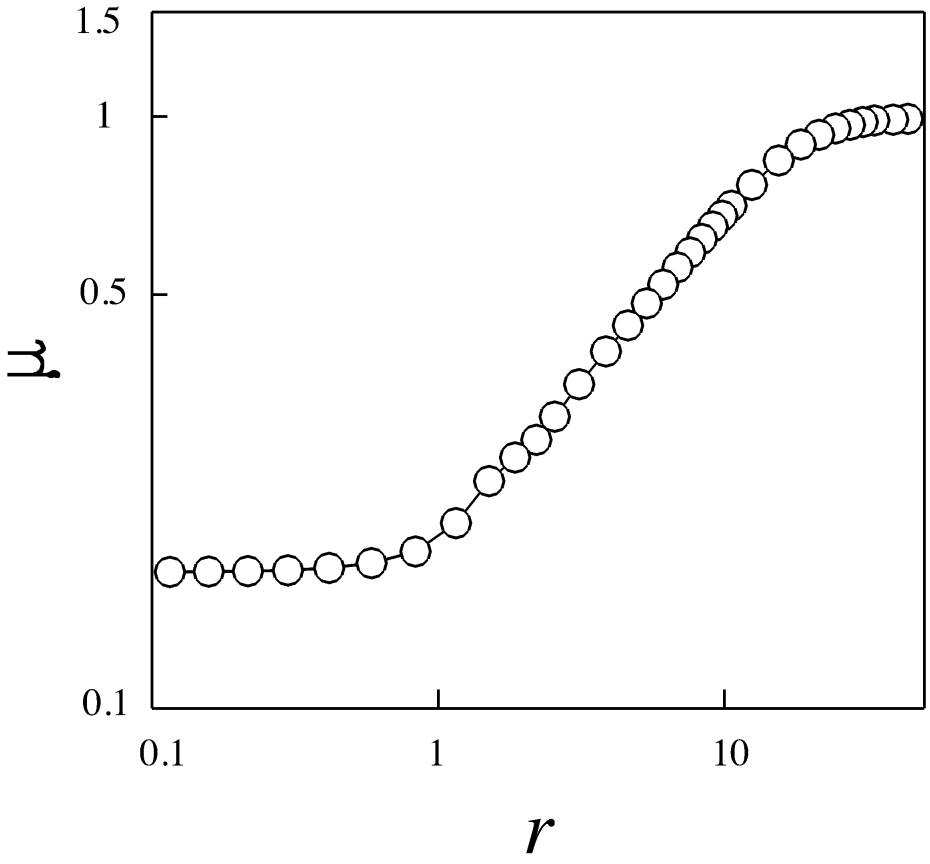


Figure 3.24. **Local apparent viscosity along the impact plane.** Large stresses developed in the impact region ($r < 1$) reduce the local viscosity to about 1/6 of its value at rest during the collision of two shear-thinning laminar jets ($n = 0.7$). The local viscosity then increases as the radial distance from the impact point increases. Here, the jet Reynolds number is $Re = 1$, and the Weber number is $We = 400$.

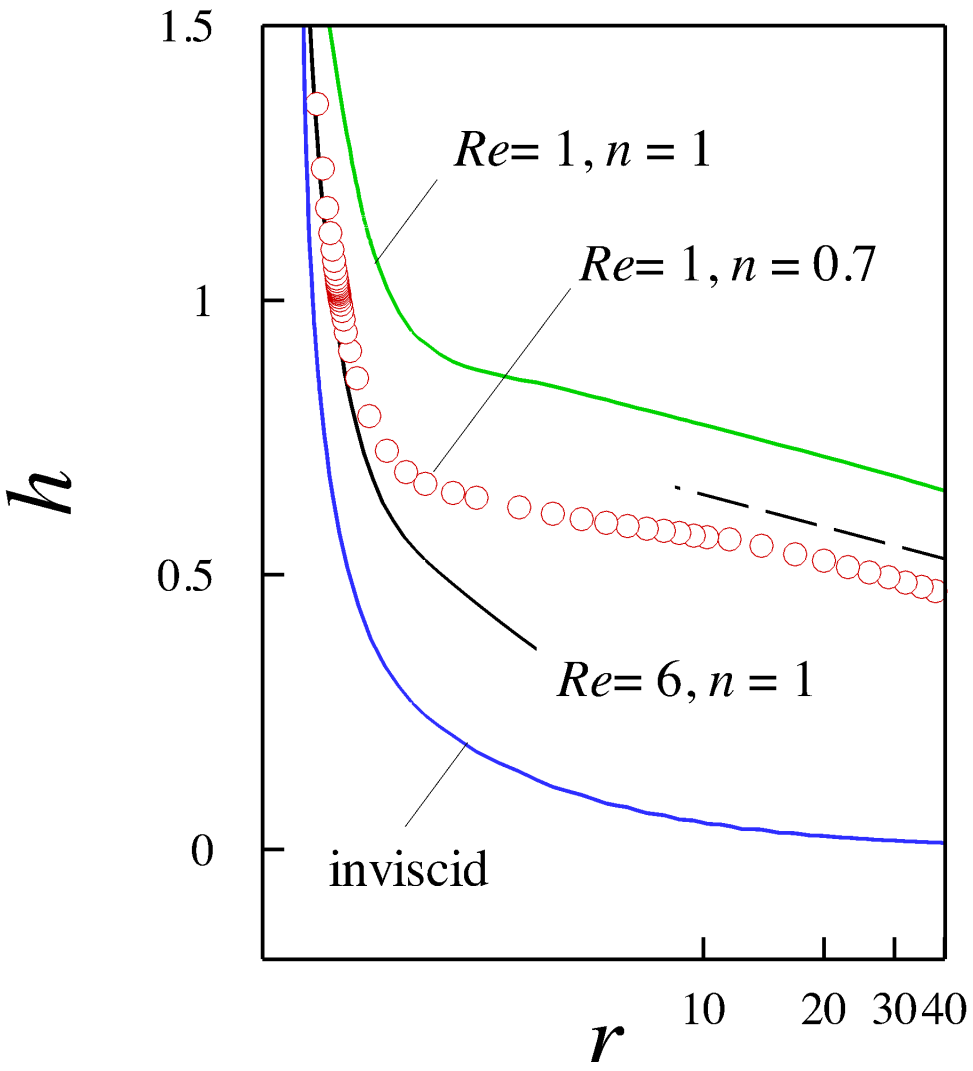


Figure 3.25. **Effect of shear-thinning rheology on liquid sheet shape.** Evolution of the liquid sheet thickness $h$ as a function of the radial distance $r$ for the system illustrated in Figure 3.24 (red circles). For reference the figure also shows the sheet thickness corresponding to the collision of Newtonian liquid jets in the inviscid regime (blue solid line) and with the jet Reynolds numbers $Re = 1$ (green line) and $Re = 6$ (black).

Here the influence of shear-thinning on the steady-state impact viscosity $\bar{\mu} \equiv \mu(r = 0, z = 0)$ and resulting sheet thickness $h(r)$ is illustrated for liquids of different Carreau flow index $n$. According to the Carreau-Yasuda model (cf. Eq. 3.17), a decrease in the Carreau flow index $n$ results in increasing shear-thinning; that is, in faster decrease in the apparent viscosity with shear stress. Figure 3.26 demonstrate that the Carreau flow index plays a major role in determining the viscosity in the impact point and on the overall sheet thickness. The figure illustrates the cross-sectional viscosity field for liquids of low ($n = 0.8$), intermediate ($n = 0.7$), and high ($n = 0.6$) degree of shear-thinning. Results show that, the viscosity in the impact region drops with the flow index from $\bar{\mu} = 0.2$, or about 20% of the zero-shear viscosity, for the low shear-thinning liquid to $\bar{\mu} = 0.03$, or about 3% of the zero-shear viscosity, for the high shear-thinning liquid jets. Simulations for a larger number of the Carreau flow index demonstrate that at given jet Reynolds number $Re$ and the Weber number $We$, the viscosity in the impact regions follows an exponentially scaling $e^n$ with the Carreau flow index as shown in Figure 3.27.

**Effect of the Jet Reynolds Number $Re$ and the Weber Number $We$**

Figure 3.28 demonstrates the important role that the Weber number plays on the steady state viscosity field and sheet thickness. The figure illustrates the sheet profile and cross-sectional viscosity field for three shear-thinning jets ($n = 0.7$) with $We$ numbers in the smooth region $We < 1000$. Results show smaller overall viscosities, and, therefore, faster decrease of the sheet thickness, with increasing $We$ numbers.

Figure 3.29 shows the evolution of the impact viscosity $\bar{\mu}$ with the $We$ number for the shear-thinning jets of Figure 3.28. For this system, the predicted apparent viscosity in the impact region drops to approximately 10% of the zero-shear value when $We = 200$ to approximately 6% of the zero-shear value when $We = 800$. More importantly, a large number of simulations demonstrate that in the smooth region

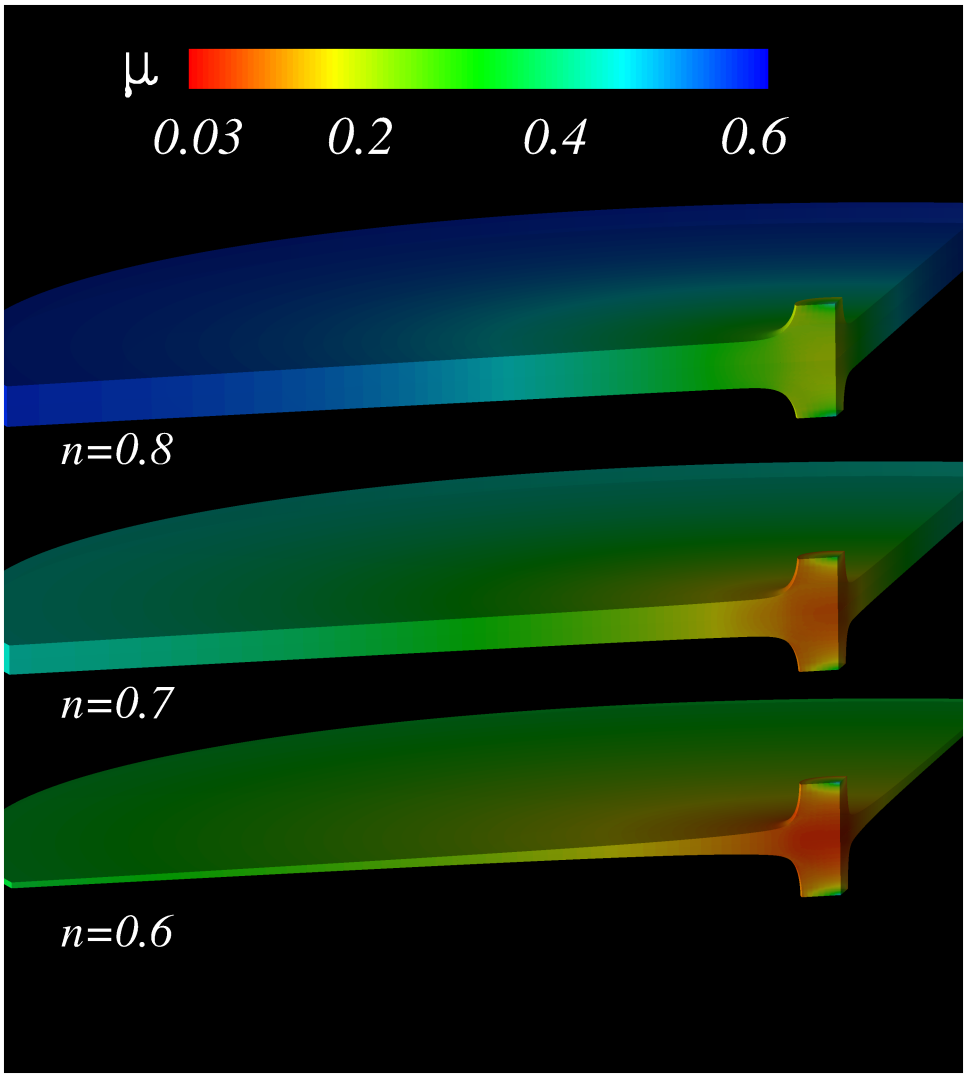


Figure 3.26. **Effect of the Carreau flow index $n$ on sheet thickness.** As the Carreau flow index decreases, larger shear-thinning effects reduce the thickness of the fluid sheet. Here, the jet Reynolds number is $Re = 1$, and the Weber number is $We = 400$.

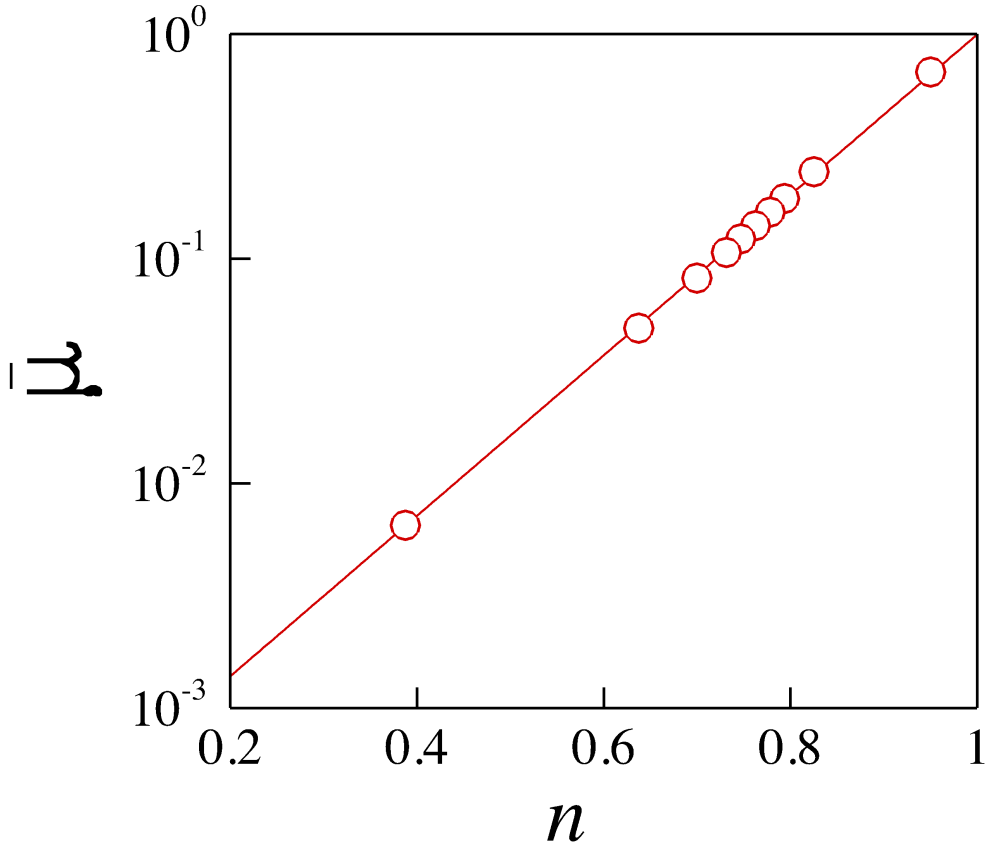


Figure 3.27. **Evolution of the impact viscosity as a function of the Carreau flow index $n$.** The dimensionless impact viscosity $\bar{\mu}$ scales with the Carreau flow index $n$ as $\bar{\mu} \sim e^n$. Here, the jet Reynolds number is $Re = 1$, and the Weber number is $We = 400$.

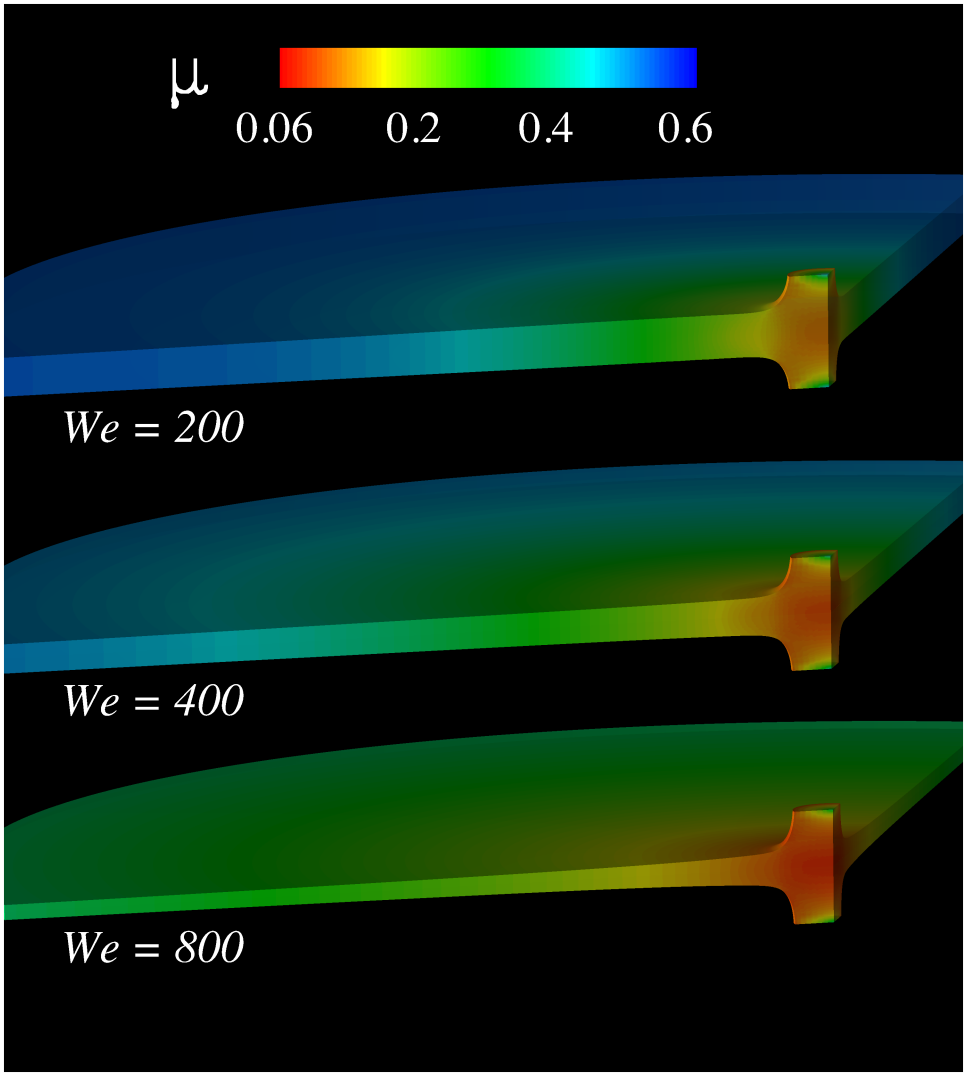


Figure 3.28. **Effect of the Weber number $We$ on sheet thickness.** As the Weber number increases, the thickness of the shear-thinning liquid sheet decreases. Here, the jet Reynolds number is $Re = 1$, and the Carreau flow index is $n = 0.7$.

$We < 1000$, the impact viscosity exhibits a power-law decline $We^{n-1}$ with the Weber number, as shown in Figure 3.30.

Indeed, the results show that for viscous, shear-thinning liquid jets in the smooth region $We < 1000$ the impact viscosity can be predicted precisely by following a universal curve that scales as $\bar{\mu}^{1/(n-1)} \sim Ca$, where the capillary number $Ca \equiv We/Re \equiv \hat{U}\mu_0/\sigma$, where $\hat{U}$ is the dimensional jet velocity, $\mu_0$ is the zero-shear viscosity and $\sigma$ is the surface tension, as illustrated in the summary Figure 3.31.

### 3.2.5 Conclusion

This Section reported simulations that enabled a detailed analysis of the influence of shear-thinning rheology on the axisymmetric impingement of laminar liquid jets. The simulations extend previous works by simultaneously solving the full generalized Navier-Stokes system of equations on both the impingement region and the resulting radially expanding liquid sheet. Moreover, the shear-thinning rheology of the impinging jets is modeled by using a realistic three parameter Carreau-Yasuda rheological model.

Results show that strong shear-stresses developed in the impact region largely reduces the local apparent viscosity. In turn, this shear-thinning effect results in radially expanding sheets that are considerably thinner than the corresponding viscous Newtonian sheets. As the shear-thinning sheets expand, the apparent viscosity increases and the thickness $h$ of the liquid sheets decreases following the characteristic viscous scaling $h = \ln r$ with the distance $r$ from the impact point. Simulations further reveal that the local viscosity in the impact region follows a power law scaling $Ca^{(n-1)}$ with the jet capillary number $Ca = \hat{U}\mu_0/\sigma$, where $\hat{U}$ is the dimensional jet velocity, $\mu_0$ is the zero shear viscosity, and $\sigma$ is the surface tension.

It is expected that these new insights into the mechanisms of shear-thinning impinging jets will enhance the current understanding of spray and atomization systems involving non-Newtonian fluids. However, the results are limited by model assump-

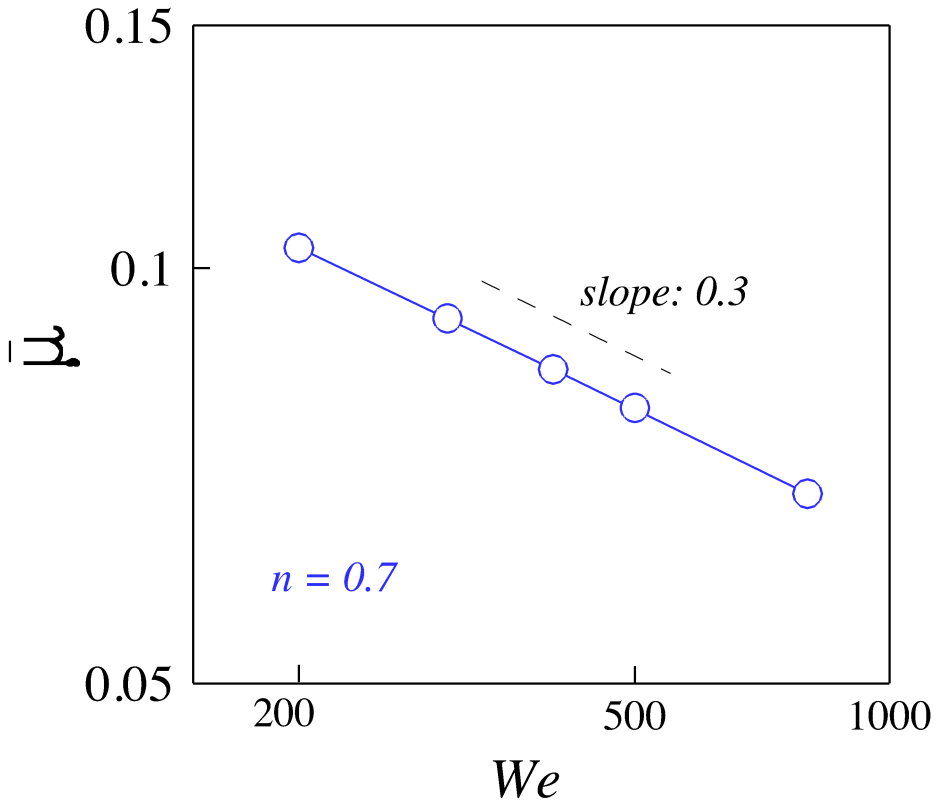


Figure 3.29. **Evolution of the impact viscosity as a function of the Weber number** $We$**.** The dimensionless apparent viscosity at the impact point follows a power-law decline that scales as $We^{n-1}$ with the Weber number. Here, the jet Reynolds number is $Re = 400$, and the Carreau flow index is $n = 0.7$.

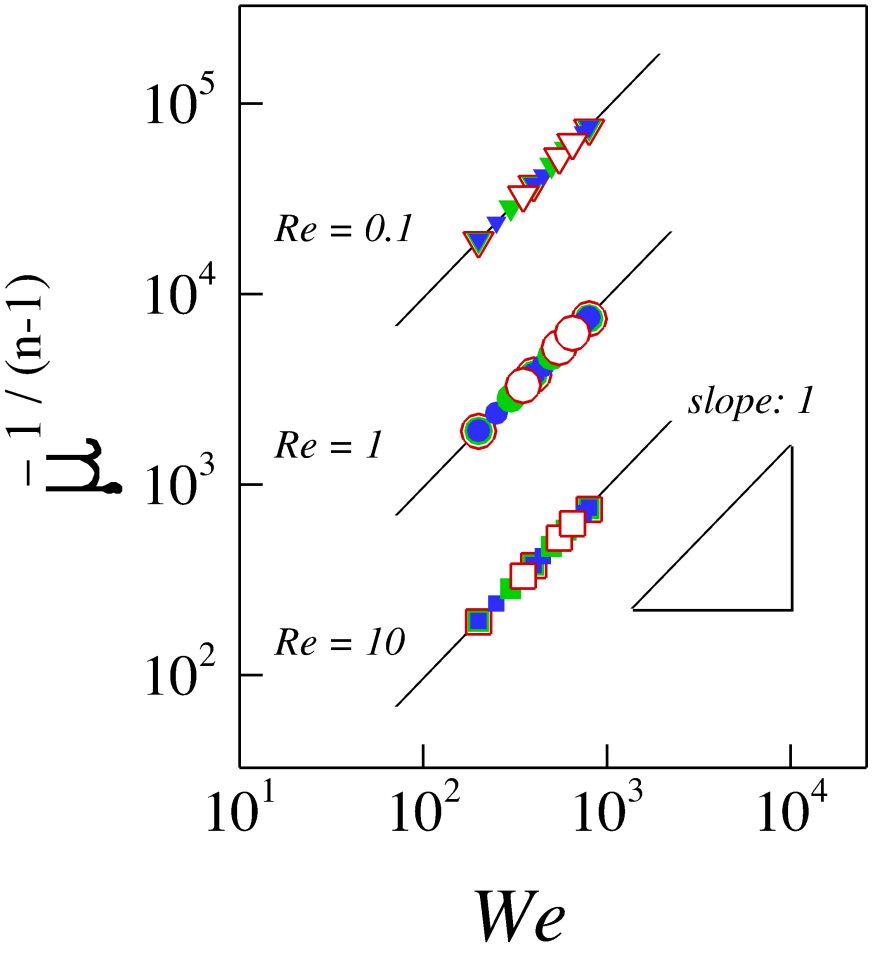


Figure 3.30. **Evolution of the impact viscosity as a function of the Weber number $We$ and the jet Reynolds number $Re$.** The dimensionless apparent viscosity at the impact point $\bar{\mu}$ follows a power-law decline $We^{n-1}$ with the Weber number (solid line). Here, the jet Reynolds numbers are $Re = 0.1$ (triangles), $Re = 1$ (circles), and $Re = 10$ (squares), and the Carreau flow index are $n = 0.3$ (green), $n = 0.5$ (red), and $n = 0.7$ (blue).

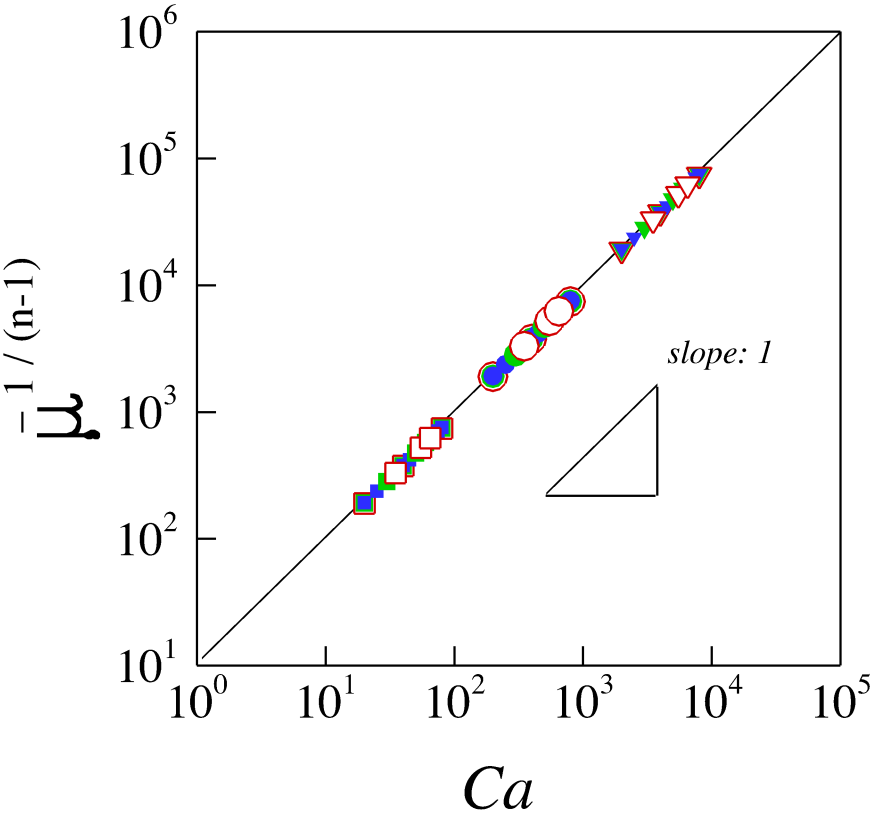


Figure 3.31. **Evolution of the impact viscosity as a function of the Capillary number** $Ca$**.** The dimensionless impact viscosity scales as $Ca^{n-1}$ (solid line). Here, the jet Reynolds numbers are $Re = 0.1$ (triangles), $Re = 1$ (circles), and $Re = 10$ (squares), and the Carreau flow index are $n = 0.3$ (green), $n = 0.5$ (red), and $n = 0.7$ (blue).

tions that restrict the analysis to smooth, axisymmetric systems. Therefore, future work should generalize this study to include the destabilizing action of the surrounding air at higher Weber numbers, and allow oblique impingement of the jets in order to enable a more complete understanding of the influence of shear-thinning effects in the mechanisms of jet impingement. Furthermore, more sophisticated rheological models should be considered, as recent research increasingly shows that extensional stresses may play a significant role in the dynamics of expanding non-Newtonian liquid sheets.

# 4. SUMMARY AND OUTLOOK

This Thesis developed high-fidelity simulations of free-surface flows of complex fluids. The simulations enabled a detailed analysis of the dynamics of drop coalescence and liquid jet impingement when viscous, surfactant and shear-thinning effects are important.

By solving the unsteady free-surface hydrodynamics coupled to the convective-diffusion equation that governs the surfactant transport, this work have made progress towards the understanding of the mechanisms of coalescence of surfactant laden drops.

The simulations demonstrate that surfactants rapidly accumulate on the liquid meniscus bridge formed between the merging drops. Results reveal, for the first time, how the resulting gradient of surfactant concentration controls the rate at which the drops coalesce by modulating the pull of normal (Laplace) and tangential (Marangoni) stresses on the growing meniscus bridge.

Although the numerical algorithm developed for the simulation of drop coalescence solve the full system of Navier-Stokes and surfactant-transport equations, the inertia of the drops and the solubility of the surfactant were not considered. Future work should generalize this analysis to consider higher drop Reynolds numbers and include soluble surfactants. Additionally, future work should include more sophisticated surfactant equations of state able to describe colligative micellar interactions in the tiny meniscus bridge to ensure a more complete understanding of the mechanisms of coalescence in the presence of surfactant.

A second class of free-surface flows studied in this work is the flow generated by two opposed impinging liquid jets. By simultaneously solving the unsteady free-surface hydrodynamics in both the impinging region and the resulting radially expanding liquid sheet, this work have made advances towards the understanding of the mechanisms of jet impingement of viscous and non-Newtonian liquids.

Results demonstrate the critical influence of both viscous and non-Newtonian shear-thinning stresses on the fluid dynamics of the impinging region. Moreover, the moving-boundary parametrization algorithm with free moving spines developed in this work enabled the accurate determination of the unsteady expansion of the fluid sheet and the precise characterization of the influence of viscosity and shear-thinning in the bounding toroidal rim formed at the edge of the sheets.

The simulations reveal that the fluid sheet formed by the jet impingement of viscous fluids expands at a diminishing velocity, hampered by the viscous stresses. As a consequence, viscous fluid sheets are thicker than the inviscid ones. Simulation further demonstrated for the first time that viscous, inertia and intermediate dynamics of jet impingement can be precisely characterized based on the scaling laws of the impact pressure.

Results of jet impingement of shear-thinning liquids demonstrate, for the first time that the degree of shear thinning of the liquid comprising the impinging jets plays a critical role on the local viscosity at the impact point, which consequently determines the thickness of the resulting fluid sheet.

This is an important result since previous analyses have not resolved a detailed picture of the dynamics on the impact region of jet impingement of non-Newtonian shear-thinning liquids.

Results from a large number of simulations also enabled the development of scaling laws to predict the impact viscosity based on $Ca$ number and the Carreau flow index.

Although this new results enhance the current understanding of the physical mechanisms governing viscous and shear-thinning impinging jets, the simulations have been limited to the smooth regime of sheet expansion ($We < 1000$). Future work should enable the analysis of higher impinging velocities ($We > 1000$) by including the destabilizing effect of the surrounding air.

The moving boundary parameterization algorithm enabled accurate sensitivity analysis of the bounding toroidal rim to different flow conditions. However, the separation of the rim from the expanding liquid sheet has not been considered. As a

first approximation, this separation could be considered in future works by assuming that the neck formed downstream of the rim breaks when its thickness is less than a small specified value.

Exciting possibilities for future work also include more sophisticated rheological models that describe viscoelastic behaviour of the fluid. This extension will help better understand dynamics of jet impingement of gelled fluids as more recent works have pointed out that the effect of extensional viscosity from the gelled fluid may play an important role in the atomization process of jet impingement.

# LIST OF REFERENCES

# LIST OF REFERENCES

D. G. Aarts, H. N. W. Lekkerkerker, H. Guo, G. H. Wegdam, and D. Bonn. Hydrodynamics of droplet coalescence. *Physical Review Letters*, 95:164503, 2005.

W. E. Anderson, K. L. Miller, H. M. Ryan, P. S. Santoro, and J. L. Dressler. Effects of periodic atomization on combustion instability in liquid-fueled propulsion systems. *Journal of Propulsion and Power*, 14(11):818–825, 1998.

R. Aris. *Vectors Tensors and the Basic Equations of Fluid Dynamics*. Dover Publication, New Jersey, 1962.

N. Ashgriz. *Handbook of Atomization and Sprays*, volume 1. Springer US, 2011.

G. Baek, S. Kim, J. Han, and C. Kim. Atomization characteristics of impinging jets of gel material containing nanoparticles. *Journal of Non-Newtonian Fluid Mechanics*, 166(2122):1272 – 1285, 2011.

E. X. Berry and R. L. Reinhardt. An analysis of cloud drop growth by collection: Part 3. accretion and self-collection. *Journal of the Atmospheric Sciences*, 31:2118–2126, 1974.

A. Bhakta and E. Ruckenstein. Decay of standing foams: drainage, coalescence and collapse. *Advances in Colloid and Interface Science*, 70:1–214, 1997.

F. Blanchette and T. P. Bigioni. Partial coalescence of drops at liquid interfaces. *Nature Physics*, 2:254–257, 2006.

F. Blanchette, L. Messio, and J. W. M. Bush. The influence of surface tension gradients on drop coalescence. *Physics of Fluids*, 21:072107, 2009.

E. G. Bowen. The formation of rain by coalescence. *Australian Journal of Scientific Research, Series A: Physical Sciences*, 3:193–214, 1950.

H. Braess and P. Wriggers. Abritrary lagrangian eulerian finite element analysis of free surface flow. *Computer Methods in Applied Mechanics and Engineering*, 190: 95–109, 2000.

N. Bremond and E. Villermaux. Atomization by jet impact. *J. Fluid Mech.*, 549: 273–306, 2006.

M. P. Brenner and D. Gueyffier. On the bursting of viscous films. *Physics of Fluids*, 11(3):737–739, 1999.

J. W. M. Bush and A. E. Hasha. On the collision of laminar jets: fluid chains and fishbones. *Journal of Fluid Mechanics*, 511:285–310, 2004.

D. Campana, J. Di Paolo, and F. A. Saita. A 2-d model of rayleigh instability in capillary tubes – surfactant effects. *International Journal of Multiphase Flow*, 50 (5):431–454, 2004.

X. Chen, D. Ma, and V. Yang. Dynamics and stability of impinging jets. *Annual Conference on Liquid Atomization and Spray Stystem, San Antonian, TX*, 2012a.

X. D. Chen, D. J. Ma, and V. Yang. Dynamics and stability of impingement jets. In *Annual Conference on Liquid Atomization and Spray Systems*, number 24, San Antonio, TX, May 2012b.

A. K. Chesters and I. B. Bazhlekov. Effect of insoluble surfactants on drainage and rupture of a film between drops interacting under a constant force. *Journal of Colloid and Interface Science*, 230:229–243, 2000.

K. Chojnacki. *Atomization and Mixing of Impinging Non-Newtonian Jets.* PhD thesis, The University of Alabama, Huntsville, 1997.

K. T. Chojnacki and D. A. Feikema. Atomization studies of gelled liquids. In *AIAA/ASME/SAE/ASEE Joint Propulsion Conference & Exhibit*, number 30, page 2773, Indianapolis, IN, 1994.

Y. J. Choo and B. S. Kang. Parametric study on impinging-jet liquid sheet thickness distribution using an interferometric method. *Experiments in Fluids*, 31:56–62, 2001.

C. Clanet and E. Villermaux. Life of a smooth liquid sheet. *J. Fluid Mech.*, 462: 307–340, 2002.

C. M. Corvalan and F. A. Saita. Automatic stepsize control in continuation procedures. *Computers & Chemical Engineering*, 15(10):729–739, 1991.

R. V. Craster, O. Mater, and D. T. Papageorgiou. Breakup of surfactant-laden jets above the critical micelle concentration. *Journal of Fluid Mechanics*, 629:498–507, 2009.

B. Dai and L. G. Leal. The mechanism of surfactant effects on drop coalescence. *Physics of Fluids*, 20:040802, 2008.

W. M. Deen. *Analysis Transport Phenomena*. Oxford University Press, 2011.

N. Dombrowski and P. C. Hooper. A study of sprays formed by impinging jets in laminar and turbulent flow. *J. of Fluid Mechanics*, 18:392–400, 1964.

N. Dombrowski and W. R. Johns. The aerodynamic instability and disintegration of viscous liquid sheets. *Chemical Engineering Science*, 18(3):203 – 214, 1963.

V. Dravid, S. Songsermpong, Z. J. Xue, C. Corvalan, and P. E. Sojka. Two-dimensional modeling of the effects of insoluble surfactant on the breakup of a liquid filament. *Chemical Engineering Science*, 61(11):3577–3585, 2006.

L. Duchemin, J. Eggers, and C. Josserand. Inviscid coalescence of drops. *Journal of Fluid Mechanics*, 487:167–178, 2003.

J. Eggers, J. R. Lister, and H. A. Stone. Coalescence of liquid drops. *Journal of Fluid Mechanics*, 401:293–310, 1999.

P. M. Gresho, R. L. Lee, and R. L. Sani. On the time-dependent solution of the incompressible navierstokes equations in two and three dimensions. *Recent Advances in Numerical Methods in Fluids*, 1:27–79, 1980.

D. Halpern and J. B. Grotberg. Surfactant effects on fluid-elastic instabilities of liquid-lined flexible tubes: a model of airway closure. *Journal of Biomechanical Engineering*, 115:271–227, 1993.

S. Hansen, G. W. M. Peters, and H. E. H. Meijer. The effect of surfactant on the stability of a fluid filament embedded in a viscous fluid. *Journal of Fluid Mechanics*, 382:331–349, 1999.

D. Hasson and R. E. Peck. Thickness distribution in a sheet formed by impinging jets. *AIChE Journal*, pages 752–754, 1964.

M. F. Heidman, R. J. Priem, and J. C. Humphrey. A study of the spray formed by two impinging jets. *NACA, TN,3835*, 1957.

T. D. Hodgson and J. C. Lee. The effect of surfactants on the coalescence of a drop at an interface i. *Journal of Colloid Interface Science*, 30:94–108, 1969.

R. W. Hopper. Coalescence of two equal cylinders: Exact results for creeping viscous plane flow driven capillarity. *Communications of the American Ceramic Society*, 67:C262, 1984.

P. D. Howell, B. Scheid, and H. A. Stone. Newtonian pizza: spinning a viscous sheet. *Journal of Fluid Mechanics*, 659(23):1–23, 9 2010. ISSN 1469-7645.

J. C. P. Huang. The break-up of axisymmetric liquid sheets. *J. Fluid Mechanics*, 43 (2):305–319, 1970.

E. A. Ibrahim. Instability of a liquid sheet of parabolic velocity profile. *Physics of Fluids*, 10(4):1034–1036, 1998.

E. A. Ibrahim and A. J. Przekwas. Impinging jets atomization. *Physics of Fluids A: Fluid Dynamics*, pages 2981–2987, 1991.

M. D. James, T. D. Kubal, S. F. Son, W. E. Anderson, and T. L. Pourpoint. Calibration of an impinging jet injector suitable for liquid and gelled hypergolic propellants. In *AIAA/ASME/SAE/ASEE Joint Propulsion Conference & Exhibit*, number 45, page 4882, Denver, Colorado, 2009.

J. V. Kampen and H. K. Ciezki. Spray and combustion characteristics of aluminized gelled fuels with an impinging jet injector. *European conference for aerospace sciences*, 2007.

J. V. Kampen, F. Alberio, and H. K. Ciezki. Spray and combustion characteristics of aluminized gelled fuels with an impinging jet injector. *Aerospace Science and Technology*, 11(1):77 – 83, 2007.

H. S. Kheshgi and L. E. Scriven. Measurement of liquid-film profiles by moire topography. *Chemical Engineering Science*, 38(4):525–534, 1983.

S. F. Kistler and L. E. Scriven. *Coating Flow: Computational Analysis of Polymer Processing*. Applied Science Publishers, New York, 1983.

W. H. Lai, T. H. Huang, T. L. Jiang, and W. Huang. Effects of fluid properties on the characteristics of impinging-jet sprays. *Atomization and Sprays*, 15(4):457–468, 2005.

Y. H. Lai, M. H. Hsu, and J. T. Yang. Enhanced mixing of droplets during coalescence on a surface with a wettability gradient. *Lab on a Chip*, 10:3149–3156, 2010.

H. Lefebvre. *Atomization and Sprays*. CRC Press, USA, 1988.

J. Lienhard and T. Newton. Effect of viscosity upon liquid velocity in axi-symmetric sheets. *Zeitschrift fr angewandte Mathematik und Physik ZAMP*, 17(2):348–353, 1966.

S. P. Lin and W. Y. Jiang. Absolute and convective instability of a radially expanding liquid sheet. *Physics of Fluids*, 15(6):1745, 2003.

Z. Liu, G. Brenn, and F. Durst. Linear analysis of the instability of two-dimensional non-newtonian liquid sheets. *Journal of Non-Newtonian Fluid Mechanics*, 78(6): 133–166, 1998.

L. Lobo and A. Svereika. Coalescence during emulsification 2. role of small molecule surfactants. *Journal of Colloid and Interface Science*, 261:498–507, 2003.

G. Luo, L. Du, Y. Wang, Y. Lu, and J. Xu. Controllable preparation of particles with microfluidics. *Particuology*, 9(6):545 – 558, 2011.

A. J. Mahajan and D. J. Kirwan. Micromixing effects in a two-impinging-jets precipitator. *AIChE Journal*, 42(7):1801–1814, 1996. ISSN 1547-5905.

J. Mallory and P. E. Sojka. On the primary atomization of non-newtonian impinging jets: Volume ii linear stability theory. *Journal of Propulsion and Power*, 24(6): 525–554, 2014.

C. Marangoni. Ueber die ausbreitung der tropfen einer flssigkeit auf der oberflche einer anderen. *Annalen der Physik*, 219(7):337–354, 1871.

J. I. Martinez-Herrera and J. J. Derby. Analysis of capillary-driven viscous flows during the sintering of ceramic powders. *AICHE Journal*, 40:1794–1804, 1994.

J. I. Martinez-Herrera and J. J. Derby. Viscous sintering of spherical particles via finite element analysis. *Journal of American Ceramic Society*, 78(3):645–649, 1995.

D. J. McClements. *Food emulsions: principles, practice, and techniques*. CRC Press, 1999.

E. Miller, B. Gibson, E. McWilliams, and J. P. Rosthstein. Collision of viscoelastic jets and the formation of fluid webs. *Applied Physics Letters*, 87:014101, 2005.

W. J. Milliken, H. A. Stone, and L. G. Leal. The effect of surfactant on the transient of newtonian drops. *Physics of Fluids A*, 5(1):69–79, 1993.

R. J. Muddu, J. Lu, P. E. Sojka, and C. M. Corvalan. Threshold wavelength on filaments of complex fluids. *Chemical Engineering Science*, 69(1):602–606, 2012.

M. Negril and H. K. Ciezki. Liquid sheet dynamics and primary breakup characteristics at impingement type injector. In *AIAA/ASME/SAE/ASEE Joint Propulsion Conference & Exhibit*, number 46, page 6821, Nashville, TN, 2010.

H. N. Oguz and A. Prosperetti. Surface-tension effects in the contact of liquid surfaces. *Journal of Fluid Mechanics*, 203:149–171, 1989.

S. Osher and R. P. Fedkiw. Level set methods: an overview and some recent results. *Journal of Computational Physics*, 169:463–502, 2001.

J. D. Paulsen, J. C. Burton, and S. R. Nagel. Viscous to inertial crossover in liquid drop coalescence. *Physical Review Letters*, 106(11):114501, 2011.

J. D. Paulsen, J. C. Burton, S. R. Nagel, S. Appathurai, M. T. Harris, and O. A. Basaran. The inexorable resistance of inertia determines the initial regime of drop coalescence. *Proceedings of the National Academy of Sciences of the United States of America*, 109(18):1–5, 2012.

W. E. Ranz. Some experiments on the dynamics of liquid films. *Journal of Applied Physics*, 30(12):1950–1955, 1959.

J. N. Reddy. *An introduction to nonlinear finite element analysis*. Oxford University Press, USA, 2004.

H. M. Ryan, W. E. Anderson, S. Pal, and R. J. Santoro. Atomization characteristics of impinging liquid jets. *Journal of Propulsion and Power*, 11(1):135–145, 1993.

H. Saito and L.E. Scriven. Study of coating flow by the finite element method. *Journal of Computational Physics*, 42(1):53 – 76, 1981.

P. H. S. Santos, R. Arnold, W. E. Anderson, M. A. Carignano, and O. H. Campanella. Characterization of jp-8/$sio_2$ and rp-1/$sio_2$ gels. *Engineering Letters*, 18(1):41, 2010.

J. D. Sartor. Electricity and rain. *Physics Today*, 22:45–51, 1969.

F. Savart. Memoire sur le choc dune veine de liquide lance contre un plan circulaire. *Annual Review of Physical Chemistry*, 59(113-145), 1833.

R. Scardovelli and S. Zaleski. Direct numerical simulation of free-surface and interfacial flow. *Annual Review of Fluid Mechanics*, 31:567–603, 1999.

L. E. Scriven and C. V. Sternling. Marangoni effects. *Nature*, 187(4733):186–188, 1960.

J. C. Slattery. *Interfacial Transport Phenomena*. Springer, New York, 1990.

H. B. Squire. Investigation of the instability of a moving liquid film. *British Journal of Applied Physics*, 4(6):167, 1953.

H. A. Stone. A simple derivation of the time-dependent convective-diffusion equation dynamics of drop formation and breakup in viscous fluids. *Anuall Review of Fluid Mechanics*, 26:65–102, 1990.

F. P. Sutton. *Rocket propulsion element: an introduction to the engineering of rockets*. John WIley, New York, 1992.

G. I. Taylor. Formation of thin flat sheets of water. *Proc. Royal Soc. A*, 259:1–17, 1960.

J. Thomson and H. Newall. On the formation of vortex rings by drops falling into liquids, and some allied phenomena. *Proceedings of the Royal Society of London*, 39:417–436, 1885.

S. T. Thoroddsen, K. Takehara, and T. G. Etoh. The coalescence speed of a pedent and a sessile drop. *Journal of Fluid Mechanics*, 527:85–114, 2005.

S. T. Thoroddsen, B. Qian, T. G. Etoh, and K. Takehara. The initial coalescence of miscible drops. *Physics of Fluids*, 19:072110, 2007.

S. T. Thoroddsen, T. G. Etoh, and K. Takehara. High-speed imaging of drops and bubbles. *Annual Review of Fluid Mechanics*, 40:257–285, 2008.

Nirupama A. Vaidya. *Numerical simulation of the capillary driven fusion of complex foods as a model system for caking of amorphous food powders*. PhD thesis, Purdue University, Indiana, May 2010.

E. Villermaux, V. Pistre, and H. Lhuissier. The viscous Savart sheet. *Journal of Fluid Mechanics*, 730:607–625, 2013.

D. Weihs. Stability of thin, radially moving liquid sheets. *Journal of Fluid Mechanics*, pages 289–298, 1978.

H. Wong, D. Rumschitzki, and C. Maldarelli. On the surfactant mass balance at a deforming fluid interface. *Physics of Fluids*, 8:3203, 1996.

B. Xu, N. T. Nguyen, and T. N. Wong. Temperature-induced droplet coalescence in microchannels. *Biomicrofluidics*, 6(1):012811–012811, 2012.

B. Xu, N. T. Nguyen, and T. N. Wong. Droplet coalescence in microfluidic systems. *Micro and Nanosystem*, 3(2):131–136, 2014.

Z. Xue, C. M. Corvalan, V. Dravid, and P. E. Sojka. Breakup of shear-thinning liquid jets with surfactants. *Chemical Engineering Science*, 63(7):1842–1849, 2008.

B. Yaghoub, S. Shahrokh, and A. M. Mahdi. Modeling gas oil spray coalescence and vaporization in gas solid riser reactor. *International Communications in Heat and Mass Transfer*, 37:935–943, 2010.

L. Yang, F. Zhao, Q. Fu, and K. Cui. Rheological characterization of monomethylhydrazine gels. *Journal of Propulsion and Power*, 29(2):313–320, 2013.

L. J. Yang, Q. F. Fu, Y. Y. Qu, B. Gu, and M. Z. Zhang. Breakup of a power-law liquid sheet formed by an impinging jet injector. *International Journal of Multiphase Flow*, 39:37–44, 2012.

L. J. Yang, F. Zhao, Q. Fu, and K. Cui. Liquid Sheet Formed by Impingement of Two Viscous Jets. *Journal of Propulsion and Power*, pages 1–11, 2014.

W. Yao, J. Maris, P. Pennington, and G. M. Seidel. Coalescence of viscous liquid drops. *Physical Review E*, 71:016309, 2005.

D. Y. K. Yap and D. P. Gaver. The influence of surfactant on two-phase flow in a flexible-walled channel under bulk equilibrium conditions. *Physics of Fluids*, 10(8): 1846–1863, 1998.

VITA

# VITA

Jiakai Lu was born to Guoming Lu and Qiuhua Lu in Shanghai, China on March 9, 1986. After graduated from Shanghai Yan'an Senior High School in 2004, he was admitted to Shanghai Jiao Tong University to pursue his Bachelor degree in the department of Mechanical Engineering. Jiakai earned his Bachelor of Engineering degree in June 2008 and joined Purdue University in Auguest 2008 to pursue his Master degree and later transfered to the direct Ph.D. degree in 2010 under the guidance of Professor Carlos M. Corvalan and Professor Paul E. Sojka.

For his Ph.D research, Jiakai studied fundamental physics of free surface flows of complex fluids such as coalescence of surfactant-laden drops and non-Newtonian impinging jets and resulted three journal publications to his name and has others in preparation. He has presented his research at several international technical conferences. Upon graduation, Jiakai may continue pursuing a career in the academia as a researcher.